

Engineered type-II heterostructures

for high efficiency solar cells

by

Jinyoung Hwang

**A dissertation submitted in partial fulfillment
of the requirements for the degree of**

**Doctor of Philosophy
(Electrical Engineering)**

in the University of Michigan

2013

Doctoral Committee:

Associate Professor Jamie D. Phillips, Chair

Professor Joanna M. Millunchick

Professor Jasprit Singh

Professor Duncan Steel

© Jinyoung Hwang

2013

To my parents

ACKNOWLEDGMENTS

First, I would like to express the deepest appreciation to my committee chair and research advisor, Professor Jamie Phillips, for his expertise, support, and generous guidance.

I also would like to thank my committee members, Professor Joanna Millunchick, Professor Jasprit Singh, and Professor Duncan Steel for valuable discussions and advice throughout this work.

I would like to acknowledge the past and current members of Phillips' research group, collaborators, and all my friends.

I would like thank to staff members of the Lurie Nanofabrication Facility (LNF) and Solid State Electronics Lab (SSEL), and Electrical Engineering at the University of Michigan for their support through my graduate carrier. I gratefully acknowledge scholarship support from the STX Foundation in South Korea.

Finally, I would like to express my heartfelt gratitude to my family for their love, support, and encouragement throughout my entire life.

This work is supported as part of the Center for Solar and Thermal Energy Conversion, an Energy Frontier Research Center funded by the U.S. Department of Energy, Office of Science, Office of Basic Energy Sciences under Award Number DE-SC0000957

TABLE OF CONTENTS

DEDICATION	ii
ACKNOWLEDGMENTS	iii
LIST OF FIGURES	vii
LIST OF TABLES	xi
LIST OF APPENDICES	xii
ABSTRACT.....	xiii
CHAPTER	
1. Introduction.....	1
1.1. Limit of single junction solar cells.....	3
1.2. Exceeding the Shockley-Queisser limit.....	5
1.3. Multi-junction solar cells.....	7
1.4. Intermediate band solar cells	12
1.5. Thesis outline.....	16
2. Band structure of strain-balanced GaAsBi/GaAsN superlattices on GaAs	
.....	17
2.1. Introduction.....	17
2.2. Methods.....	18
2.2.1. Overview.....	18
2.2.2. Material parameters	19

2.2.3. Strain balanced criteria	20
2.2.4. Band-structure calculation by the k.p method	22
2.2.5. Mini-band structure with Self-consistent solution of Schrödinger-Poisson equations	25
2.2.6. Absorption coefficient	27
2.3. Results and Discussion	28
2.3.1. Bandstructure	28
2.3.2. Effective mass	31
2.3.3. Spatial Distribution of Wavefunctions.....	31
2.3.4. Optical Properties.....	34
2.4. Conclusions.....	36
3. Electronic structures of GaSb/GaAs quantum dots	38
3.1. Introduction.....	38
3.2. Methods.....	39
3.2.1. Quantum dot structures	39
3.2.2. Strain distribution.....	41
3.2.3. Electronic structures.....	42
3.2.4. Optical transition.....	45
3.3. Results.....	46
3.3.1. Electronic structure	46
3.4. Conclusions.....	54

4. Thermal emission in type-II GaSb/GaAs quantum dots and prospects for intermediate band solar energy conversion	56
4.1. Introduction.....	56
4.2. Methods.....	58
4.3. Results.....	58
4.4. Discussions	66
4.5. Conclusions.....	68
5. GaSb/GaAs quantum dot intermediate band solar cells.....	69
5.1. Introduction.....	69
5.2. GaSb/GaAs quantum dot growth.....	71
5.3. Experimental Procedure.....	73
5.4. Results and discussions.....	76
5.5. Conclusions.....	89
6. Conclusion	91
6.1. Summary of present work.....	91
6.1.1. Strain-balanced GaAsBi/GaAsN superlattice on GaAs.....	91
6.1.2. Type-II GaSb/GaAs self-assemble quantum dots.....	92
6.2. Future works	94
6.2.1. Strain compensation layers	94
6.2.2. Quantum-dot-in-a-fence (DEFENCE) heterostructure	96
APPENDICES.....	100
BIBLIOGRAPHY.....	108

LIST OF FIGURES

Figure

- Figure 1.1 Efficiency and cost projections for first- (I), second (II), and third-generation (III) solar cells representing Silicon wafer-based single junction photovoltaic technology, thin film PV technology, and advanced thin film PV technology, respectively (adopted from [3]) 2
- Figure 1.2 Fundamental loss processes in a standard single junction solar cell: (1) transparent loss, (2) thermalization loss, (3) junction voltage loss, (4) contact voltage loss, and (5) recombination loss (adopted from [1]) 4
- Figure 1.3 (a) Portions of intrinsic losses of a single junction solar cell with bandgap E_g in solar spectrum (one sun illumination) and (b) fraction of loss mechanisms as a function of bandgap (adopted from [5]) 4
- Figure 1.4 (a) Multi-junction solar cell, (b) intermediate band solar cell, (c) hot carrier solar cells, (d) multiple exciton generation, and (e) up/down converters 6
- Figure 1.5 Relation between bandgap and lattice constant of ternary and quaternary III-V compound semiconductors (adopted from [12]) 9
- Figure 1.6 (a) Bandgaps and lattice parameters of composite semiconductors and (b) voltage and current for each sub-cells in the triple junction solar cells (adopted from [14]) 11
- Figure 1.7 The calculated energy of band structure (left) and density of states (right) for $Zn_{0.88}Mn_{0.12}O_{0.01}Te_{0.99}$ based on the band anticrossing model (adopted from [19]) 14
- Figure 1.8 Schematic diagram of an IBSC constructed by InAs/GaAs QDs 15
- Figure 2.1 Bandgap energy versus lattice constant for GaAsN [28] and GaAsBi [29, 30] dilute alloys and (inset) schematic of strain-balanced GaAsBi/GaAsBi superlattice with effective lattice match to GaAs. 18
- Figure 2.2 Strain balanced composition of Bi and N for several thickness ratios of GaAsBi and GaAsN layers. 22

Figure 2.3 Miniband structure of 40Å/40Å GaAs _{0.96} Bi _{0.04} /GaAs _{0.979} N _{0.021} superlattice with effective bandgap energy of 1eV.....	30
Figure 2.4 Effective bandgap energy for GaAsBi/GaAsN superlattices with matched layer thickness, varying period thickness and variable alloy composition.....	30
Figure 2.5 Effective masses of ground state minibands (m_e^* for CB1 and m_{hh}^* for HH1) for GaAsBi/GaAsN superlattices with matched layer thickness, varying period thickness and variable alloy composition.....	33
Figure 2.6 Miniband structure for 10 period 40Å/40Å GaAs _{0.96} Bi _{0.04} /GaAs _{0.979} N _{0.02} superlattice using self-consistent Schrödinger-Poisson calculations.....	33
Figure 2.7 Squared envelope function of the 40Å/40Å GaAs _{0.96} Bi _{0.04} /GaAs _{0.979} N _{0.02} superlattice. Characters s and x in the figure represent the symmetry character of the envelop function.....	34
Figure 2.8 Joint density of states of a 40Å/40Å GaAs _{0.96} Bi _{0.04} /GaAs _{0.979} N _{0.02} superlattice.....	35
Figure 2.9 Absorption coefficient of of a 40Å/40Å GaAs _{0.96} Bi _{0.04} /GaAs _{0.979} N _{0.02} superlattice.....	35
Figure 3.1 Contour plots of varying Sb concentrations composed from atom probe tomography data within the GaSb/GaAs QD layers of the sample, as seen from the (001) surface (adopted from [67]).....	40
Figure 3.2 Model structure of a GaSb QD with 1ML GaSb wetting layer on (100) surface embedded in GaAs matrix, together with the axes referred to in the text	40
Figure 3.3 The strain distribution of the GaSb QD embedded in the GaAs matrix, calculated using the VFF strain model: (a) ϵ_{xx} at the xy-plane (0.5nm above the base of the QD), (b) ϵ_{xx} at the xz-plane (crossing the center of the dot), (c) ϵ_{zz} at the xy-plane (0.5nm above the base of the QD), (d) ϵ_{zz} at the xz-plane (crossing the center of the dot), and ϵ_{xx} and ϵ_{zz} along (e) [100] direction (0.5nm above the base of the dot) and (f) [001] direction through the center of the dot.....	47
Figure 3.4 The strain distribution of the GaSb QD embedded in the GaAs matrix, calculated using the VFF strain model: Hydrostatic strain (a) at the xy-plane (0.5nm above the base of the QD) and (b) at the xz-plane (crossing the center of the dot), biaxial strain (c) at the xy-plane (0.5nm above the base of the QD) and at the xz-plane (crossing the center of the dot), and the hydrostatic and biaxial strain plotted along (e) [100] direction (0.5nm above the base of the dot) and (f) [001] direction through the center of the dot.....	48
Figure 3.5 The strain distribution of the GaSb QD embedded in the GaAs matrix, calculated using the VFF strain model (shear strain): ϵ_{xy} (a) at the xy-plane	

(0.5nm above the base of the QD) and (b) at the xz-plane (crossing the center of the dot), ϵ_{yz} (c) at the xy-plane (0.5nm from the base of the QD) and at the xz-plane (crossing the center of the dot), ϵ_{zx} (c) at the xy-plane (0.5nm from the base of the QD) and at the xz-plane (crossing the center of the dot), and the shear strain tensors plotted along (e) [100] direction (0.5nm above the base of the dot) and (f) [001] direction through the center of the dot.....	50
Figure 3.6 The electron, heavy-hole, and light-hole potential profile along [100] direction through the center of QD (0.5nm above the base of QD) imposed by the hole states calculated by the 8-band k.p model. (The hole states in the grey area near LH band are too close to show their spacing clearly.).....	52
Figure 3.7 Photoluminescence spectra of the GaSb/GaAs QDs (from Tim Saucer and Vanessa Sih, Physics, University of Michigan).....	52
Figure 3.8 Contour plots of squared wavefunctions, $ \Psi ^2$, of the first eight energy levels in the GaSb/GaAs QD at the xy-plane 0.5nm above the base of the QD. The energy level of each wavefunction is indicated in the corresponding plot.	53
Figure 3.9 Hole states and the energy spectra in the GaSb QD when the dot is fully occupied by holes.....	54
Figure 4.1 (a) Capacitance-Voltage characteristics measured at 300K under AC bias at $f = 1$ MHz (data is offset vertically by $0.03 \mu\text{F}/\text{cm}^2$ for clarity), and (b) majority carrier distribution of the Schottky diode samples.	60
Figure 4.2 (a) Temperature-dependent conductance of QD, QW, and GaAs control samples measured at $V = 1.4$ V and $f = 1$ MHz, (b) temperature-dependent conductance of the QD sample at $f = 1$ MHz and varying bias, (c) temperature-dependent conductance of the QD sample at $V = 1.4$ V and varying frequency, and (d) band diagram under reverse bias at 0.8V (left) and at 2.0V (right)....	62
Figure 4.3 (a) Arrhenius plots constructed from peak conductance to extract activation energy and thermal capture cross section, and (b) activation energy and (c) thermal capture cross section extracted from Arrhenius plots and obtained by subtracting Coulomb charging energy.	65
Figure 4.4 Optical (red) and thermal (blue) emission rates of holes in GaSb/GaAs QDs under different solar concentration	67
Figure 5.1 AFM images of the uncapped 11th layer of QDs grown on the (2×8) surface with a height scale of 8 nm (adopted from ref [99]).....	72
Figure 5.2 Photoluminescence spectra measured at 10K for a sample with ten layers of GaSb QD grown on the (2×8) surface (adopted from ref [99])	72
Figure 5.3 (a) A complete structure of GaAs p ⁺ n solar cell with five layers of GaSb QD and (b) scanning transmission electron microscope image of the QD layers in	

the solar cell (from Sung Joo Kim and Xiao Pan, Material Science Engineering, University of Michigan)	74
Figure 5.4 (a) Details of the GaAs p ⁺ n solar cell structure and (b) the band diagram of the device at the equilibrium and under the reverse biases of 1V, 2V, 3V, and 4V.	79
Figure 5.5 Current density vs voltage (<i>J-V</i>) characteristics measured (a) under the 1 sun, AM 1.5G simulated solar irradiation and (b) the dark condition.....	80
Figure 5.6 (a) EQE spectra at the equilibrium and under the reverse biases of 1V, 2V, 3V, and 4V of the GaAs p ⁺ n solar cell with the five layers of GaSb QDs and the control cell without the QD layers. (b) Contributions of the emitter, space charge region, and the base to EQEs of the control and (c) the QD-IBSC.....	82
Figure 5.7 Schematic illustration of the carrier transport in the GaAs p ⁺ n junction with the GaSb QD layers under the irradiation of (a) short-wavelength photons, (b) long-wavelength photons, and (c) photons with energy less than the GaAs bandgap.....	84
Figure 5.8 (a) Device structure and (b) the band diagram of the GaAs p ⁺ n solar cell with the five layers of GaSb QDs placed in the graded junction.....	86
Figure 5.9 Current density vs voltage (<i>J-V</i>) characteristics measured under (a) the 1 sun, AM 1.5G simulated solar irradiation and (b) the dark environment, and (c) EQE spectra of the GaAs p ⁺ n solar cell with the five layers of GaSb QDs placed in the graded junction (results from Figure 5.5 and Figure 5.6 are also plotted for comparison).....	88
Figure 6.1 Scanning transmission electron microscope images of the QD layers in the solar cell that have dislocations due to the strain accumulation from the QD layers (from Sung Joo Kim and Xiao Pan, Material Science Engineering, University of Michigan).....	95
Figure 6.2 (a) Conduction band offsets and (b) valance band offsets of the III-V semiconductors as a function of lattice constant (adopted from ref [75])	98
Figure 6.3 (a) Structure of the quantum-dot-in-a-fence barrier with Ga _{0.51} In _{0.49} P and (b) the expected band diagram of the heterostructure	99

LIST OF TABLES

Table

Table 1.1 Optimal bandgap of consisting junctions and maximum efficiency limit of multi-junction solar cells under AM1.5 Global radiation [10]	8
Table 3.1 Parameters used in the VFF calculations [69]	42
Table 3.2 Parameters used in the 8-band k.p calculation [74-76]	43
Table 3.3 Deformation potential parameters used in the 8-band k.p calculation [76]	43
Table 5.1 Solar cell characteristics measured under the AM 1.5G spectrum	89

LIST OF APPENDICES

Appendix

- A. Eight-band k.p model within the envelope function approximation..... 101
- B. GaAs solar cell fabrication procedures 105

ABSTRACT

The third-generation solar cell technologies are aiming to achieve substantially higher efficiency over the Shockley-Queisser limit of a single junction solar cell while maintaining low fabrication cost per area in order to become cost competitive with coal fuel. The demanding of a breakthrough in efficiency leads the research to the development of photovoltaic devices with a new concept of fundamental operation other than the structure of single junction solar cells and to the employment of various materials and nanostructures to the devices.

The purpose of the projects in this dissertation to present nanostructures with type-II heterointerface that can provide additional possibilities to certain types of third generation solar cells for achieving an efficiency close to the theoretical maximum limit.

First, the electronic structure and optical properties of type-II GaAsBi/GaAsN superlattices with an effective lattice constant match to GaAs are studied based on the 8-band k.p method and Self-consistent Schrödinger-Poisson equation. Results show that this heterostructure can provide a new material system with a range of effective bandgap of 0.89eV - 1.32eV, which is a spectral range of high importance for the multi-junction solar cells, for Bi,N composition of less than 5% and period thickness of up to 100Å.

Second, the electronic structure, optical properties, and thermal carrier capture and escape mechanisms of the type-II GaSb/GaAs self-assembled quantum dots (QDs)

are studied theoretically and experimentally to examine the advantages of the heterostructure for the intermediate band solar cells (IBSCs). The electronic structures of the GaSb QDs calculated based on the VFF and the 8-band $\mathbf{k}\cdot\mathbf{p}$ model show that there is substantially closer spacing between the states because of the large hole effective mass, and 16 holes can fill a QD completely. Admittance spectroscopy measurements show that the thermal emission rate is significantly lower than prior reports for InAs/GaAs type-I QDs, and is estimated to be lower than the optical generation rates in an IBSC under solar concentration. Also, the fabricated GaSb/GaAs QD-IBSCs demonstrate the sub-bandgap response occurred through sub-bandgap photon absorption via the QD confined states and the enhanced the short circuit current compared to a control sample without the QDs.

CHAPTER 1

Introduction

Most currently developed solar cell technologies are aiming to achieve substantially higher efficiency over the Shockley-Queisser limit of a single junction solar cell while maintaining low fabrication cost per area in order to reduce the cost per peak Watt (W_p) to $\$0.20/W_p$ in order to become cost competitive with coal fuel [1, 2]. The solar cells in these research areas are classified as “Third-generation solar cells” indicated as III in Figure 1.1 [3]. In order to make a breakthrough in efficiency, the research is directed toward developing photovoltaic devices with a new concept of fundamental operation other than the structure of single junction solar cells, and various materials and nanostructures are employed for the devices in this new area. The third generation photovoltaic technologies prefer a thin film structure to reduce material usage, but the thin film strategy does not require large-scale areas for a given level of power because of their outstanding efficiency. Therefore, although the fabrication cost per area of these third-generation photovoltaic devices is rather higher than that of the devices in the second generation, displayed as II in Figure 1.1, due to their complicated structure, the total fabrication cost per certain power output can decrease dramatically in these third-generation technologies.

The purpose of the projects in this dissertation to present material systems with type-II heterostructures that can provide additional possibilities for certain types of third-generation solar cells for achieving an efficiency close to the theoretical maximum limit. The advantages in electronic and optical characteristics of the type-II heterostructures are examined, and the utilization of the structures in the solar cell devices is presented.

In the following sections, the fundamental factors that limit the efficiency of a single junction cell are addressed, and the operational principles of the third junction solar cell are explained, based on the limiting factors that the devices intend to reduce.

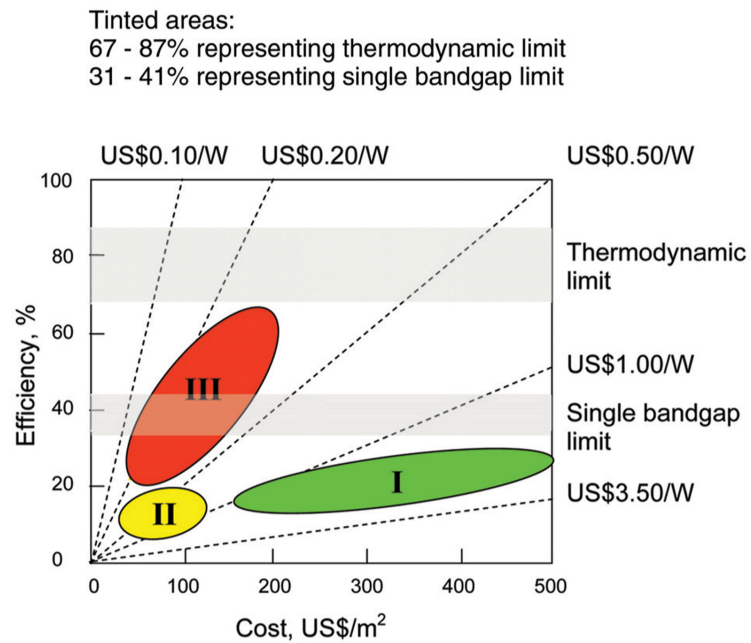


Figure 1.1 Efficiency and cost projections for first- (I), second (II), and third-generation (III) solar cells representing Silicon wafer-based single junction photovoltaic technology, thin film PV technology, and advanced thin film PV technology, respectively (adopted from [3])

1.1. Limit of single junction solar cells

Based on the principle of detailed balance, the maximum theoretical efficiency of a single pn junction solar cell is 32.9 % with a bandgap of 1.34 eV and under air mass 1.5 (AM 1.5). [4] The upper limit results from the major fundamental losses in the energy conversion process in the single junction solar cell of thermalization loss, transparent loss, junction and contact voltage loss, and radiative recombination loss, illustrated in Figure 1.2. [1] Among the loss processes, the most dominant loss mechanisms are thermalization loss and transparent loss shown in Figure 1.3 (a), and they originate from the mismatch between the broad solar spectrum and the bandgap of semiconductor materials.

Thermalization loss occurs when the absorbed photon energy is greater than the band gap of the semiconductor material. Electrons and holes in the excited states quickly relax to the edge of the conduction and valence band, respectively, and the photon energy in excess of the bandgap transforms heat through electron-phonon scattering. The energy loss results in a reduction in the open circuit voltage. On the other hand, transparent loss occurs when incident photon energy is lower than the bandgap because the photon cannot be absorbed into the semiconductor, inducing a current reduction. Basically, in the single junction solar cell these two key fundamental losses cannot decrease simultaneously because reduction in one loss induces an increment in another loss. Shown in Figure 1.3 (b), a larger bandgap semiconductor can reduce the thermalization loss while sacrificing more photon absorption, and smaller bandgap semiconductor can extend absorption spectra to longer wavelengths while losing more photon energy as heat. As a result, the trade-off between these two intrinsic losses determines the limiting efficiency at the optimal bandgap near 1.34 eV.

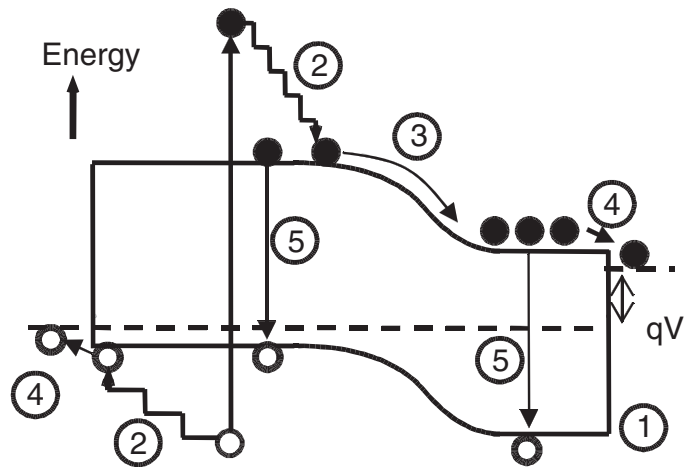


Figure 1.2 Fundamental loss processes in a standard single junction solar cell: (1) transparent loss, (2) thermalization loss, (3) junction voltage loss, (4) contact voltage loss, and (5) recombination loss (adopted from [1])

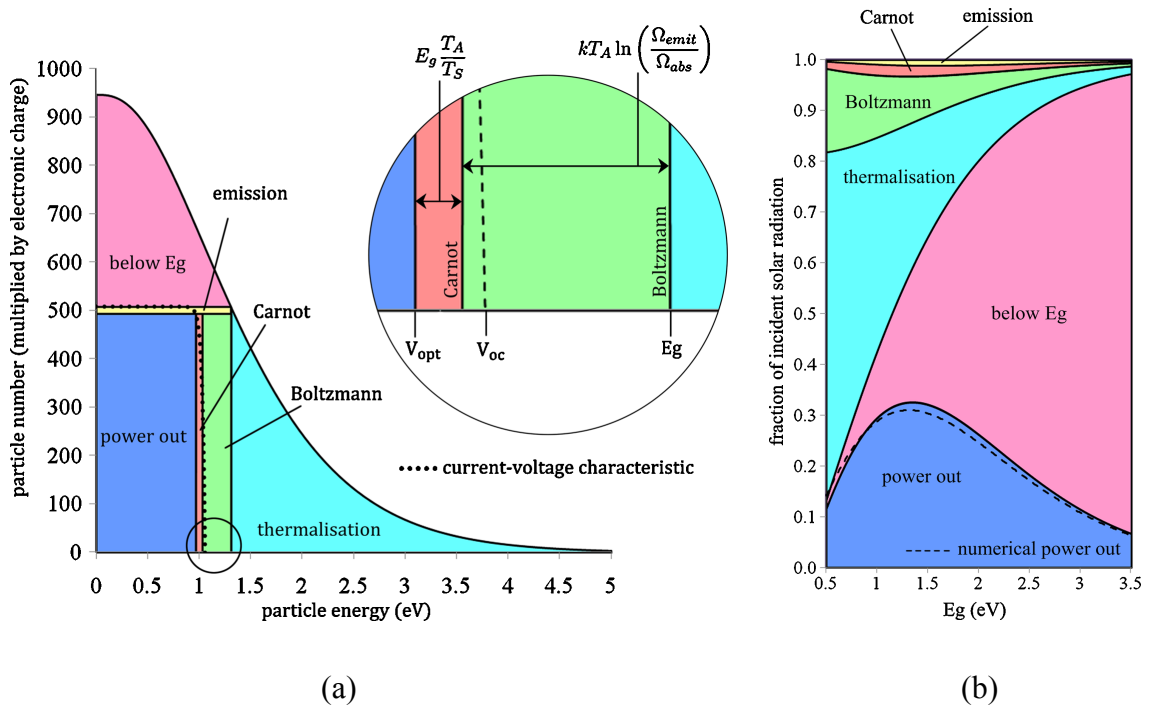


Figure 1.3 (a) Portions of intrinsic losses of a single junction solar cell with bandgap E_g in solar spectrum (one sun illumination) and (b) fraction of loss mechanisms as a function of bandgap (adopted from [5])

Currently, the highest efficiency of a single junction solar cell measured under the AM1.5 spectrum is 28.8% from a GaAs thin film solar cell [6], and the technology is almost reaching the theoretical upper limit.

1.2. Exceeding the Shockley-Queisser limit

In order to minimize the fundamental losses and to utilize the photon energy in the energy conversion process, many approaches have been proposed. The concepts are categorized into three groups [3]: (1) introducing multiple absorption bands, (2) capturing excited carriers without thermalization, and (3) modulating photon spectra. Examples of approach 1 are multi-junction solar cells and intermediate band solar cells, shown in Figure 1.4 (a) and (b), respectively. Details of the two devices are described in sections 1.3 and 1.4, respectively. Approach 2 is adopted for hot carrier solar cells and realized by multiple exciton generation shown in Figure 1.4 (c) and (d). In the hot carrier solar cells, photoexcited carriers (also called “hot carriers”) are extracted to energy selective contacts before losing their excessive kinetic energy as heat [7]. The multiple exciton generation reduces the thermalization loss by employing some of the energy of highly excited carriers to generate additional electron-hole pairs [8]. Approach 3 is implemented in the up/down converter shown in Figure 1.4 (e). The up converter emits a photon with energy greater than a bandgap of the solar cell by absorbing more than two sub-bandgap photons to reduce the transparent loss and enhance the short-circuit current. The down converter creates two (or more) sub-bandgap photons by modifying a photon with energy two times greater than the bandgap [9]. Theoretically the estimated efficiency of these new techniques exceeds the detailed balance limit of the single junction solar cell without contradicting the Shockley-Queisser limit.

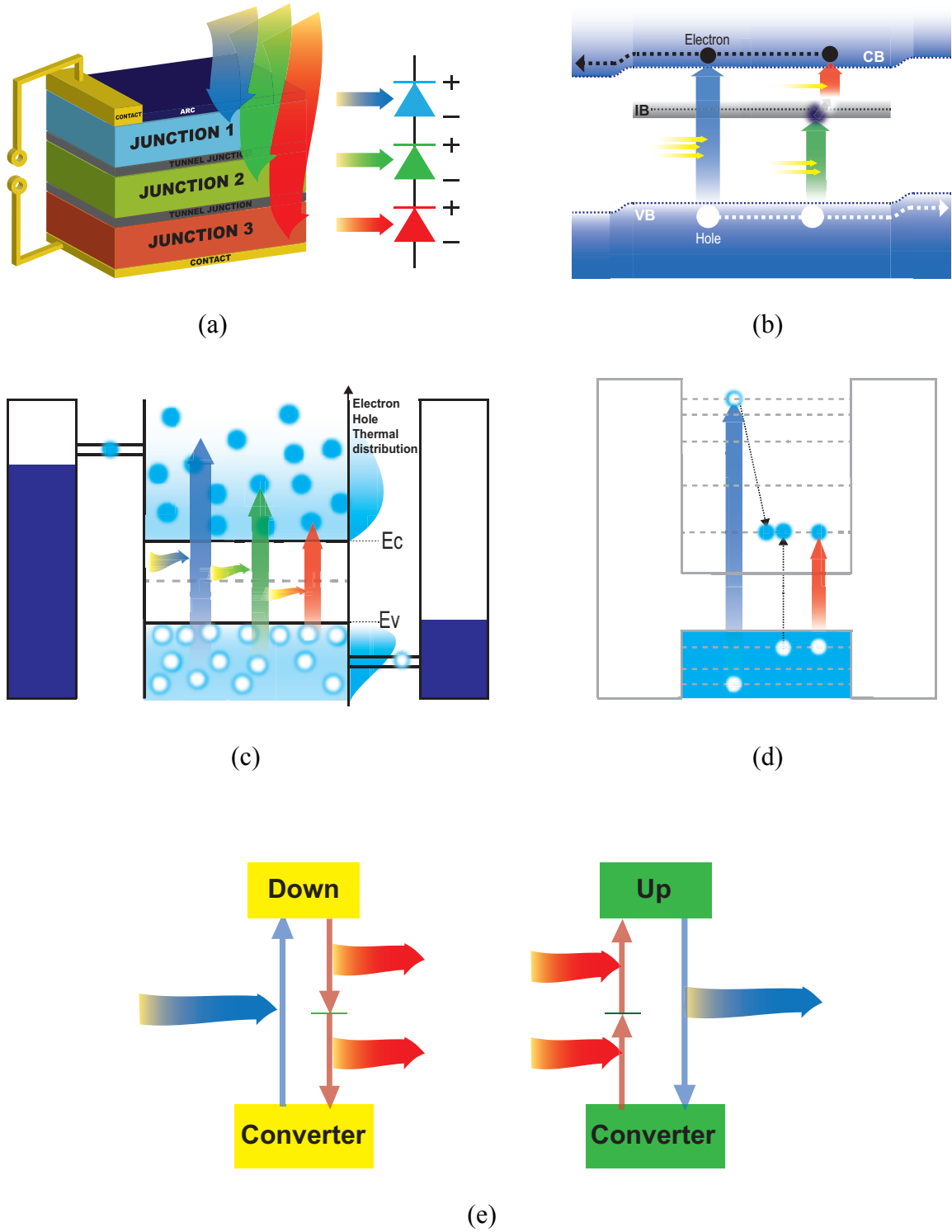


Figure 1.4 (a) Multi-junction solar cell, (b) intermediate band solar cell, (c) hot carrier solar cells, (d) multiple exciton generation, and (e) up/down converters

However, only the multi-junction solar cell has demonstrated an efficiency greater than the Shockley-Queisser limit for the single bandgap with the highest record being 43.5% (GaInP/GaAs/GaInNAs triple-junction cell, measured under 418 suns) [6].

1.3. Multi-junction solar cells

The multi-junction solar cell is built by stacking several p-n junctions in descending order of the bandgap of the semiconductor materials and connecting them in series, as shown in Figure 1.4(a). In the stack of single junction solar cells, a broad range of solar energy is absorbed selectively to minimize thermalization and transparent loss. For example, in the triple junction solar cell, the largest bandgap (E_{g1}) layer on top absorbs a portion of the solar spectrum whose energy is greater than E_{g1} while the lower energy photons reach the subsequent layer with the bandgap of E_{g2} ($< E_{g1}$). The middle layer also absorbs those photons with energy in a range between E_{g2} and E_{g1} , transmitting the remaining photons to the lowest layer with the bandgap of E_{g3} . After arriving at the bottom layer of the smallest bandgap (E_{g3}), photons with energy greater than E_{g3} are absorbed. Using this strategy allows the expansion of absorption spectrum to longer wavelengths without sacrificing the energy of short wavelength photons. Indeed, more energy of short wavelength photons can be harvested because the amount of thermalized energy can decrease when photons are absorbed in the material with bandgap energy closed to the photon energy.

The detailed balance limit of the triple junction solar cell is 51.2 % under AM1.5 spectrum and 63.2 % under fully concentrated light [10]. Clearly, higher maximum efficiency, up to 86.8%, can be achieved by increasing the number of the junctions in the solar cell to an infinite number of junctions under fully concentrated sunlight [10]. The

maximum theoretical limits of multi junction solar cells with more than three junctions are listed Table 1.1. However, in practice, the efficiency of the most successful multi-junction solar cell is 43.5% for a GaInP/GaAs/ GaInNAs solar cell under 418 suns [6]. Although it is currently the most efficient solar cell, it is still substantially below the theoretical upper limit of the multi-junction solar cell.

Table 1.1 Optimal bandgap of consisting junctions and maximum efficiency limit of multi-junction solar cells under AM1.5 Global radiation [10]

No. of junctions	E_1	E_2	E_3	E_4	E_5	E_6	η (%)
1	1.34						32.9
2	0.94	1.61					45.3
3	0.93	1.37	1.91				51.2
4	0.72	1.12	1.49	2.01			54.9
5	0.71	1.01	1.33	1.67	2.15		57.3
6	0.69	0.96	1.19	1.47	1.79	2.24	59.2

One of the major challenges in improving efficiency is obtaining high crystal quality of materials with optimal bandgap in Table 1.1. According to Table 1.1 a combination of materials with certain values of bandgap is needed to build an efficient multi-junction solar cell. Shown in Figure 1.5, III-V semiconductor alloys can cover the required bandgap range while providing high absorption and fast carrier transport. However, all lattice constants of alloys in the certain sets are not usually matched to the lattice constant of commercially available wafers such as Si, Ge, GaAs, InP, GaSb, InAs, etc. The lattice mismatch can cause a large density of dislocations in the monolithic epitaxial growth of the multi-layer heterostructure beyond the critical thickness of each layer, and the dislocation degrades the solar cell efficiency by enhancing non-radiative

recombination in the device. In particular, high quality materials near 1eV that are closely lattice matched to GaAs or Ge wafers which are essential for building efficient multi-junction solar cells with more than three junctions are hardly available. Therefore, because of the limitation in availability of material, in practice, efficiency of quadruple (or more) junction cells is still far below the efficiency of the triple junction solar cell.

[11]

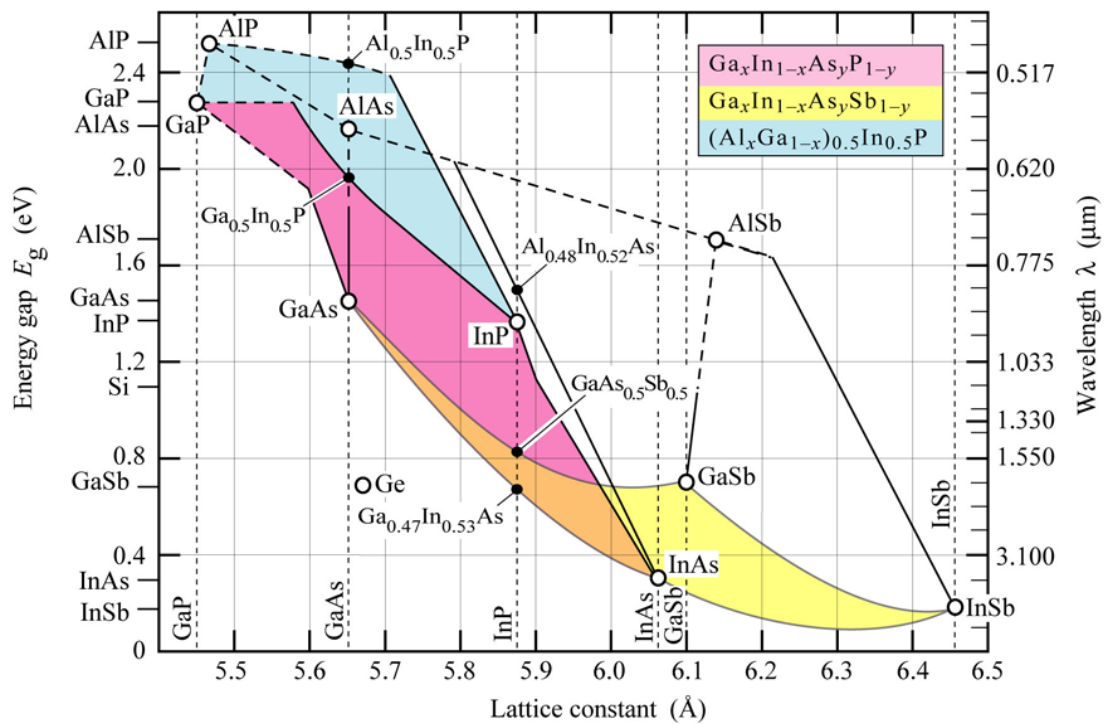
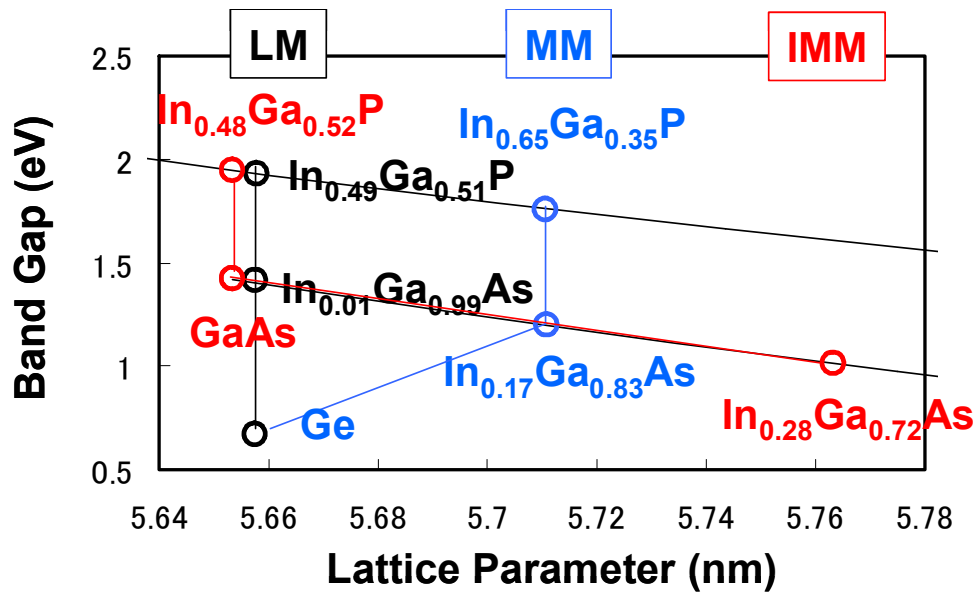


Figure 1.5 Relation between bandgap and lattice constant of ternary and quaternary III-V compound semiconductors (adopted from [12])

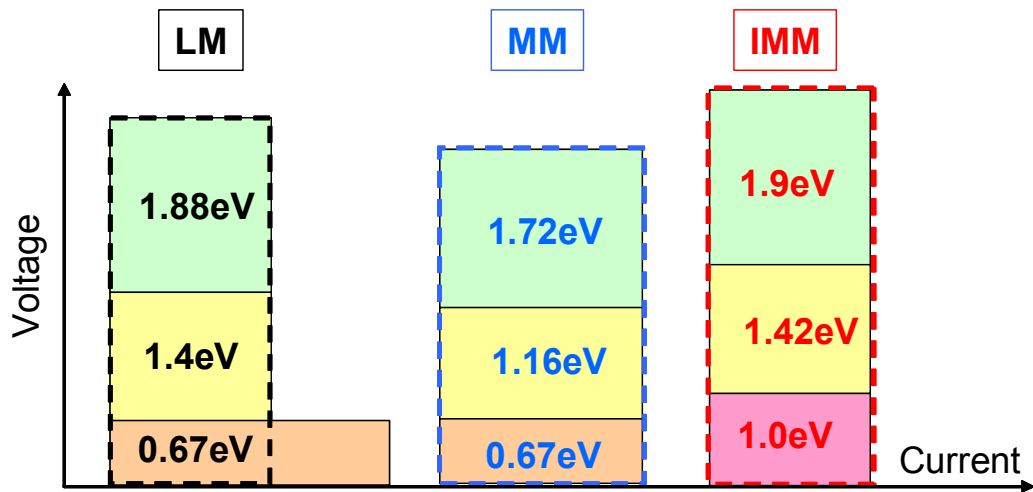
Due to the lack of lattice matched 1 eV materials, currently available triple junction solar cells are fabricated in three configurations: (1) lattice matched (LM) structure (2) upright metamorphic (MM) structure, and (3) inverted metamorphic (IMM) structure [13, 14]. Details of each structure are illustrated in Figure 1.6. In the LM

structure, lattice constants of all sub-cells are closely matched to the Ge substrate, but current matching conditions cannot be satisfied because the bandgaps of sub-cells are not the optimal values, especially in the bottom Ge cell. To balance the current from each sub-cell, the bandgaps of the top and middle cells of the MM structure are reduced, providing a combination of better theoretical efficiency with the Ge substrate. However, the bandgap of each sub-cell is still not the optimum value, and a precise buffer layer is required between the Ge bottom cell and the InGaAs middle cell to avoid misfit dislocations due to the lattice mismatch between these two layers. To minimize the effect of lattice mismatch in the epitaxial growth, the IMM structure is introduced, in which the lattice mismatched bottom layer is grown last. On the GaAs wafer, lattice matched InGaP (top) and GaAs (middle) layers are grown first, and then a precise buffer layer is grown to avoid misfit dislocations in the following InGaAs (bottom) layer. The final epitaxial structure is separated from the GaAs wafer, and the thin film is mounted to a handling substrate in reverse. With this fabrication method, high quality top and middle layers can be grown despite the lattice mismatch of the bottom layer, and materials with bandgaps close to the optimal value can be chosen. In addition, the thin-film technology allows for reducing material usage, resulting in lower fabrication costs.

Recently, GaInNAs has been introduced as a bottom sub-cell, the bandgap of which is close to 1 eV while being lattice matched to GaAs. However, this material still has the problem of short diffusion length (shorter than $0.4\mu\text{m}$) causing a low short-circuit current (J_{sc}) [15], so the efficiency of the triple junction solar cell (GaInP/GaAs/GaInNAs) is not enhanced substantially compared to other triple junction solar cells.



(a)



(b)

Figure 1.6 (a) Bandgaps and lattice parameters of composite semiconductors and (b) voltage and current for each sub-cells in the triple junction solar cells (adopted from [14])

As an alternative solution to the “1 eV material problem” of the multi-junction solar cells, a type-II GaAsBi/GaAsN superlattice is presented in CHAPTER 2, the effective lattice constant of which is the same as the GaAs lattice constant. Electronic and optical characteristics of the material system are studied to estimate its benefit in photovoltaic applications.

1.4. Intermediate band solar cells

Intermediate band solar cells (IBSC) have been developed to surmount the Shockley-Queisser limit of a single junction solar cell by accommodating sub-bandgap photon absorption via absorption bands within the bandgap of the host material while preserving the open circuit voltage (V_{oc}). As Figure 1.4 (b) shows, after one sub-bandgap photon excites an electron from the valence band to the intermediate band, another sub-bandgap photon excites the electron in the intermediate band to the conduction band. In principle, the final potential energy of the electron-hole pair from the two successive excitations is same as the electron-hole pair created by the photon above the bandgap energy in a single junction solar cell of the host material. Therefore, the short circuit current (J_{sc}) can increase through the additional absorption process of sub-bandgap photons while maintaining the same V_{oc} as the single junction solar cell of the host material. The detailed balance limit of the IBSC with one intermediate band is 63.1% under full concentration, assuming an electronically isolated IB and no overlap in absorption spectra between the three transitions [16]. Although the theoretical maximum efficiency is comparable with that of the triple junction solar cell under full concentration, the limit efficiency of the IBSC can be realized with only one junction providing the advantage of simple fabrication. Moreover, the current matching condition

in the IBSC is less constricted than in the multi-junction solar cell, resulting in less spectral sensitivity because the sub-bandgap photon process occurs in parallel with the normal single junction solar cell operation of the host material. However, in practice, most intermediate bands are not electronically isolated from the conduction or valence bands of the host material at room temperature [17], and the coefficients of non-overlapping absorption of all transitions in the IBSC are difficult to realize, which are automatically achieved in the vertically stacked multi-junction solar cell.

To introduce intermediate bands within a bandgap, two approaches have been proposed [18]: (1) employing highly mismatched semiconductor alloys (HMA) as an absorption layer and (2) incorporating quantum dots (QDs) inside the semiconductor. In the HMA, the band-anticrossing model suggests that interaction between impurity states and the conduction (valence) band leads to the split of the conduction (valence) band into E_+ and E_- , shown in Figure 1.7 [19]. In this band structure, E_- can be the intermediate band because it has a narrow density of states and is located in between two extended bands, E_+ and E_v . Examples of the HMAs are $\text{GaN}_x\text{As}_{1-x-y}\text{P}_y$ and $\text{Zn}_{1-y}\text{Mn}_y\text{O}_x\text{Te}_{1-x}$. Recently, IBSCs made of GaAsN (2.4% of N) [20] and ZnTe:O [21] have been reported, and optical transitions from IB (or E_-) to the conduction band (or E_+) and from the valence band to IB have been demonstrated with the results from the electroluminescence measurement [20]. However, the efficiencies of HMA-IBSCs are still far below those of their reference cells.

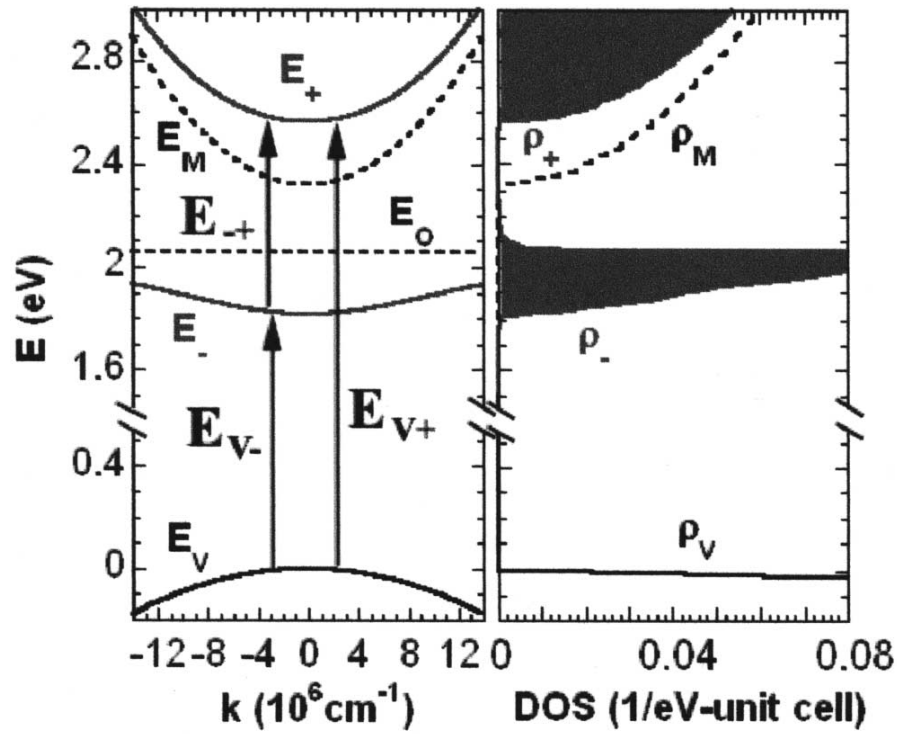


Figure 1.7 The calculated energy of band structure (left) and density of states (right) for $\text{Zn}_{0.88}\text{Mn}_{0.12}\text{O}_{0.01}\text{Te}_{0.99}$ based on the band anticrossing model (adopted from [19])

In the QD approach, the confined states of QDs can be the intermediate band of an IBSC described in Figure 1.8, because of their discrete atomic-like density of states. Recently, InAs/GaAs QD-IBSC [22] and GaSb/GaAs QD-IBSC [23] have demonstrated the sub-bandgap response and enhancement in J_{sc} . However, the efficiency of the most successful QD-IBSC made of InAs/GaAs QD-IBSC was 13.8% [22], and that value is still far below of the efficiency of a single junction GaAs solar cell (28.3% under one sun). One of the biggest challenges of the InAs/GaAs QD-IBSC is a strong thermal connection between the conduction band and the QD [17] levels due to excessive thermal emission rates of carriers in QDs leading to V_{oc} degradation. In addition, mismatches in optical transition rates associated with the IB (fast transition rate from the IB to

conduction band and slow transition rate from valence band to the IB) makes the two photon processes via the intermediate band inefficient, resulting in suppression of J_{sc} improvement. To mitigate these problems, GaSb/GaAs QDs with a type-II band alignment are proposed in this project. Because of a deep potential well in the type-II band alignment, the thermal emission rate of carriers in GaSb QD is expected to be lower than in the InAs QDs with type-I band alignment. In addition, two optical transition rates associated with the IB in the type-II alignment can be better matched to each other because of the spatial separation of electrons and holes. The electronic and optical properties of the QDs, thermal emission rates of carriers in the QDs, and the intermediate band solar cell fabricated with the material system are reported in CHAPTER 3, CHAPTER 4, and CHAPTER 5, respectively.

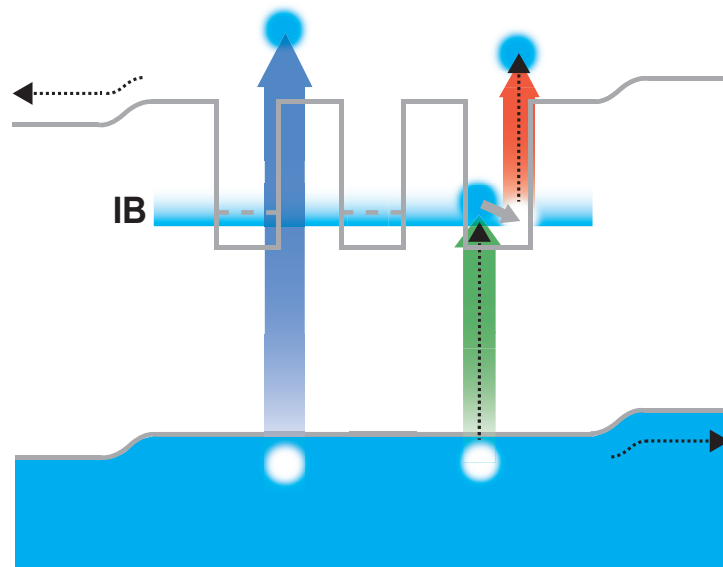


Figure 1.8 Schematic diagram of an IBSC constructed by InAs/GaAs QDs

1.5. Thesis outline

In CHAPTER 2, the miniband structure and effective bandgap for strain-balanced GaAsBi/GaAsN superlattices with effective lattice match to GaAs are calculated for alloy compositions up to 5% Bi and N using the k.p method. Based on the results, the joint density of states and optical absorption of a 40Å/40Å GaAs_{0.96}Bi_{0.04}/GaAs_{0.98}N_{0.02} superlattice are reported, demonstrating a ground state transition at 1.005eV and first excited transition at 1.074eV.

In CHAPTER 3, details of electronic structure and optical properties of the GaSb QDs are studied based on 8-band k.p model, and the some of results are compared with the previously reported experimental results to validate the assumptions and theoretical methods used in this study.

In CHAPTER 4, the electronic structure and thermal emission of carriers from the QD states are studied for the type-II GaSb/GaAs quantum dots using the admittance spectroscopy measurement. The measured thermal emission rates are compared to the optical transition rates from the VB to the QD states under the various concentration of the solar irradiation.

In CHAPTER 5, GaSb/GaAs QD-IBSCs are fabricated to present the utilization of the type-II QDs on the solar energy conversion in the IBSCs, and the device structure optimization are presented to improve the conversion efficiency of the solar cells.

CHAPTER 2

Band structure of strain-balanced GaAsBi/GaAsN superlattices on GaAs

2.1. Introduction

Semiconductor alloys compounds with large electronegativity variation, often termed highly mismatched alloys, possess dramatic changes in electronic and optical properties with only small alloy concentrations. High-mismatched alloys of GaAsBi and GaAsN have received much attention due to their wide range of achievable bandgap energy. GaAsN with dilute nitrogen content has demonstrated materials with desired narrow bandgap properties [24] resulting from shifting the conduction band edge relative to GaAs, though their use in device applications has been limited due to substantial degradation of electron mobility in the material [25]. GaAsBi similarly offers a means of shifting the bandgap relative to GaAs [26], primarily through altering the valence band edge. Heterojunctions of GaAsN/GaAsBi are expected to have a type-II band lineup, and provide a further range of bandgap energy and a means of engineering carrier transport [27]. Furthermore, GaAsBi/GaAsN superlattices would offer a means for strain-balanced structures on technologically important GaAs substrates due to compressive/tensile strain for GaAsBi/GaAsN materials. The bandgap versus lattice constant relationships for GaAsBi and GaAsN and schematic concept for the GaAsBi/GaAsN superlattice are

shown in Figure 2.1. In this work, the bandstructure of strain-balanced GaAsBi/GaAsN are calculated using for varying alloy composition and superlattice layer thickness to determine realistically achievable effective bandgap energies for this material system. The results of the bandstructure calculations are then used to determine the near-bandedge density of states and optical absorption coefficient.

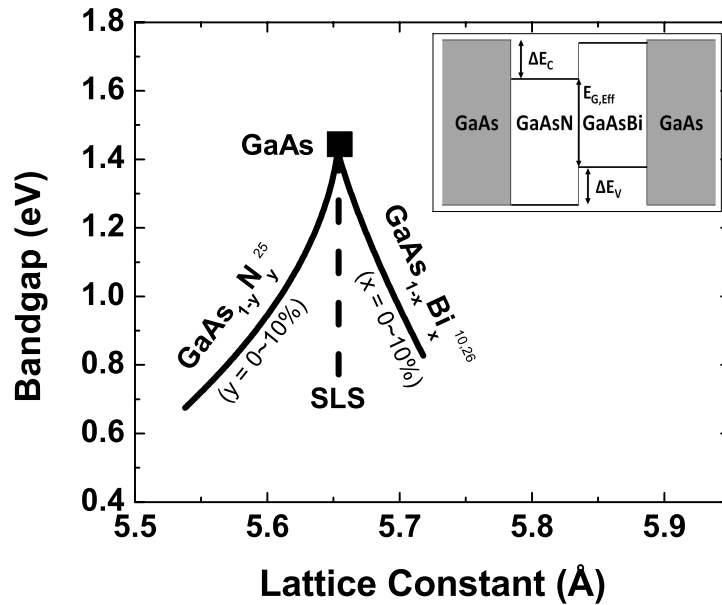


Figure 2.1 Bandgap energy versus lattice constant for GaAsN [28] and GaAsBi [29, 30] dilute alloys and (inset) schematic of strain-balanced GaAsBi/GaAsBi superlattice with effective lattice match to GaAs.

2.2. Methods

2.2.1. Overview

The electronic bandstructure of GaAsBi/GaAsN strain-balanced superlattices with (001) crystal orientation was calculated using an 8-band k.p method, and compared to the self-consistent solution to the Schrodinger and Poisson equations [31]. Superlattice period and thickness were varied for structures that were strain-balanced with an effective

lattice match to GaAs, for Bi and N content up to 5%. Details for the calculation methods and material parameters are described in the following.

2.2.2. Material parameters

Lattice constants and elastic constants of GaAsBi and GaAsN layer were obtained using the virtual crystal approximation with the parameters of GaAs [32], GaN [32], and GaBi [33]. Results of theoretical studies were used for GaBi, where experimental data is on this material is generally lacking [33]. It should be noted that the alloy compositions studied in this work are well within the range of previously achieved values of 5% for GaAsN [34, 35], 10% for GaAsBi [36], and agree with prior experiments that follow the band anticrossing model [29, 37]. GaAs material with dilute concentrations of Bi results in a bandgap reduction primarily resulting from a valence band shift, which may be explained by the valence-band anticrossing (VBAC) model [29]. The valence band maximum for GaAsBi was calculated by applying the VBAC model

$$E_V = \frac{E_{Bi} + H_{GaAs} + \sqrt{(H_{GaAs} - E_{Bi})^2 + 4C_{Bi-GaAs}^2 x}}{2} \quad (2.1)$$

with

$$H_{GaAs} = -\frac{\hbar^2}{2m_0} [(k_x^2 + k_y^2)(\gamma_1 + \gamma_2) + k_z^2(\gamma_1 - 2\gamma_2)] + \Delta E_{VBM} x \quad (2.2)$$

where $E_{Bi} = 0.4eV$, $C_{Bi-GaAs} = 1.55eV$, and $\Delta E_{VBM} = 0.8eV$. Concurrently, the conduction band minimum of GaAsBi layer was approximated using the virtual crystal approximation

$$E_C = E_g(GaAs) - \Delta E_{CBM} x \quad (2.3)$$

where $\Delta E_{CBM} = E_C(GaAs) - E_C(GaBi) = -2.1eV$. In contrast, GaAs with dilute nitrogen concentration results in a bandgap reduction primarily resulting from a shift in the conduction band minimum. The bandgap energy and band alignment can be similarly described by the conduction-band anticrossing (CBAC) model given by[37]

$$E_C = \frac{E_N + E_{C,GaAs} - \sqrt{(E_N - E_{C,GaAs})^2 + 4C_{N-GaAs}^2}}{2} \quad (2.4)$$

where $E_N = 1.65eV$ and $C_{N-GaAs} = 2.7eV$. The GaAsBi/GaAsN superlattice has a corresponding type-II band lineup with a potential well for electrons and holes in GaAsN and GaAsBi layers, respectively. It should be noted that GaAsN exhibits significant deviations from the BAC model due to disorder in the alloy system, where N-cluster states and related interactions between N-states alter the bandstructure. A closer fit to experimental data is provided by the linear combination of resonant nitrogen states (LCINS) model [38-40], Similar behavior may also occur for GaAsBi, though the materials growth technology is still in its infancy. The BAC model was employed in this work in order to provide a more direct interpretation of trends related to the type-II superlattice bandstructure that are not clouded by deviations related to effects described in LCINS and similar models, or deviations related to material synthesis methods. Furthermore, the BAC model has been shown to provide excellent agreement for the bandgap energy of both GaAsN [37] and GaAsBi [29] relevant to the superlattice calculations presented in this work.

2.2.3. Strain balanced criteria

Strain-balanced superlattices were investigated for structures with individual layer thickness of up to 100\AA , which is below the critical thickness predicted by the Matthews-

Blakeslee model [41]. Alternating layers of tensile (GaAsN) and compressive (GaAsBi) strain can be used to minimize the total average strain energy of the superlattice, where the condition of zero average in-plane can be achieved based on the relations [42]

$$t_1 A_1 \varepsilon_1 a_2 + t_2 A_2 \varepsilon_2 a_1 = 0 \quad (2.5)$$

$$a_0 = \frac{A_1 t_1 a_1 a_2^2 + A_2 t_2 a_2 a_1^2}{A_1 t_1 a_2^2 + A_2 t_2 a_1^2} \quad (2.6)$$

$$A = C_{11} + C_{12} - \frac{2C_{12}^2}{C_{11}} \quad (2.7)$$

where a_0 , a_1 , and a_2 represent lattice constants ($a_1 > a_0 > a_2$) for the substrate with constant a_0 , and t_1 and t_2 define the thickness of each layer. According to these relations, strain-balanced GaAsBi/GaAsN superlattices with effective lattice match to GaAs can be obtained by controlling the thickness of GaAsBi and GaAsN layers. Figure 2.2 shows a series of Bi and N compositions in GaAsBi and GaAsN, respectively, which satisfy the strain-balanced criteria in the superlattice for several ratios of layer thickness. In the following calculations, 4% Bi and 2.1% N is chosen under the strain-balanced condition corresponding to equivalent thickness of the GaAsBi and GaAsN layers.

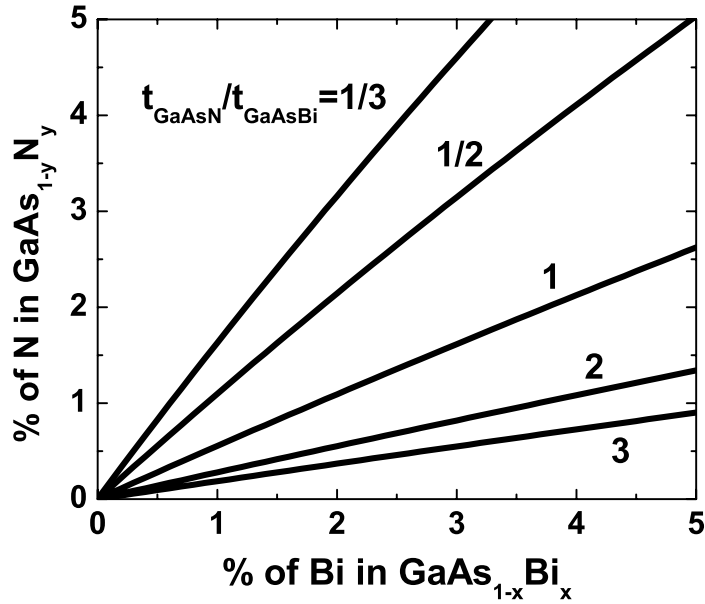


Figure 2.2 Strain balanced composition of Bi and N for several thickness ratios of GaAsBi and GaAsN layers.

2.2.4. Band-structure calculation by the k.p method

The energy band structure and wave functions of the superlattice were calculated using 8-band k.p perturbation theory within the envelope function approximation, which is suitable for describing the band structure near the zone center where the envelope function is slowly varying [43, 44]. The k.p methodology has been similarly applied to GaInNAs [45] and type-II GaAsN/GaAsSb [46] quantum wells demonstrating good agreement with experimental measurements. In future work, the k.p model may also be adapted to account for interactions between nitrogen (or bismuth) states based on experimental or first-principles calculations; as has been done previously for GaInAsN/GaAs quantum wells [47]. In this approximation, two 8x8 k.p Hamiltonian

matrices describing the band structure of the bulk constituent material satisfy the relation[48]

$$H^i \Psi_j(\mathbf{r}) = e_j \Psi_j(\mathbf{r}) \quad \left\{ \begin{array}{l} i = GaAsBi, GaAsN \\ j = CB, HH, LH, SO \end{array} \right\} \quad (2.8)$$

in each layer, where terms representing energy band offsets and hydrostatic and shear strain effects were included in the matrix elements. The wave function $\Psi_j(\mathbf{r})$ was expanded in the basis set of cell-periodic wave function expressed by

$$\Psi_j(\mathbf{r}) = \sum_j f_j(z) \exp(ik_x x) \exp(ik_y y) |j\rangle \quad (2.9)$$

where $f_j(z)$ is the envelope function of j-th band of the superlattice and $|j\rangle$ is the Kane basis function of the zinc-blend structure satisfying the relation

$$\Psi(\mathbf{r} + \mathbf{d}) = \exp(i\mathbf{q} \cdot \mathbf{d}) \Psi(\mathbf{r}) \quad (2.10)$$

where \mathbf{d} is period of the superlattice and \mathbf{q} is the superlattice wave vector. In addition, the envelope function and the first derivative of $f_j(z)$ are required to be continuous at the interface between the constituent materials of the superlattice. In this work, additional assumptions of the Hamiltonian parameters for the conduction band Kane parameter F , Kohn-Luttinger parameter γ_1 , γ_2 , and γ_3 , and the matrix elements of the momentum operator between conduction and valence band $\langle s | p_x | x \rangle$ were assumed to be equivalent to GaAs [32] due to lack of available data for GaAsBi and GaAsN, and expectation that variation in these parameters would be insignificant across the range of dilute alloy compositions studied.

The envelope function approach of the 8-band k.p method provides a set of eight coupled second order differential equation in the variable z , where k_z is replaced by

$-i\partial/\partial z$. The equations were solved numerically using a transfer-matrix algorithm [48].

The coupled differential equations may be written as

$$\sum_{j=1}^8 \left[A_{ij} \frac{\partial^2}{\partial z^2} - iB_{ij} \frac{\partial}{\partial z} + C_{ij} \right] f_j(z) = \varepsilon f_i(z) \quad i=1,2,\dots,8 \quad (2.11)$$

and modified to first order coupled differential equations using a new 16x1 column vector, $\Phi(z)$ given by

$$\Phi_i(z) = \begin{cases} f_i(z) & i=1,2,\dots,8 \\ \sum_{j=1}^8 -A_{ij} \frac{\partial f_j}{\partial z} - iB_{ij} f_j(z) & i=9,10,\dots,16 \end{cases} \quad (2.12)$$

satisfying the relation

$$\frac{\partial \Phi(z)}{\partial z} = \begin{pmatrix} -iA^{-1}B & -A^{-1} \\ \varepsilon - C & 0 \end{pmatrix} \Phi(z) \quad (2.13)$$

Because the solution of the first order homogeneous differential equation is exponential, the solution of equation (2.13) can be described by the exponential matrix

$$\Phi(z) = \exp \left[\begin{pmatrix} -iA^{-1}B & -A^{-1} \\ \varepsilon - C & 0 \end{pmatrix} z \right] \Phi(0) \quad (2.14)$$

where the solution is continuous at the interface between the layers. Energy eigenvalues, ε , are obtained according to the translational symmetry of the superlattice. If d is a period of the superlattice, $\Phi(z)$ and the wave function of the superlattice should follow the relation

$$\Phi(d) = \exp(iqd)\Phi(0) \quad (2.15)$$

where q is the superlattice wave vector in the growth direction. The eigenvalue problem may then be described by

$$\exp\left[\left(\begin{array}{cc} -iA^{-1}B & -A^{-1} \\ \varepsilon - C & 0 \end{array}\right)d\right]\Phi(0) = \exp(iqd)\Phi(0) \quad (2.16)$$

to calculate the energy band structure and wave functions for the superlattice.

2.2.5. Mini-band structure with Self-consistent solution of Schrödinger-Poisson equations

The spatial dependence of mini-bands in superlattices with finite periods was also investigated using one-dimensional calculation of the self-consistent solution of Schrödinger-Poisson equations [31, 49]. The superlattice mini-band profile was determined in this method including strain effects, where the Schrödinger equation was solved to obtain energy eigenvalues and wavefunctions of the superlattice based on the transfer matrix formulation. The superlattice structure was divided by N segments, where the time independent Schrödinger equation for the i -th segment is written as [50]

$$\frac{d^2}{dz^2}\Psi_i(z) + \tilde{\kappa}_i^2\Psi_i(z) = 0 \quad (z_{i-1} \leq z \leq z_i) \quad (2.17)$$

with the boundary conditions

$$\Psi_{i-1}(z_{i-1}) = \Psi_i(z_{i-1}) \quad (2.18)$$

$$\frac{1}{m_{i-1}^*} \frac{d}{dz} \Psi_{i-1}(z_{i-1}) = \frac{1}{m_i^*} \frac{d}{dz} \Psi_i(z_{i-1}) \quad (2.19)$$

where $\tilde{\kappa}_i = \sqrt{\frac{2m_i^*}{\hbar^2}(E - V_i)}$ and m_i^* is the effective mass of charge carriers in i -th layer.

Considering the boundary conditions and combining all relations between two adjacent layers, the 0-th and (N+1)-th layer can be related as

$$\left(\begin{array}{c} \Psi_0(z_0) \\ \frac{1}{m_0^*} \frac{d}{dz} \Psi_0(z_0) \end{array}\right) = \mathbf{M} \times \left(\begin{array}{c} \Psi_{N+1}(z_{N+1}) \\ \frac{1}{m_{N+1}^*} \frac{d}{dz} \Psi_{N+1}(z_{N+1}) \end{array}\right) \quad (2.20)$$

$$\mathbf{M} = \prod_{i=1}^N \begin{pmatrix} \cos(\tilde{\kappa}_i \cdot d_i) & -\frac{m_i^*}{\tilde{\kappa}_i} \sin(\tilde{\kappa}_i \cdot d_i) \\ \frac{\tilde{\kappa}_i}{m_i^*} \sin(\tilde{\kappa}_i \cdot d_i) & \cos(\tilde{\kappa}_i \cdot d_i) \end{pmatrix} \quad (2.21)$$

to determine Ψ and E . In this work, the numerical calculation of the transfer method formulation was performed using the argument principle method [50].

The results from the Schrödinger equation solution can be used to calculate the carrier distribution in the superlattice and may then be incorporated in the Poisson equation [49]

$$\frac{d}{dz} \left(\epsilon_s(z) \frac{d}{dz} \right) \phi(z) = -\frac{q}{\epsilon_0} [n(z)] \quad (2.22)$$

where $\epsilon_s(z)$ is dielectric constant and $\phi(z)$ is electrostatic potential distribution which satisfies the relation

$$V(z) = -q\phi(z) + \Delta E(z) \quad (2.23)$$

where ΔE defines the band offset at the interfaces of the superlattice. The calculations were performed iteratively until the results of the Schrödinger and Poisson equations converged.

The electron effective mass of GaAsBi and the hole effective mass of GaAsN were assumed to be equal to GaAs effective mass values since the conduction band and valence band are almost unchanged when small amount of Bi and N are incorporated in GaAs, respectively [51, 52]. The electron effective mass of GaAsN was obtained based on the relation [37]

$$m_{eff}^*(E) = m_{GaAs}^* \left\{ 1 + \frac{C_{N-GaAs}^2 x}{(E_N - E)^2} \right\} \quad (2.24)$$

The hole effective mass of GaAsBi is not well known, where predictions have only estimated that the values would be higher than that of GaAs [26]. In this work, the heavy hole and light hole effective mass were assumed to be $m_{hh}^*=0.55$ and $m_{lh}^*=0.10$, respectively.

2.2.6. Absorption coefficient

The near-band edge density of states and optical absorption coefficient were studied due to their major importance for device applications. The calculations of these parameters were all based on the results from the k.p bandstructure calculations. From the dispersion relations, constant transition energy surface in k-space can be obtained. By evaluating the volume between two adjacent surfaces which represent transition energy E and $E + dE$, and dividing it by the volume in which each electron state occupies, the joint density of states of the superlattice was obtained. The absorption coefficient is given by [53]

$$\alpha(\hbar\omega) = \frac{2\pi}{\hbar} \frac{e^2}{m_0^2} \left(\frac{\hbar}{2\omega n_r c \epsilon_0} \right) \sum_{n,n'} \int d\mathbf{K} \left| \langle n, \mathbf{K} | p_x | n', \mathbf{K} \rangle \right|^2 \delta(E_n(\mathbf{K}) - E_{n'}(\mathbf{K}) - \hbar\omega) \quad (2.25)$$

neglecting the Coulomb interaction between electrons and holes, and considering only x-polarized light (normal incidence to the superlattice). The delta function in the integration was evaluated by counting the number of states at \mathbf{K} , and the number of states was multiplied by the matrix element of momentum operator, $\langle n, \mathbf{K} | p_x | n', \mathbf{K} \rangle$. With the envelope function approximation of the superlattice wavefunction, the matrix element of the momentum operator can be written as [54]

$$\langle n, \mathbf{K} | p_x | n', \mathbf{K} \rangle = \sum_{j,j'} \langle j, n | p_x | j', n' \rangle \int_0^d f_{j,n}^*(\mathbf{K}, z) f_{j',n'}(\mathbf{K}, z) dz \quad (2.26)$$

where the p_x is the momentum operator $-i\hbar\frac{\partial}{\partial x}$, and $f_{j,n}(z)$ represents the envelope function of the j -th basis of the n -th band. For the term $\langle j,n|p_x|j',n'\rangle$, only the $\langle x|p_x|s\rangle$ term is a nonzero, and was assumed to be equivalent to GaAs for the small composition of Bi and N in this work. The value of the matrix element for the momentum operator was obtained from

$$E_p = \frac{2}{m_0} |\langle x|p_x|s\rangle|^2 \quad (2.27)$$

where E_p for GaAs was assumed to be 28.8eV from Ref. [32].

2.3. Results and Discussion

2.3.1. Bandstructure

A representative bandstructure for a $\text{GaAs}_{0.96}\text{Bi}_{0.04}/\text{GaAs}_{0.979}\text{N}_{0.021}$ superlattice with 80Å period thickness calculated by the k.p method is shown in Figure 2.3. The conduction band contains one confined miniband (CB1) and a continuum of states at the edge of the conduction band offset. The valence band contains confined minibands corresponding to the first heavy hole (HH1), the first light hole (LH1), and the second heavy hole (HH2). The effective bandgap energy for this superlattice, defined as the energy separation between lowest energy states in the conduction and valence band (CB1-HH1), shows a value of 1eV. It should be noted that this effective bandgap energy has not been previously achieved for a lattice matched III-V system to GaAs. While strained quantum well and quantum dot systems have succeeded in achieving such narrow bandgap materials on GaAs, they do not offer a means for achieving sufficiently thick active layers that are required for devices such as solar cells and photodetectors.

The energy-momentum relations are shown for both the in-plane directions and the direction normal to the superlattice. For the in-plane direction, the bandstructure is isotropic for k_x and k_y , while the curvature differs dramatically for the direction normal to the superlattice. The range of effective bandgap energies achievable for the GaAsBi/GaAsN superlattice were investigated by varying the alloy composition up to 5% and superlattice period up to 100Å with equivalent thickness for the GaAsBi and GaAsN layers. The variation in effective bandgap spans from 0.89eV to 1.32eV in this range, as shown in Figure 2.4. The superlattice bandstructure was found to be primarily dependent on the superlattice period, strain parameters, and bandgap energy and band offsets of the materials. These parameters have a high degree of certainty for these calculations.

Uncertain parameters for the k.p calculations include the matrix element of the momentum operator E_p and Kohn-Luttinger parameters γ_1 , γ_2 , and γ_3 , which may be significantly altered in GaAsN and GaAsBi dilute alloys. Calculations were performed with large variations in these parameters to determine their influence on the calculated bandstructure and effective bandgap. Varying parameters E_p (for GaAsN, conduction band states) γ_1 , γ_2 , and γ_3 (for GaAsBi, valence band states) by up to a factor of 2 for the GaAs_{0.096}Bi_{0.04}/GaAs_{0.979}N_{0.021} superlattice results in a similar result, with a deviation of <5% for the effective bandgap. The small deviation suggests a relatively low sensitivity of the results presented to the chosen k.p parameters.

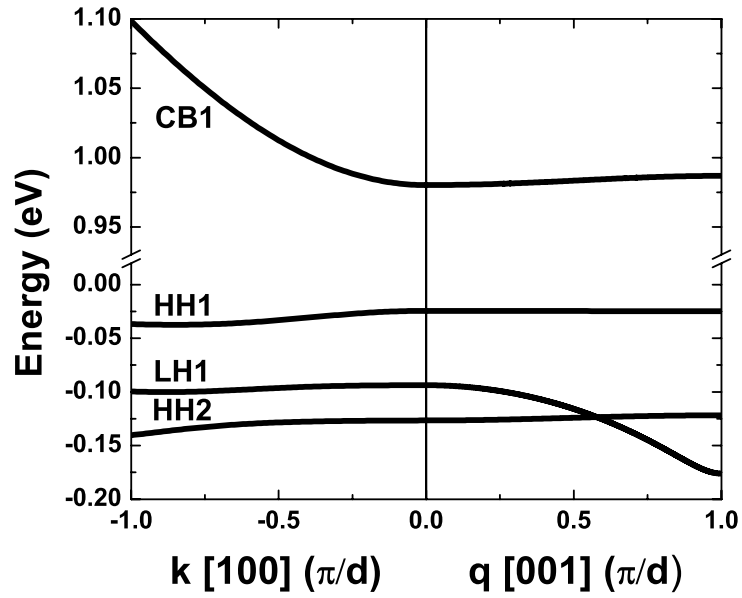


Figure 2.3 Miniband structure of $40\text{\AA}/40\text{\AA}$ GaAs_{0.96}Bi_{0.04}/GaAs_{0.979}N_{0.021} superlattice with effective bandgap energy of 1eV.

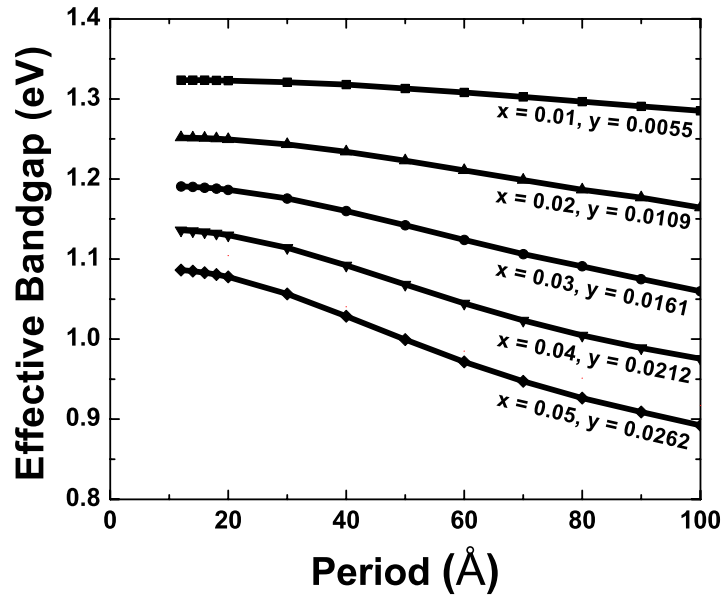


Figure 2.4 Effective bandgap energy for GaAsBi/GaAsN superlattices with matched layer thickness, varying period thickness and variable alloy composition.

2.3.2. Effective mass

The electron and hole effective masses in the superlattice growth direction can be calculated for these structures assuming parabolic relationships near the band edge according to the relation

$$\frac{1}{m^*} = \frac{1}{\hbar^2} \frac{d^2 \epsilon}{dk^2} \quad (2.28)$$

The effective mass of electrons and holes increases as the superlattice period increases, as shown in Figure 2.5. This increase is consistent with a decrease in tunneling probability with increasing layer thickness. This trend is more pronounced in the valence band for the range of composition and period examined, with an increasing dependence on period for larger Bi/N alloy compositions. The effective mass for the conduction band demonstrates a cross-over point at a period of approximately 60 Å, reflecting the transition from smaller effective mass dominated by GaAsN behavior at small period thickness to larger effective mass dominated by decreased tunneling probability at large period thickness.

2.3.3. Spatial Distribution of Wavefunctions

Varying finite total thickness of the superlattices was investigated between 5 to 15 periods using the Schrödinger-Poisson self-consistent solution in order to evaluate the influence of finite structures and number of periods on effective bandgap. The spatial distribution of wave-functions for a 10 period (80Å period) GaAs_{0.096}Bi_{0.04}/GaAs_{0.979}N_{0.021} superlattice with GaAs layers at both ends are shown in Figure 2.6. The effective bandgap energy of the superlattice is 1eV, with four confined states in the bound state region (CB1, HH1, LH1, and HH2). The conduction and the first heavy hole

band levels are in agreement with the results of the k.p calculations, while the first light hole and the second heavy hole band levels differ by approximately 30meV. The discrepancy for the position of the first light hole and the second heavy hole states is attributed to assumed values for the hole effective mass in GaAsBi required to evaluate the Schrödinger equation using the transfer-matrix formalism, while these values are not required for the k.p calculations. Although the hole effective mass of GaAsBi is expected to be larger than the hole effective mass of GaAs, the value is still unknown due to lack of theoretical and experimental data. In this work, the hole effective mass of GaAsBi was used as a fitting parameter to match the transition energy for effective bandgap energy obtained by k.p, resulting in values of $0.55 m_0$ and $0.10 m_0$ for heavy hole and light hole mass, respectively. In addition, the effective bandgap energy is found to match the k.p prediction of 1.000eV, with a variation of approximately 1.001eV to 1.004eV varying between 5 and 15 periods.

The spatial dependence of the wavefunctions is also examined using results of the k.p method due to the importance on optical properties. The square of the envelope function of the superlattice at $k_x = k_y = q = 0$ is shown as a function of the superlattice normal direction in Figure 2.7. The s component of the conduction band and x component of the valence band envelope functions are shown, corresponding to the primary components that are coupled with optical radiation at normal incidence to the superlattice. The s and x designation indicate the component of the zinc-blend zone-center cell-periodic basis function. The electrons and holes are primarily confined in the GaAsN and GaAsBi layers, respectively, with significant overlap near the GaAsBi/GaAsN interfaces.

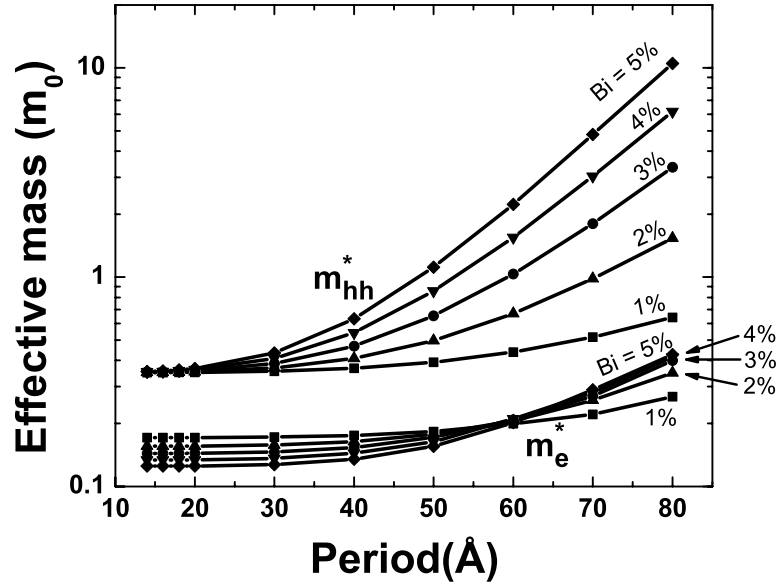


Figure 2.5 Effective masses of ground state minibands (m_e^* for CB1 and m_{hh}^* for HH1) for GaAsBi/GaAsN superlattices with matched layer thickness, varying period thickness and variable alloy composition.

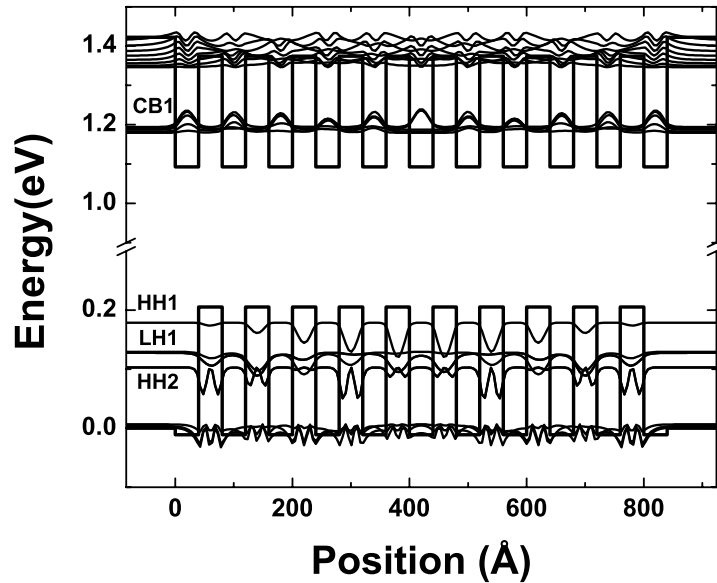


Figure 2.6 Miniband structure for 10 period 40Å/40Å GaAs_{0.96}Bi_{0.04}/GaAs_{0.979}N_{0.02} superlattice using self-consistent Schrödinger-Poisson calculations.

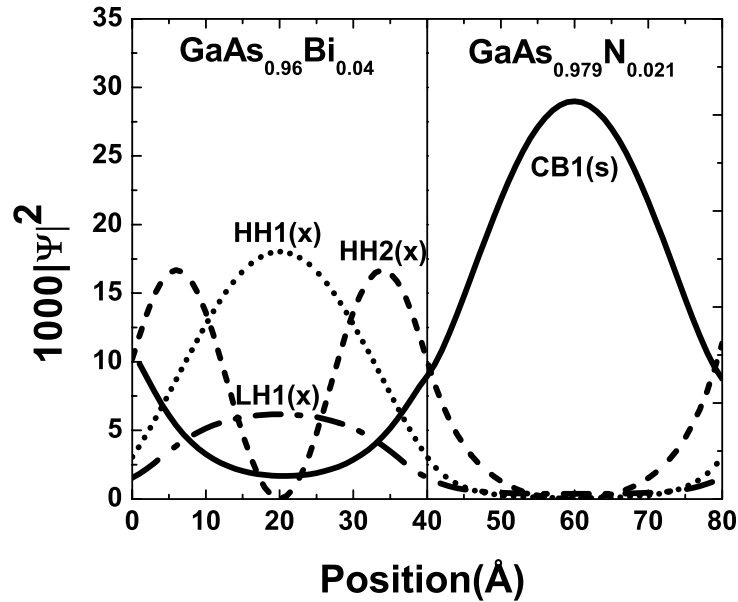


Figure 2.7 Squared envelope function of the 40Å/40Å GaAs_{0.96}Bi_{0.04}/GaAs_{0.979}N_{0.021} superlattice. Characters s and x in the figure represent the symmetry character of the envelop function.

2.3.4. Optical Properties

The joint density of states for the superlattice including the transitions from HH1 to CB1 and LH1 to CB1 is shown in Figure 2.8 for a GaAs_{0.96}Bi_{0.04}/GaAs_{0.979}N_{0.021} superlattice with 80Å period thickness. The curve has a step-like shape due to the quantum confinement in the superlattice, with a smooth transition in the vicinity of the effective bandgap due to the miniband dispersion. The joint density of states for the LH1 to CB1 transition results in a shallower transition due to the large curvature of the LH1 band in the out of plane direction. The optical absorption coefficient of the superlattice for x-polarized light incident in the growth direction is shown in Figure 2.9, assuming a full valence band and empty conduction band. The absorption spectrum follows the step-like shape of the joint density of states, altered by the oscillator strength of the optical

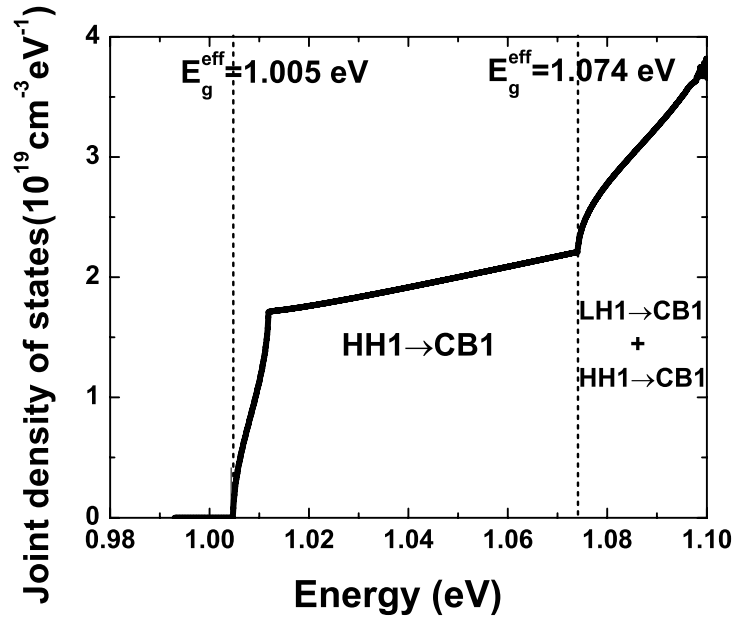


Figure 2.8 Joint density of states of a 40Å/40Å GaAs_{0.96}Bi_{0.04}/GaAs_{0.979}N_{0.02} superlattice.

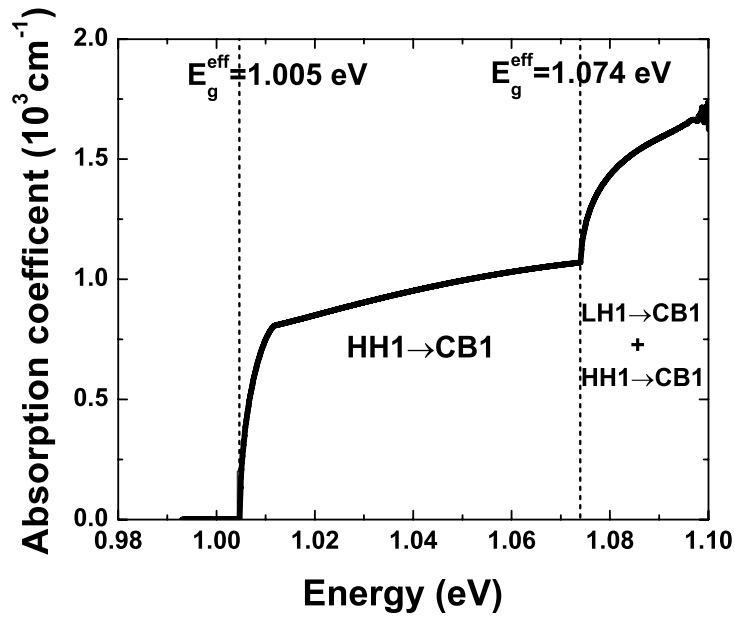


Figure 2.9 Absorption coefficient of a 40Å/40Å GaAs_{0.96}Bi_{0.04}/GaAs_{0.979}N_{0.02} superlattice.

transition in this type-II structure. In these calculations, the Coulomb interaction between electrons and holes was not considered, which would otherwise result in excitonic peaks below the effective bandgap energy. The magnitude of the optical absorption coefficient is approximately one order of magnitude smaller than bulk GaAs due to the spatially indirect transition, with approximately the same magnitude for joint density of states.

2.4. Conclusions

In conclusion, the miniband structure for strain-balanced GaAsBi/GaAsN with effective lattice match to GaAs were calculated, demonstrating a range of effective bandgap of 0.89eV - 1.32eV for Bi,N composition of less than 5% and period thickness of up to 100Å. The energy-momentum dispersion relations show a general trend of increasing carrier effective mass with increasing period due to reduced tunneling probability, and a compositional dependence that contains a crossover point for electron effective mass due to competing mechanisms of the superlattice period and host material properties. The calculated miniband structure by the k.p method is consistent with the Schrodinger-Poisson technique, where further efforts to determine carrier effective mass are required in order to provide improved accuracy and agreement for excited state transitions. The GaAsBi/GaAsN superlattices have a joint density of states similar to GaAs and an optical absorption coefficient that is approximately one order of magnitude lower than GaAs due to the spatial separation of electron and hole wavefunctions in the type-II structure. This superlattice structure may provide a narrow bandgap material system that is lattice-matched to GaAs with optical response suitable for optoelectronic devices requiring optically thick active regions, such as a spectral band in a multi-

junction solar cell. Further theoretical and experimental work is desired to realize these materials and to determine optical transitions and charge transport properties.

CHAPTER 3

Electronic structures of GaSb/GaAs quantum dots

3.1. Introduction

GaSb/GaAs quantum dots (QDs) introduce unique opportunities for the applications of photovoltaic devices [23, 55], infrared light emitting diodes [56], semiconductor lasers [57, 58], and charge storage devices [59, 60] because of the staggered (type-II) band alignment of the heterostructures, where holes are confined within the GaSb QD while electrons are in the surrounding GaAs. In this band configuration, the spatially indirect optical transition of carriers between the QD confined states and the conduction band (CB) of GaAs leads to a long radiative lifetime of carriers on the order of nanoseconds[61], and the overlap between the electron and hole wavefunctions can be controlled by optimizing QD structures or charge injections within the QD states enabling the modulation of the optical transition rate [62]. In addition, the deep potential well on the valence band is favorable for reducing thermal connections between the QD confined states and the valence band (VB). These distinctive intrinsic properties of the type-II GaSb QD can provide better thermal stability, longer carrier storage time [60], suppressed Auger-recombination of non-equilibrium carriers [63], and finer tuning of operating wavelengths in the device applications [64], which are difficult to achieve in the type-I heterostructures such as InAs/GaAs QDs. Specifically, the type-II

GaSb/GaAs QDs can be applied to intermediate band solar cells (IBSCs) to build the intermediate band (IB) with the confined states of the QDs. In this application, the low thermal emission rates of the type-II QDs are beneficial to the quasi-Fermi level separation between the IB and the valence band (VB) of GaAs [17], and the changeable/reduced optical transition rates from the QD states to the CB of GaAs provide an opportunity to closely match them to the rates of the optical transition from the VB to the QD states.

In this work, details of electronic structures and optical properties of the GaSb/GaAs QDs are studied based on the 8-band k.p model, and some of the results are compared with the previously reported experimental results in order to validate the assumptions and theoretical methods used in this study.

3.2. Methods

3.2.1. Quantum dot structures

In the device applications, the GaSb QDs are embedded in the GaAs crystal in order to create confined states of discrete density of states. The structure of the buried QDs has been investigated by cross-sectional scanning tunneling microscopy (XSTM) [65, 66] and atom probe tomography (APT) [67], and various sizes and shapes of the QDs have been reported due to strong intermixing between As and Sb. However, QD peaks in the photoluminescence data do not much differ from each other, with the value of the peak locations being almost 1.1 eV (regardless of the QD structure), suggesting that the physical structure is not the most critical factor affecting the electronic structure of the GaSb/GaAs QDs. Therefore, in this study, the GaSb QDs grown on a GaAs (100) surface are assumed to have the plat dome shape reported in ref [67], with a diameter of 25 nm

and a height of 3.6 nm, shown in Figure 3.1, and a 1ML wetting layer is included as illustrated in Figure 3.2.

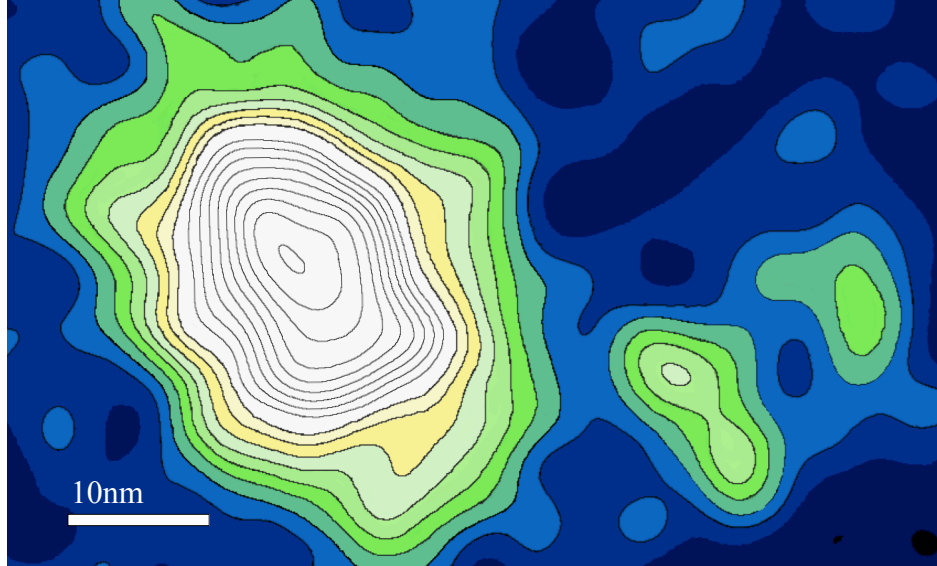


Figure 3.1 Contour plots of varying Sb concentrations composed from atom probe tomography data within the GaSb/GaAs QD layers of the sample, as seen from the (001) surface (adopted from [67])

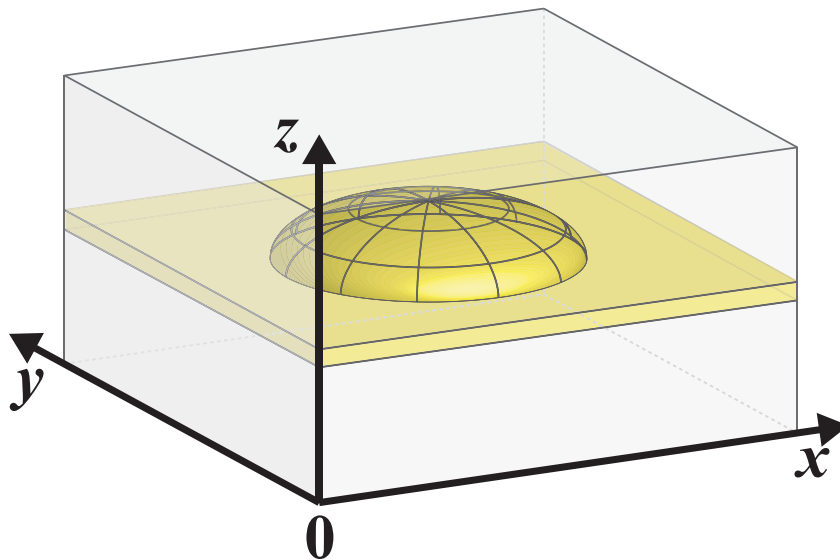


Figure 3.2 Model structure of a GaSb QD with 1ML GaSb wetting layer on (100) surface embedded in GaAs matrix, together with the axes referred to in the text

3.2.2. Strain distribution

Because the lattice constant mismatch between GaSb and GaAs is approximately 7.8%, the band structure of the self-assembled GaSb/GaAs QDs can be significantly affected by the strain. In order to determine the strain tensors of the dome shaped GaSb QDs buried in the GaAs matrix, the Valence Force Field (VFF) strain model of Keating [68] and Martin [69] is employed, which can provide a reasonable description of the elastic properties of III-V materials. In the semi-empirical model, the total elastic energy is given by [69]

$$U = \sum_i U_i = \sum_i \left(\frac{3}{16} \sum_j \alpha_{ij} \frac{(\vec{r}_{ij}^2 - r_{0ij}^2)}{r_{0ij}^2} + \frac{3}{8} \sum_{j \neq k} \beta_{ijk} \frac{\vec{r}_{ij} \cdot \vec{r}_{ik} + (r_{0ij} r_{0ik} / 3)^2}{r_{0ij} r_{0ik}} \right) \quad (3.1)$$

where \vec{r}_{ij} and r_{0ij} represent the distance vector from a certain atom (i) to one of the nearest neighbors (j) and the equilibrium bond length of these atoms ($r_0 = a\sqrt{3}/4$, where a is the lattice constant), respectively. The bond-stretching and bond-bending constants, α_{ij} and β_{ij} , are given in Table 3.1, and β_{ijk} is defined by $\sqrt{\beta_{ij}\beta_{ik}}$ [70]. In this work, only the changes in the bond length and angle with the first nearest neighbors are considered, corresponding to the first and the second summation terms in the equation (3.1), and the effect of long-range Coulombic interaction is ignored. The whole configuration of the atoms in the model structure is defined by iteratively solving the three-coupled differential equations

$$\frac{\partial U}{\partial x_i} = \frac{\partial U}{\partial y_i} = \frac{\partial U}{\partial z_i} = 0 \quad (3.2)$$

for all atomic positions until the total elastic energy U of the system reaches the minimum value [70]. The final displacement (u, v, ω) of the atoms can be directly converted to the strain tensors, ε_{ij} ($i, j = x, y, z$), based on the following relations [71]:

$$\begin{aligned}
2r_0\varepsilon_{xx} &= u'_2 - (u'_2 + u'_3 + u'_4)/2 \\
2r_0\varepsilon_{yy} &= v'_3 - (v'_2 + v'_3 + v'_4)/2 \\
2r_0\varepsilon_{zz} &= \omega'_4 - (\omega'_2 + \omega'_3 + \omega'_4)/2 \\
4r_0\varepsilon_{xy} &= u'_3 - (u'_2 + u'_3 + u'_4)/2 + v'_2 - (v'_2 + v'_3 + v'_4)/2 \\
4r_0\varepsilon_{yz} &= v'_4 - (v'_2 + v'_3 + v'_4)/2 + \omega'_3 - (\omega'_2 + \omega'_3 + \omega'_4)/2 \\
4r_0\varepsilon_{xz} &= u'_4 - (u'_2 + u'_3 + u'_4)/2 + \omega'_2 - (\omega'_2 + \omega'_3 + \omega'_4)/2
\end{aligned} \tag{3.3}$$

where u'_i , v'_i , and ω'_i ($i = 1, 2, 3, 4$, the four nearest neighbors) stand for $u_i - u_0$, $v_i - v_0$, and $\omega_i - \omega_0$, respectively.

Table 3.1 Parameters used in the VFF calculations [69]

	α (N/m)	β (N/m)	a (Å)
GaAs	41.19	8.95	5.6533
GaSb	33.16	7.22	6.0959

3.2.3. Electronic structures

In order to calculate the single carrier states of the self-assembled GaSb/GaAs QDs, the 8-band $\mathbf{k}\cdot\mathbf{p}$ method is applied within the envelope function approximation. In this approximation, the wavefunction, $\Psi(\vec{r})$, can be expanded in the form

$$\Psi(\vec{r}) = \sum_{i=1}^8 \Phi_i(\vec{r})|i\rangle \tag{3.4}$$

where $|i\rangle$ is the Γ point Bloch functions of the conduction, heavy-hole, light-hole, and spin-orbit bands corresponding to Γ_6 , Γ_7 , and Γ_8 of the zinc-blend crystal, and $\Phi_i(\vec{r})$ is

the envelope function of the i -th basis [72, 73]. The wavefunction satisfies the time-independent Schrödinger equation,

$$H(\vec{r})\Psi(\vec{r}) = E\Psi(\vec{r}) \quad (3.5)$$

with the Hamiltonian given by

$$H(\vec{r}) = H_0(\vec{r}) + H_s(\vec{r}) \quad (3.6)$$

where H_0 and H_s are the 8×8 matrices corresponding to the second order eight-band Kane Hamiltonian with the modified Luttinger-like parameters and the strain Hamiltonian, respectively. All \mathbf{k}, \mathbf{p} parameters used in this calculation are given in Table 3.2. The strain Hamiltonian can be constructed by the strain tensor ε_{ij} ($i, j = x, y, z$) from the VFF calculations described in the section 3.2.2 and the deformation potentials listed in Table 3.3.

Table 3.2 Parameters used in the 8-band \mathbf{k}, \mathbf{p} calculation [74-76]

	E_g (eV)	$E_{v,av}$ (eV)	Δ_0 (eV)	γ_1	γ_2	γ_3	E_p (eV)
GaAs	1.5192	-6.92	0.341	-6.95	-2.10	-2.90	22.71
GaSb	0.813	-6.25	0.82	-13.4	-4.70	-6.00	22.88

Table 3.3 Deformation potential parameters used in the 8-band \mathbf{k}, \mathbf{p} calculation [76]

	a_c (eV)	a_v (eV)	b (eV)	d (eV)
GaAs	-7.17	1.16	-1.7	-4.50
GaSb	-6.85	0.79	-2.0	-4.8

According to North *et al.* [77], the conduction band offset of the type-II GaSb/GaAs heterointerface derived from the model-solid theory of van der Walle [76]

$$E_v = E_{v,av} + \frac{\Delta_0}{3} \quad (3.7)$$

(0.63 eV) deviates substantially from the experimental results measured by ballistic electron emission microscopy ($0.08 \pm 0.02\text{eV}$) [78]. In order to be consistent with the experimental results, the Kane Hamiltonian in the equation (3.5) is modified by shifting down the conduction, heavy-hole, light-hole and spin-orbit bands of GaSb by 0.53 eV from their original positions defined by the model-solid theory, replicating the method used by North *et al.* [77]. To solve the eigenvalues and eigenfunctions of the secular equation of the 8-band k.p Schrödinger equation, the finite-difference method is employed on the 3-dimensional uniform square mesh, the spacing of which is the lattice constant of GaAs, 5.6533 Å, in all directions.

In addition, the fully occupied QD states are calculated by considering the Coulomb charging energy as perturbations to the single particle structure. The matrix element of the Coulomb interaction is

$$\Delta E_{ij}^c = -\frac{e^2}{4\pi\epsilon_0} \iint \frac{|\Psi_i(\vec{r}_1)|^2 |\Psi_j(\vec{r}_2)|^2}{\epsilon_r(\vec{r}_1, \vec{r}_2) |\vec{r}_1 - \vec{r}_2|} d\vec{r}_1 d\vec{r}_2 \quad (3.8)$$

where $\Psi_i(\vec{r})$ is the normalized wavefunction of the i -th confined state in the GaSb QD with a single particle [79-81]. In this approximation, only the repulsive Coulomb force between the holes in the QD states is considered, while the attractive Coulomb force between the holes in the QD states and the electrons on the CB of the surrounding GaAs is ignored because the spatial distance between the electrons and the confined holes is distinctly greater than the distance between the holes in the QD states [64]. Also, the quantum confinement effect of the triangle potential on the CB established at the interface between GaAs and GaSb under the high carrier injection condition, which

causes blueshift of the photoluminescence (PL) peak from the type-II QDs with increasing excitation density [61, 64], is not considered.

3.2.4. Optical transition

In this work, the optical capture cross sections of the transitions from the QD ground state to the GaAs CB and from the GaAs VB to the QD ground state are calculated based on the relation [82]

$$\sigma_{i \rightarrow f}^{op}(\omega) = \frac{2\pi}{\tilde{n}\epsilon_0 c \omega} |\langle i | H' | f \rangle|^2 g(E_f - E_i - \hbar\omega) \quad (3.9)$$

where

$$H' = \frac{ie\hbar}{m_0} \vec{A} \cdot \nabla \quad (3.10)$$

and the inhomogeneous broadening of the QD states is accounted in terms of the Gaussian function

$$g(E_i - E_f - \hbar\omega) = \frac{1}{\sigma\sqrt{2\pi}} \exp\left(-\frac{(E_i - E_f - \hbar\omega)^2}{2\sigma^2}\right) \quad (3.11)$$

The linewidth of the transition, σ , is assumed to be 20meV [83]. The wavefunction of the QD ground state needed to calculate the matrix element, $\langle i | H' | f \rangle$, is obtained from the 8-band $\mathbf{k}\cdot\mathbf{p}$ calculation. However, for the sake of reducing calculation power, the wavefunctions of the CB and VB of the surrounding GaAs matrix where the influence of the remote bands are insignificant are calculated by the single-band Schrödinger equation in the effective mass approximation

$$-\frac{\hbar^2}{2} \left(\nabla \cdot \left(\frac{1}{m_{eff}(\vec{r})} \nabla \Psi(\vec{r}) \right) \right) + V(\vec{r}) \Psi(\vec{r}) = E \Psi(\vec{r}) \quad (3.12)$$

where $m_{eff}(\vec{r})$ is the density of states effective mass of electrons (holes), and $V(\vec{r})$ corresponds to the CB (VB) profile obtained from the 8-band $\mathbf{k}\cdot\mathbf{p}$ calculation.

The differential equation is solved numerically by applying the finite-element method on the 3-dimensional uniform square mesh, the spacing of which is the lattice constant of GaAs, 5.6533 Å, in all directions. The periodic boundary condition is assumed in the x, y, and z directions.

3.3. Results

3.3.1. Electronic structure

The strain distributions in the QDs calculated from the VFF strain model are shown in Figure 3.3, Figure 3.4, and Figure 3.5. According to the diagonal components of the strain tensors (ϵ_{xx} and ϵ_{zz}) shown in Figure 3.3, the tensile strain permeates deep into the GaAs layer in the [001] direction, suggesting that the GaAs spacer requires some degree of thickness in order to avoid the strain accumulation in a stack of multiple QD layers, which is usually incorporated in the device application. The hydrostatic and the biaxial strains can be expressed in terms of the diagonal components of the strain tensors,

$\epsilon_{xx} + \epsilon_{yy} + \epsilon_{zz}$ and $\epsilon_{zz} - \frac{1}{2}(\epsilon_{xx} + \epsilon_{yy})$, respectively, and these directly affect the profile of

the electron, heavy-hole, and light-hole potentials in the GaSb/GaAs QDs. The negative hydrostatic strain inside the QD shifts the conduction band (CB) and the valence band (VB) of GaSb upward and downward, respectively, resulting in the larger bandgap than the bandgap of bulk GaSb (0.75 eV). In addition, the positive biaxial strain inside the QD splits the heavy-hole and the light-hole band. Shown in Figure 3.6, the light-hole band of GaSb is pushed down while the heavy-hole band moves upward.

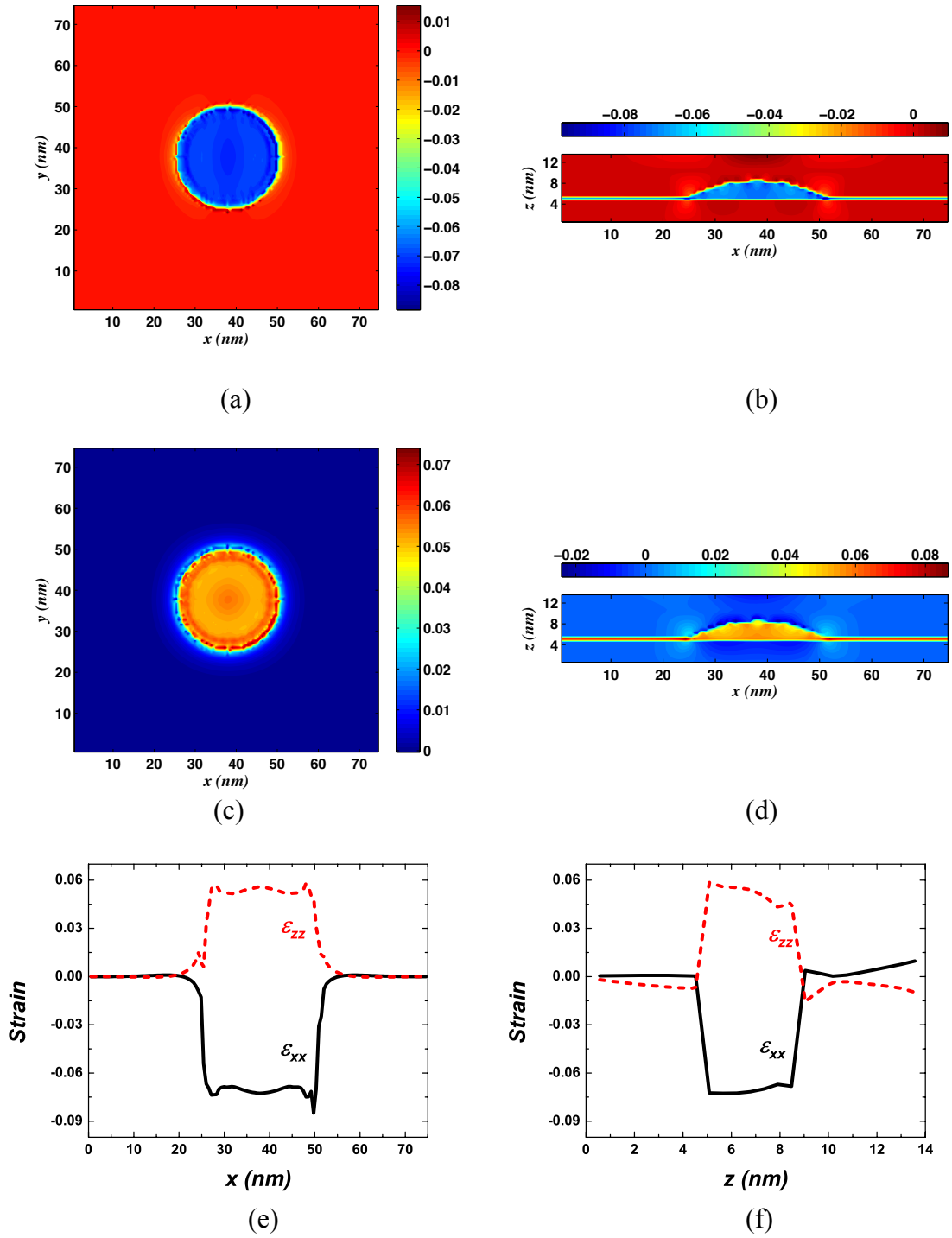


Figure 3.3 The strain distribution of the GaSb QD embedded in the GaAs matrix, calculated using the VFF strain model: (a) ϵ_{xx} at the xy-plane (0.5nm above the base of the QD), (b) ϵ_{xx} at the xz-plane (crossing the center of the dot), (c) ϵ_{zz} at the xy-plane (0.5nm above the base of the QD), (d) ϵ_{zz} at the xz-plane (crossing the center of the dot), and ϵ_{xx} and ϵ_{zz} along (e) [100] direction (0.5nm above the base of the dot) and (f) [001] direction through the center of the dot

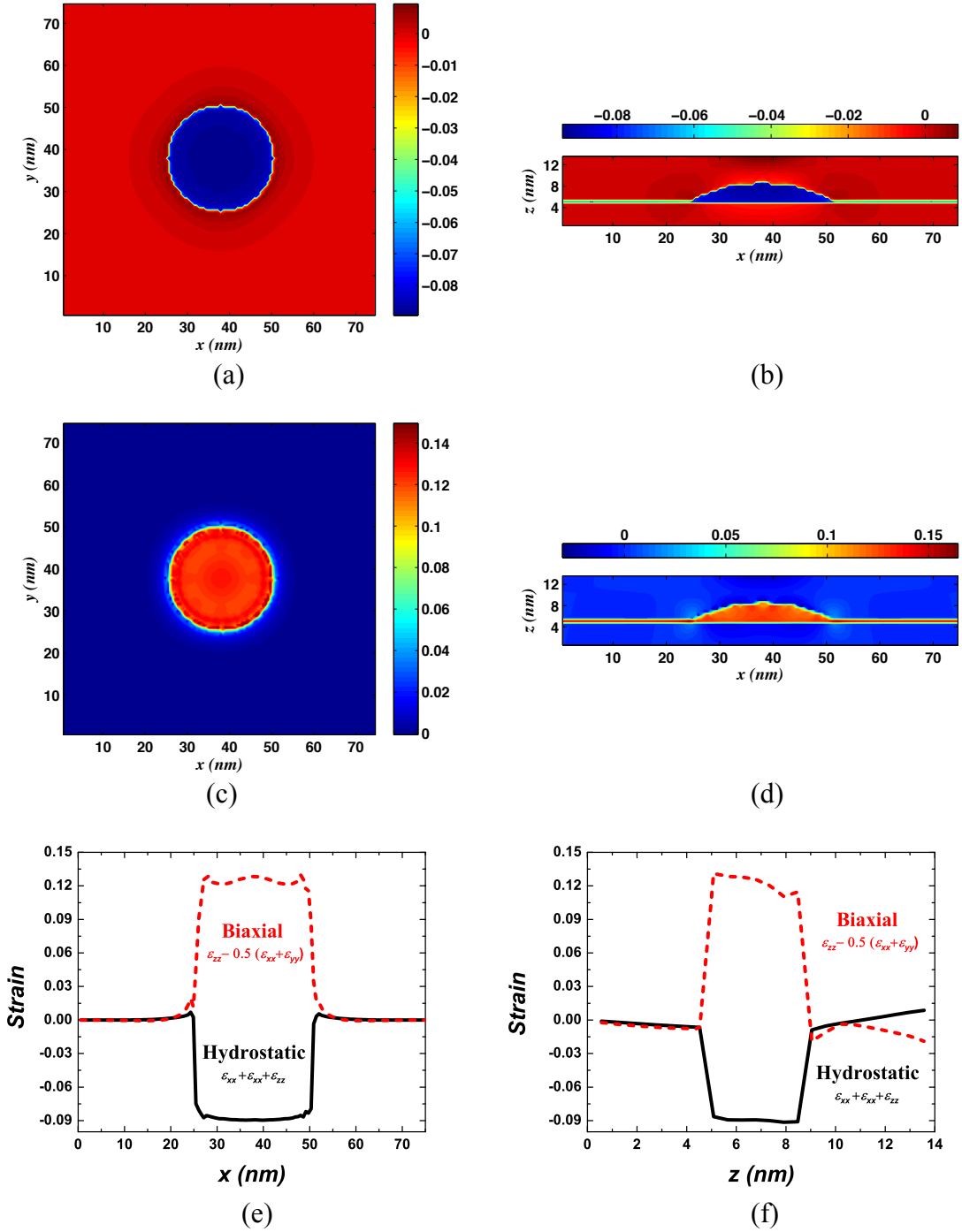
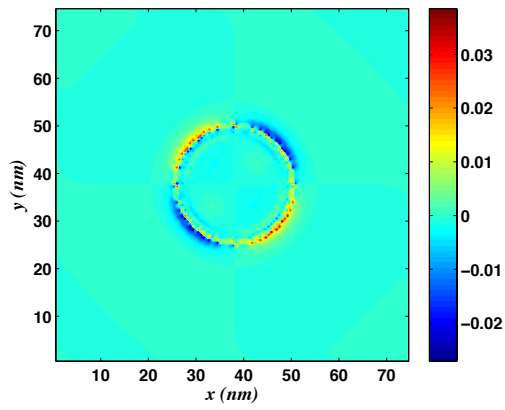
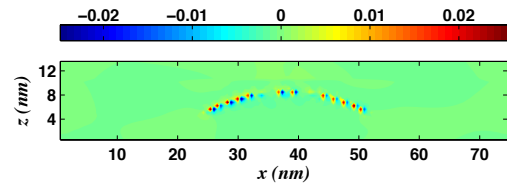


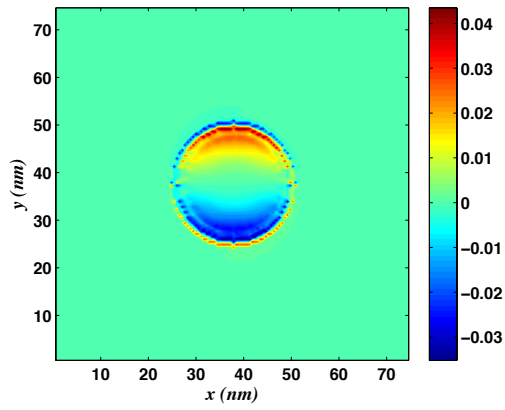
Figure 3.4 The strain distribution of the GaSb QD embedded in the GaAs matrix, calculated using the VFF strain model: Hydrostatic strain (a) at the xy-plane (0.5nm above the base of the QD) and (b) at the xz-plane (crossing the center of the dot), biaxial strain (c) at the xy-plane (0.5nm above the base of the QD) and at the xz-plane (crossing the center of the dot), and the hydrostatic and biaxial strain plotted along (e) [100] direction (0.5nm above the base of the dot) and (f) [001] direction through the center of the dot



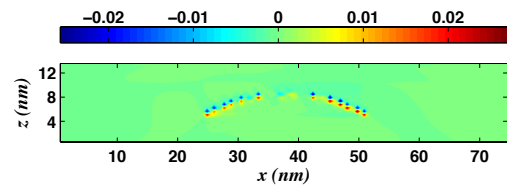
(a)



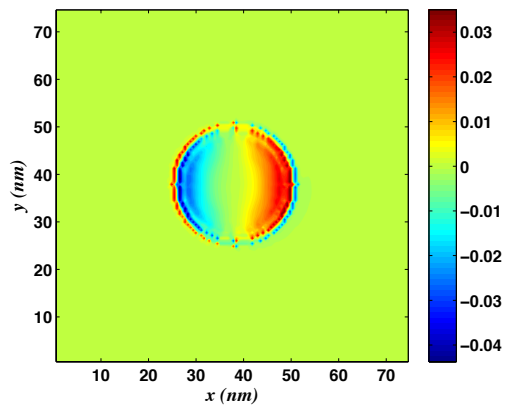
(b)



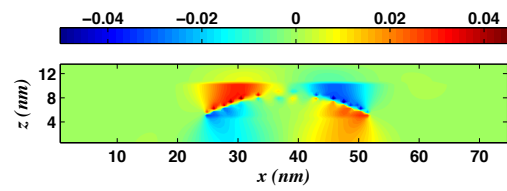
(c)



(d)



(e)



(f)

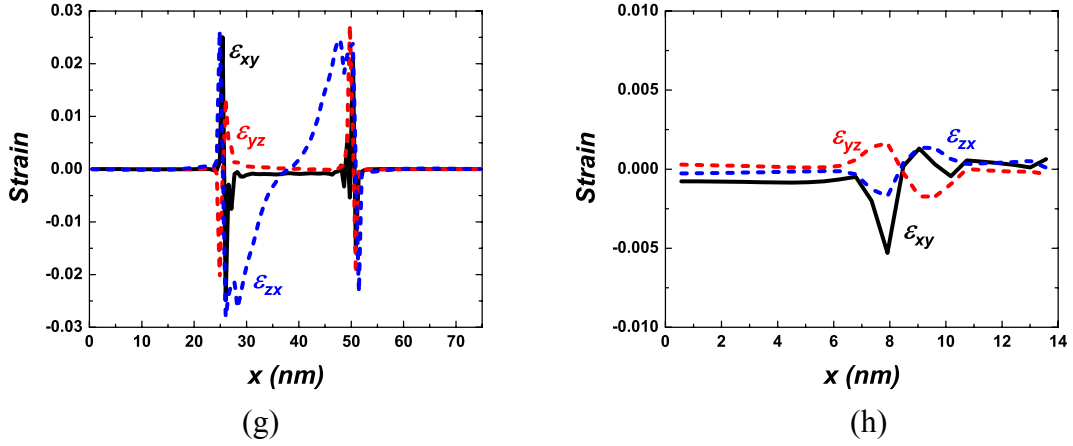


Figure 3.5 The strain distribution of the GaSb QD embedded in the GaAs matrix, calculated using the VFF strain model (shear strain): ϵ_{xy} (a) at the xy-plane (0.5nm above the base of the QD) and (b) at the xz-plane (crossing the center of the dot), ϵ_{yz} (c) at the xy-plane (0.5nm from the base of the QD) and at the xz-plane (crossing the center of the dot), ϵ_{zx} (c) at the xy-plane (0.5nm from the base of the QD) and at the xz-plane (crossing the center of the dot), and the shear strain tensors plotted along (e) [100] direction (0.5nm above the base of the dot) and (f) [001] direction through the center of the dot

The off-diagonal components of the strain tensors ϵ_{xx} , ϵ_{yz} , and ϵ_{zx} , shown in Figure 3.5, can induce piezoelectric polarization, P^{pz} , in the GaSb/GaAs QD structure given by

$$P_i^{pz} = e_{14} \epsilon_{jk}, \quad (j \neq k) \quad (3.13)$$

where e_{14} is the one existent piezoelectric coefficient for zinc-blende structures. According to Figure 3.5, the shear strain is only noticeable at the QD surface and is negligible inside the dot and surrounding GaAs compared to the diagonal components of the strain tensors. Therefore, in this work, the impact of the piezoelectric field on the electronic structure of the QD is ignored.

Figure 3.6 shows the electron, heavy-hole, and light-hole potential profiles along [100] direction after considering the band alteration caused by the strain. The confined energy

states in the QD obtained from the 8-band $\mathbf{k}\cdot\mathbf{p}$ model are also imposed in the band diagram. The results show that the spacing between the confined hole states of the GaSb QD is much closer than the spacing between the electron states in the InAs/GaAs QD system because of the larger effective mass of a hole than that of an electron. The two major optical transitions that can occur in the GaSb/GaAs QD system (from the GaAs CB to the QD ground state, and the band-to-band transition in the GaAs barrier) and the corresponding transition energy values are indicated in the plot. The transition energy values agree well with the location of the peaks in the measured photoluminescence spectra shown in Figure 3.7. The contour plots of squared wavefunctions, $|\Psi|^2$, of the first eight energy levels in the QD at the xy-plane 0.5 nm above the base of the QD are shown in Figure 3.8, and the corresponding energy spectra of the wavefunctions are indicated in the plots.

Finally, the energy spectra of the fully occupied GaSb/GaAs QD system are shown in Figure 3.9. After incorporating the Coulomb charging effect, the number of confined states in the QD reduces to 8 levels, implying that 16 holes can fill a GaSb/GaAs QD completely. This result is in accordance with the results of Geller *et al.*, who derived that a GaSb/GaAs QD (with an average QD base width of about 26 nm, and an average height of about 3.5 nm, and an areal density of about $3 \times 10^{10} \text{ cm}^{-2}$) can be filled completely with 15 holes from the capacitance-voltage measurement [84].

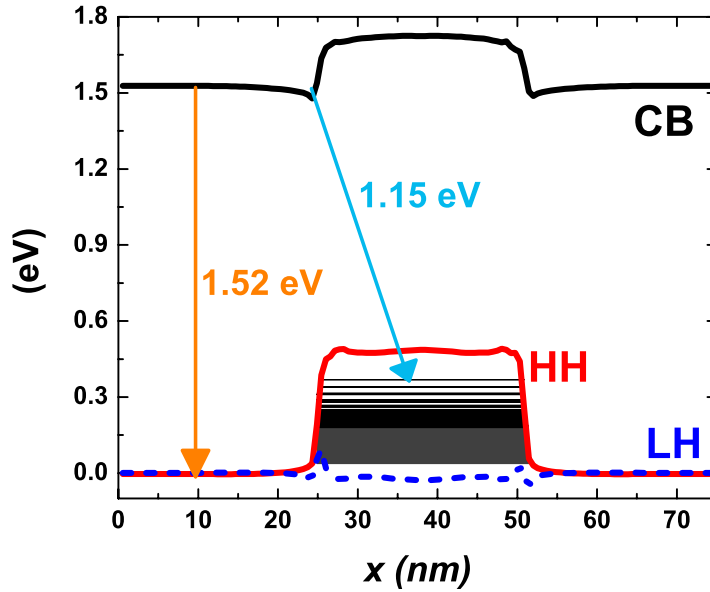


Figure 3.6 The electron, heavy-hole, and light-hole potential profile along [100] direction through the center of QD (0.5nm above the base of QD) imposed by the hole states calculated by the 8-band $\mathbf{k}\cdot\mathbf{p}$ model. (The hole states in the grey area near LH band are too close to show their spacing clearly.)

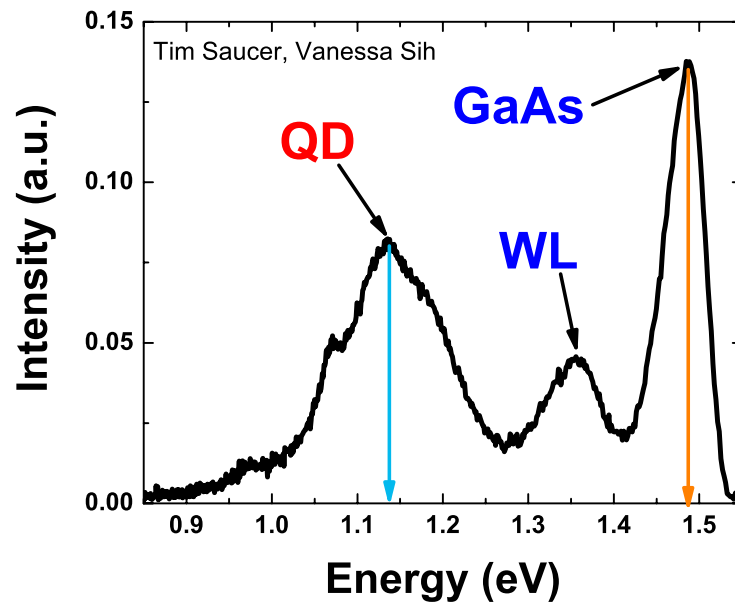


Figure 3.7 Photoluminescence spectra of the GaSb/GaAs QDs (from Tim Saucer and Vanessa Sih, Physics, University of Michigan)

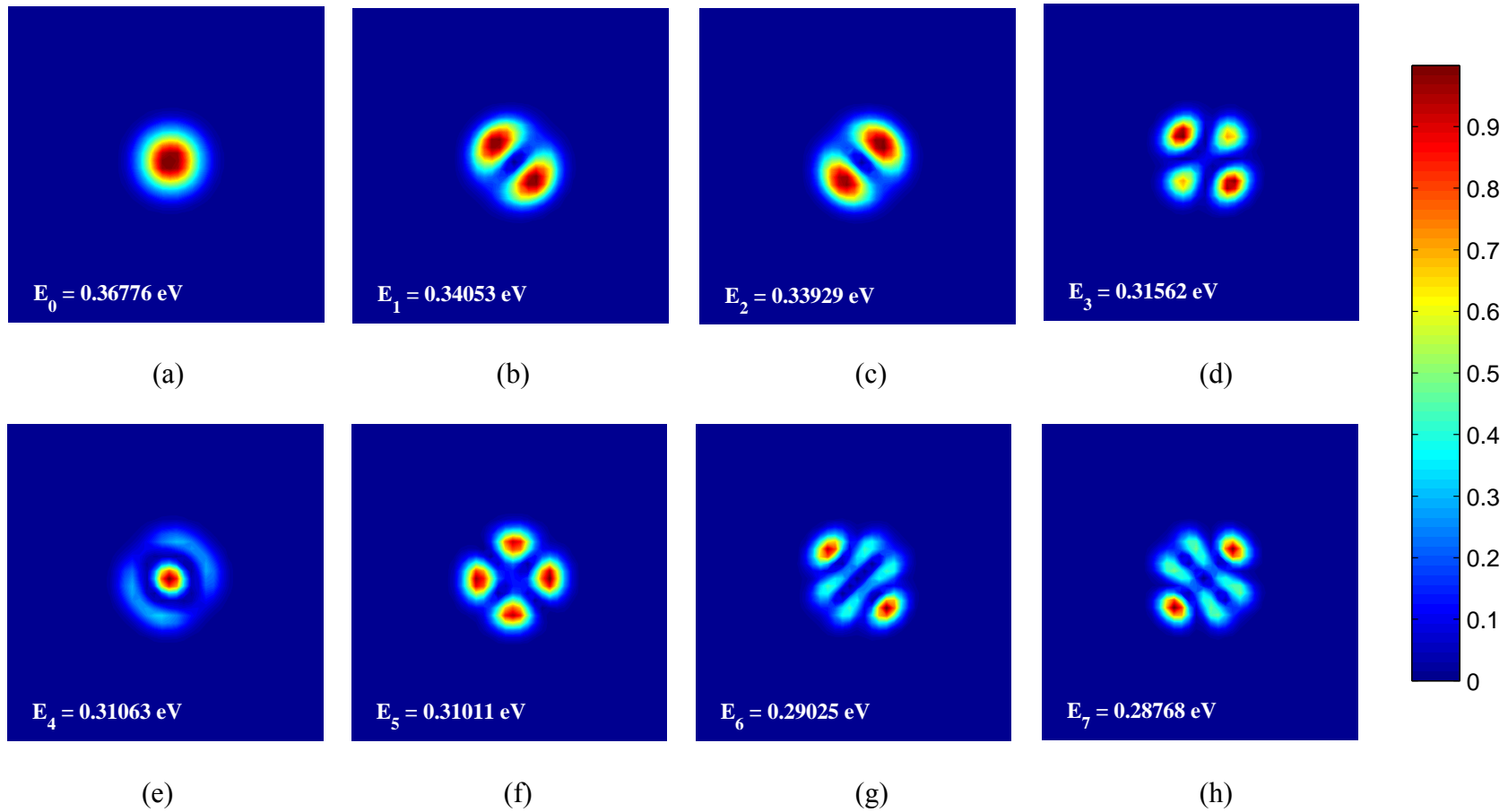


Figure 3.8 Contour plots of squared wavefunctions, $|\Psi|^2$, of the first eight energy levels in the GaSb/GaAs QD at the xy-plane 0.5nm above the base of the QD. The energy level of each wavefunction is indicated in the corresponding plot.

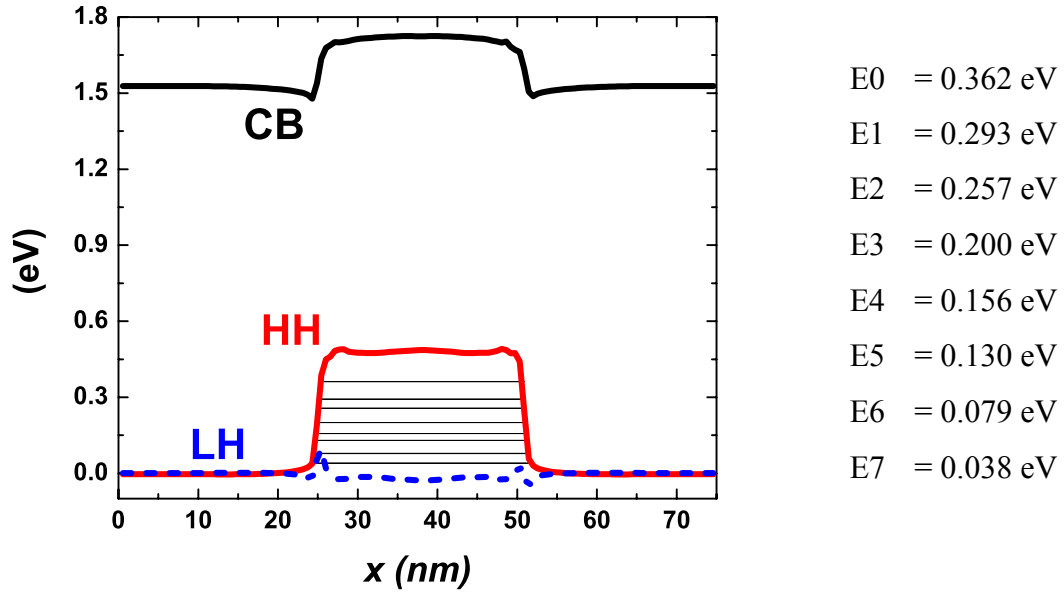


Figure 3.9 Hole states and the energy spectra in the GaSb QD when the dot is fully occupied by holes

3.4. Conclusions

In conclusion, the electronic structures of the self-assembled GaSb QDs embedded in the GaAs matrix are calculated based on the VFF and the 8-band $\mathbf{k}\cdot\mathbf{p}$ model. The strain distributions in the QD derived by the VFF model show that the negative hydrostatic strain in the QD alters the position of the electron, heavy-hole, and light-hole potential profile, resulting in the larger bandgap of the QD than that of bulk GaSb, and the positive biaxial strain splits the HH and LH band significantly. The confined hole states of the QD in the single-particle condition are calculated based on the 8-band $\mathbf{k}\cdot\mathbf{p}$ model with the strain Hamiltonian directly constructed by the strain tensor from the VFF calculation, showing that there is substantially closer spacing between the states because of the large effective mass of holes. The transition energy from the CB edge of the GaAs barrier to the ground state of the QD agrees well with the location of the QD peak in the

PL spectra. In addition, the fully occupied QD states are calculated by considering the repulsive Coulomb energy between the confined holes in the QD as a perturbation, and the results show that 16 holes can fill a QD completely, which closely matches the results from the capacitance-voltage measurement.

CHAPTER 4

Thermal emission in type-II GaSb/GaAs quantum dots and prospects for intermediate band solar energy conversion

4.1. Introduction

Large confinement potential and the spatial separation of electron and hole wavefunctions in type-II heterostructures lend themselves to unique applications in electronic and optoelectronic devices. Among these devices is the intermediate band solar cell (IBSC), where confined states in quantum structures may enhance absorption via multi-photon transitions below the bandgap energy, while maintaining a voltage that tracks the bandgap energy of the host material [85]. The IBSC has been demonstrated in quantum dot (QD) systems including InAs/(Al,Ga)As [86] and (In,Ga)As/Ga(As,P) [87, 88]. While QD IBSCs have demonstrated sub-bandgap response and enhanced photo current, the conversion efficiency of these devices has not exceeded that of GaAs single junction solar cells due to a mismatch in optical transition rates between confined hole levels and electron levels within QDs ($\sim 10^9 \text{ sec}^{-1}$) and transitions from QD confined electron levels to the continuum band of the host material ($\sim 10^3 \text{ sec}^{-1}$) [89]. Increased carrier lifetime has been observed in type-II QDs [90-92] and may provide a better match for optical transitions via the intermediate band, thereby improving photocurrent generation in IBSC devices (analogous to current matching requirements in multi-

junction cells). An intermediate band based on a type-II system has been demonstrated using GaSb/GaAs QDs [93, 94], where enhanced photocurrent is observed, but efficiency is still limited by a significant drop in the V_{OC} . A possible source of reduced V_{OC} for an IBSC is coupling between the intermediate states and the conduction/valence band by thermal capture/emission processes [87, 95, 96]. Thermal emission behavior in QD materials with type-II band lineups such as GaSb/GaAs have competing mechanisms 1) large confinement potential that may enhance energy quantization and suppress thermal emission, and 2) large effective mass in the valence band that may reduce energy quantization and enhance thermal emission. These competing mechanisms motivate a detailed study of thermal emission rates to determine dominant behavior.

Previously, thermal emission in GaSb/GaAs quantum dots have been reported using deep level transient spectroscopy (DLTS) for materials grown by molecular beam epitaxy (MBE) [97] and metal-organic chemical vapor deposition [98], with activation energies in the range of $E_A = 150 - 450$ meV and thermal capture cross section in the range of $\sigma_{th} = 10^{-16} - 10^{-12}$ cm². Similar results have been reported for GaSb/GaAs QDs using admittance spectroscopy [60]. The results reported for thermal emission characteristics in GaSb/GaAs QDs are somewhat variable, where the source of the differences (e.g. growth technique, QD dimensions) and detailed study of the bias-dependence remains unclear. In this paper, the carrier population dependence of thermal hole emission in GaSb/GaAs QDs grown by MBE are described, where the implications of the observed behavior on the operation of an IBSC are analyzed.

4.2. Methods

Three Schottky diode structures were used for this study, consisting of structures grown by MBE on p⁺ GaAs(001) substrates. The three structures are (1) a GaAs control, (2) 1.0 monolayer (ML) GaSb quantum well (QW), and (3) a single layer of GaSb QDs with a nominal thickness of 2.3 ML. The material structures include an initial p-GaAs layer with thickness of 600 nm. The GaSb QDs were grown via the Stranski-Krastanov growth mode, where details of the growth and resulting structural properties are reported elsewhere [99]. Samples were subsequently capped with 200 nm of p-doped GaAs. The control GaAs sample consisted of 800 nm of p-doped GaAs grown at a rate of 1.0MLsec⁻¹. Ti/Au Schottky contacts of diameter 240 μm were deposited, and Pd/Zn/Pd/Au ohmic contacts were deposited on the backside of the substrate. AC capacitance and conductance measurements were performed using a Keithley 4200-SCS Semiconductor characterization system with 30 mV RMS over a temperature range of T = 20 K – 300K and frequency range of 100 kHz – 1 MHz.

4.3. Results

The Capacitance-Voltage (C-V) characteristics of the three Schottky diode samples measured at 300 K and f = 1 MHz are shown in Figure 4.1 (a). The control sample exhibits a conventional V^{-1/2} dependence. A plateau region is observed for the QW and QD samples between approximately 1 – 3 V reverse bias, consistent with charge accumulation in the quantum confined layers [100, 101]. The hole accumulation at the QD and QW layer can be shown clearly by calculating the depth-dependent majority carrier distribution [102]

$$p(W) = \frac{2}{q\epsilon_s\epsilon_0 A^2 d(1/C^2) / dV} \quad (4.1)$$

where $W = \epsilon_s\epsilon_0 A/C$, with results shown in Figure 4.1 (b). The control GaAs sample exhibits a constant hole concentration of $p = 1.37 \times 10^{17} \text{ cm}^{-3}$, consistent with the intended value of $1 \times 10^{17} \text{ cm}^{-3}$. The QW and QD exhibit peaks corresponding to the QD and QW locations occurring at approximately $0.17 \text{ }\mu\text{m}$ from the top metal/semiconductor interface. The number of holes in the QD structure can be estimated from the C-V characteristics according to the relation [101], $Q \approx C_p \Delta V / N_{QD}$, where C_p and ΔV define capacitance value and voltage range of the plateau region, respectively, and N_{QD} represents the areal density of the QD layer. The QD areal density is approximately $3.5 \times 10^{10} \text{ cm}^{-2}$ based on atomic force microscopy studies on independent samples grown under similar conditions, resulting in 39 holes per QD.

Representative data of conductance versus temperature for the three structures are compared in Figure 4.2 (a). The QD structure demonstrates a unique conductance peak that is not observed in the QW and GaAs control samples. This observation provides unambiguous identification of conductance behavior associated with GaSb QD states, distinct from a 2-D GaSb wetting layer or defect states in GaAs. The bias-dependence of conductance versus temperature is shown in Figure 4.2 (b), which exhibits a peak shift to higher temperature under increasing reverse bias. The shift of the conductance peak to higher temperature with increasing reverse bias suggests the presence of Coulomb charging effects [103] or state-filling in the QDs [104], behavior that provides further support that the observed conductance behavior is related to thermal emission and capture processes via QD states. The distinct plateau region in the C-V curve and conductance peak and its characteristics observed in this work, which do not appear in control GaAs

and QW samples, demonstrate a more obvious response from GaSb/GaAs QD states in comparison to prior reports [60, 97], providing high confidence in the data and ability to attribute measured data to QD response without ambiguity. Following the identification of the signal from the QD states, the remainder of the article will exclusively discuss results and analysis of the QD structure.

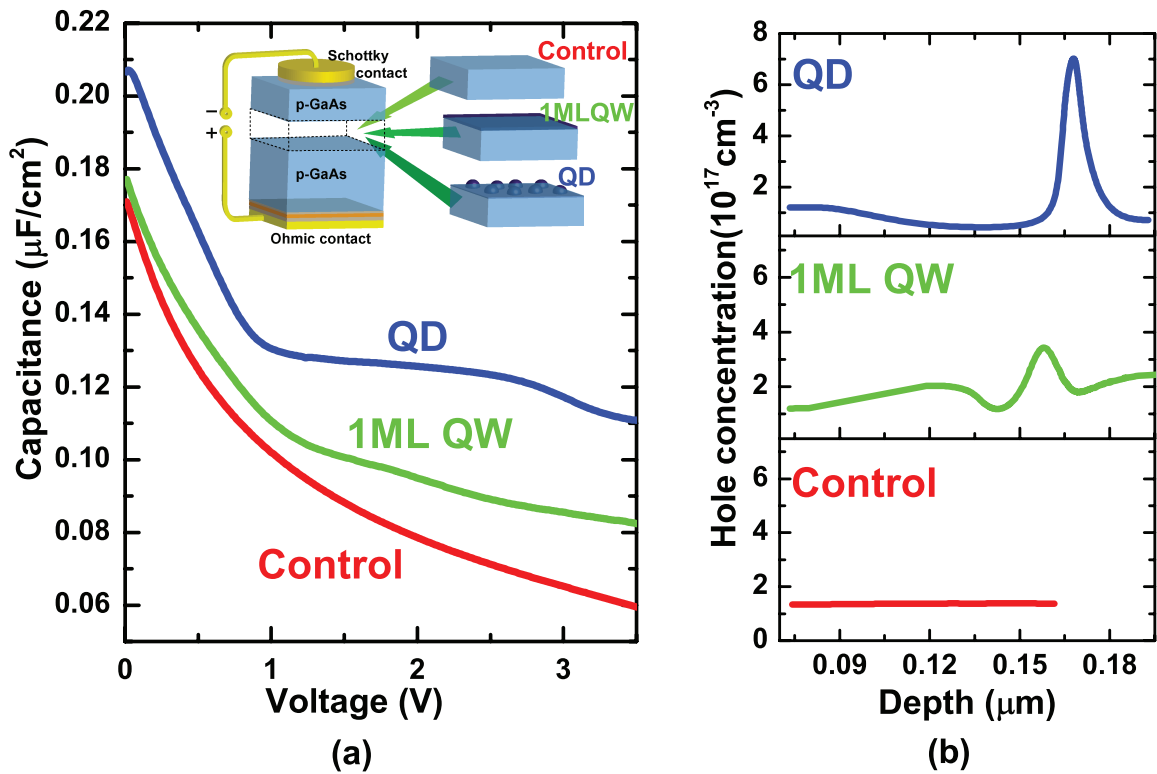
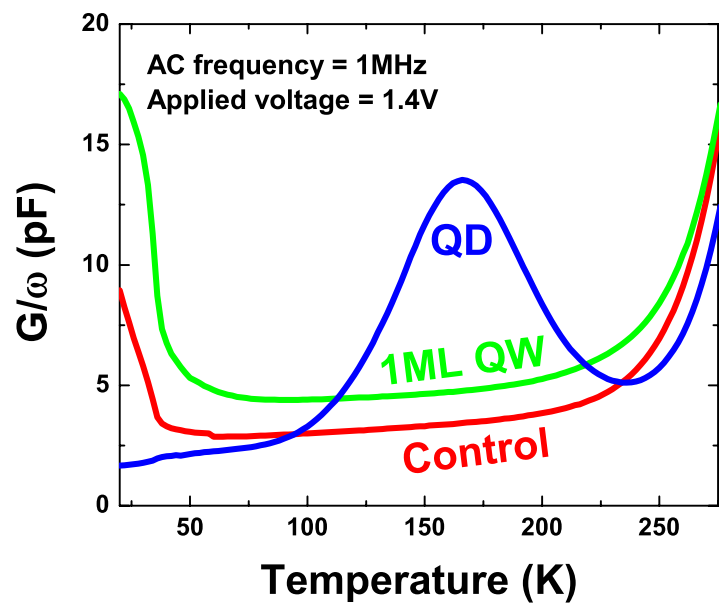
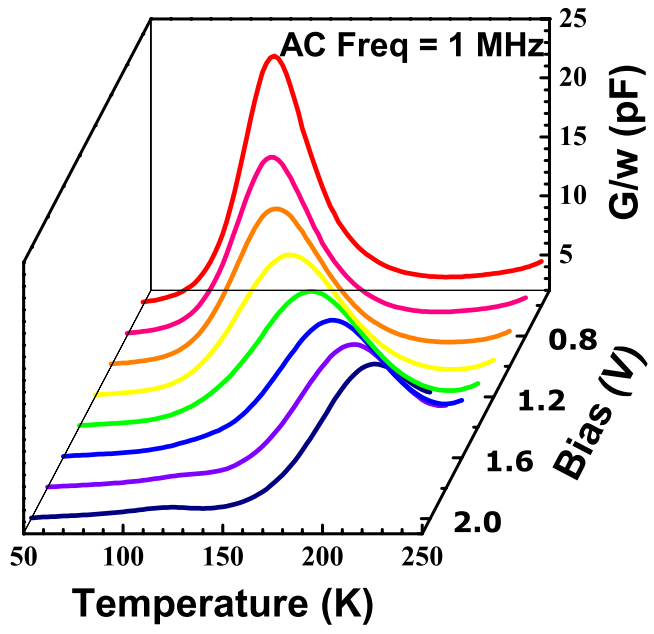


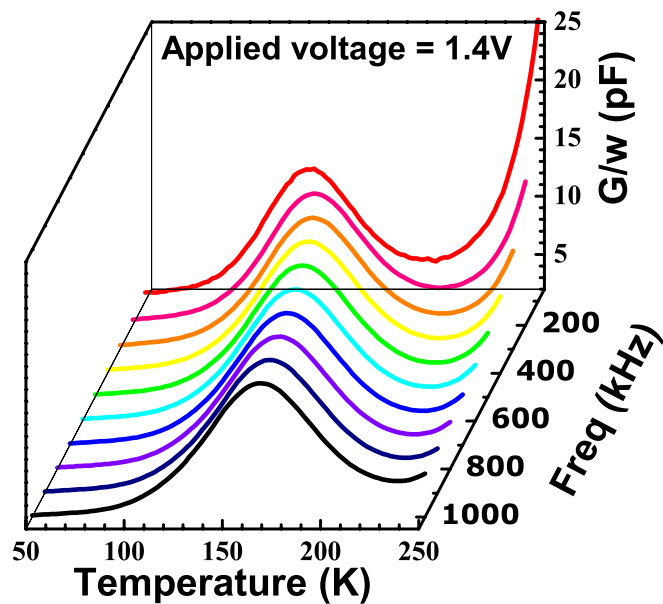
Figure 4.1 (a) Capacitance-Voltage characteristics measured at 300K under AC bias at $f = 1$ MHz (data is offset vertically by $0.03 \mu\text{F}/\text{cm}^2$ for clarity), and (b) majority carrier distribution of the Schottky diode samples.



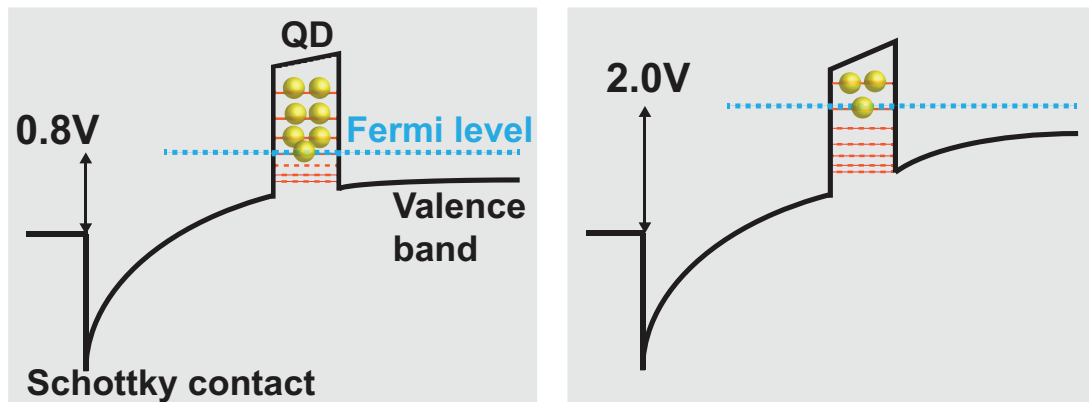
(a)



(b)



(c)



(d)

Figure 4.2 (a) Temperature-dependent conductance of QD, QW, and GaAs control samples measured at $V = 1.4$ V and $f = 1$ MHz, (b) temperature-dependent conductance of the QD sample at $f = 1$ MHz and varying bias, (c) temperature-dependent conductance of the QD sample at $V = 1.4$ V and varying frequency, and (d) band diagram under reverse bias at 0.8V (left) and at 2.0V (right)

The maximum value of the conductance versus temperature occurs when the thermal emission rate for holes satisfies the condition [105]

$$e_n = \sigma_{th} \gamma T^2 \exp\left(-\frac{E_A}{k_B T}\right) = \frac{\omega}{2} \quad (4.2)$$

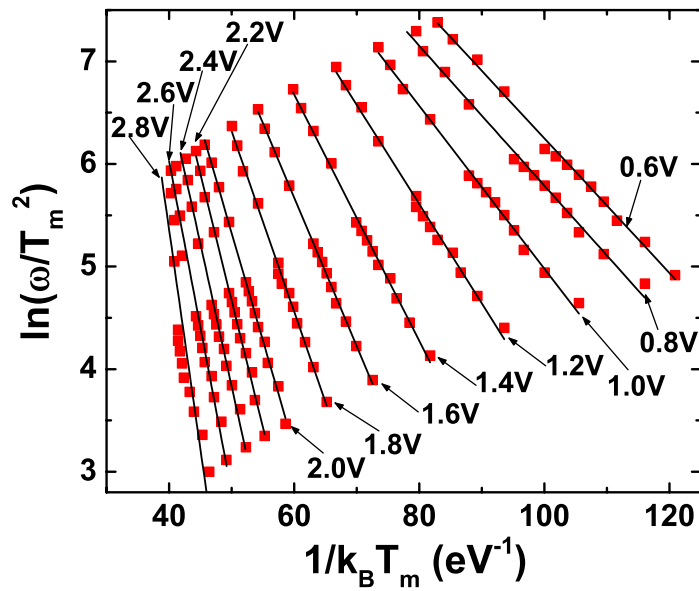
where σ_{th} , E_A , γ and ω represent thermal capture cross section, hole activation energy of a QD, a temperature-independent factor and the frequency of the AC bias, respectively. The activation energy and thermal capture cross section may be determined for a given bias by the Arrhenius relation [105]

$$\ln\left(\frac{\omega}{T_m^2}\right) = -\frac{E_A}{k_B T_m} + \ln(\gamma \sigma_{th}) \quad (4.3)$$

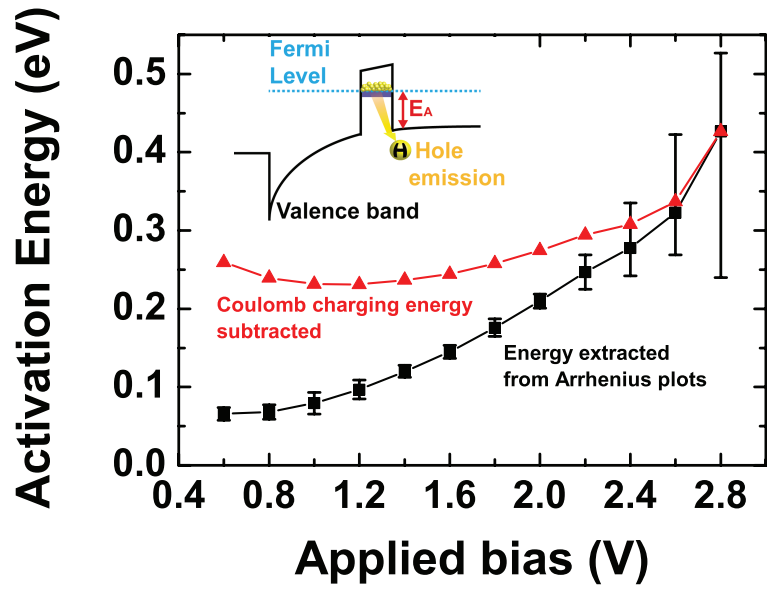
where T_m and γ represent peak temperature of the conductance curve and temperature independent constant, respectively. The resulting data under varying bias are shown in Figure 4.3 (a). Extracted values of the bias-dependent activation energy are shown in Figure 4.3 (b). The analysis presented here assumes a singular energy level within the QD states. A more realistic model would include variability in confined QD energies associated with the inhomogeneous distribution of QD size, and also account for all confined states within the QDs. Analysis using the model presented in this work, however, will provide an accurate description of the average behavior of thermal emission and capture among all confined states in the ensemble of QDs.

The activation energy extracted for the QDs increases with reverse bias, indicating a possible decrease in Coulomb charging energy in the QDs as holes are depleted with increasing reverse bias. The Coulomb charging energy of n holes in a disk shaped QD is given by $E_N = (n - 1/2)e^2/4\epsilon_r\epsilon_0 D$ [103], where D represents the QD diameter, estimated to be approximately 40 nm from independent cross-sectional

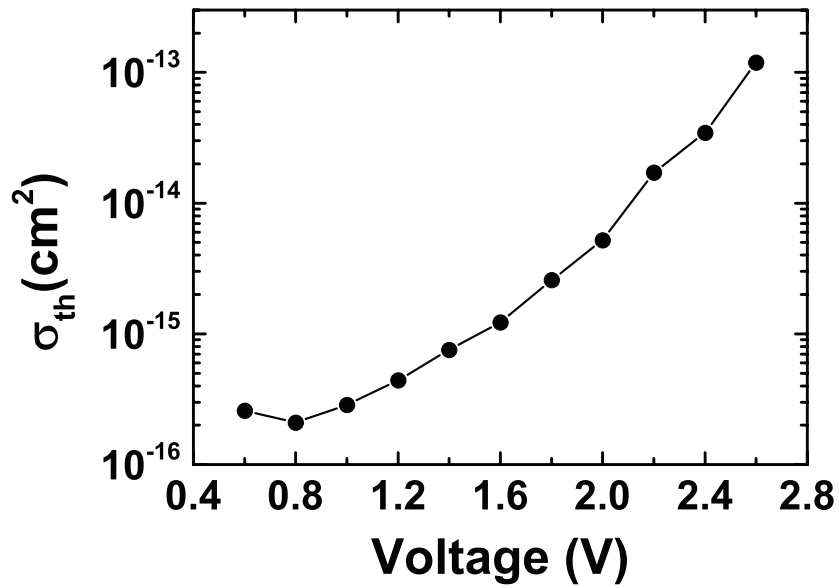
transmission electron microscopy analysis. The Coulomb charging energy can be estimated by C-V analysis. The activation energy obtained by subtracting the calculated Coulomb charging energy is also shown in Figure 4.3 (b), where a range of $E_A = 0.231\text{eV} - 0.337\text{ eV}$ is obtained. This energy corresponds to the separation between confined QD states and the top of the GaAs valence band. The extracted activation energy is also consistent with photoluminescence results, where an energy separation of 0.34 eV is observed [99] between the GaAs bandedge emission and the type-II optical transition from the GaAs conduction band to confined GaSb QD states.



(a)



(b)



(c)

Figure 4.3 (a) Arrhenius plots constructed from peak conductance to extract activation energy and thermal capture cross section, and (b) activation energy and (c) thermal capture cross section extracted from Arrhenius plots and obtained by subtracting Coulomb charging energy.

4.4. Discussions

The thermal capture cross section of the QDs was extracted to be $\sigma_{th} = 2.0 \times 10^{-16} \text{ cm}^2 - 1.2 \times 10^{-13} \text{ cm}^2$ for the bias range between 0.8 V and 2.6 V. The increasing thermal capture cross section of the QDs with increasing reverse bias may be due to reduced Coulomb charging effects or reduced state filling in the QDs. Thermal capture cross section of holes in GaSb/GaAs QDs are orders of magnitude smaller than the reported thermal capture cross section of electrons in InAs/GaAs QDs [106-108], which have been reported in the range from 10^{-10} cm^2 to $3 \times 10^{-12} \text{ cm}^2$. The thermal emission rate of holes from QD states to the GaAs valence band may be compared to the optical generation rate; a comparison of primary importance for an IBSC. The thermal emission rate measured in these experiments is $2.851 \times 10^7 \text{ sec}^{-1}$ at 300 K. The thermal emission rate in the GaSb/GaAs QDs is significantly smaller than previous reports of electron emission for InAs/GaAs QD system [106-108] (note that hole emission is quoted for GaSb/GaAs since the intermediate band transition is near valence band, while electron emission is quoted for InAs/GaAs since the intermediate band transition is near conduction band). The optical generation rate is given by $e_{op} = \sigma_{op} \Phi$ where Φ is the photon flux and σ_{op} is the optical capture cross section [109], The photon flux is given by the irradiance from the solar spectrum that would excite transitions between the GaSb QD states and GaAs valence band. In the solar spectrum, the energy range between the QD activation energy 0.337 eV and the energy separation between the QD confined state and the GaAs conduction band 1.087 eV. The optical cross-section for GaSb/GaAs QDs is not well characterized, but may be approximated by measurement results from Ge/Si QD with an activation energy of 310 meV, where $\sigma_{op} = 2 \times 10^{-13} \text{ cm}^2$ [110]. The resulting optical

emission rate is $2.963 \times 10^4 \text{ sec}^{-1}$ under AM1.5 sunlight and $1.365 \times 10^9 \text{ sec}^{-1}$ under full solar concentration [111]. A comparison of the optical and thermal emission rates and under varying solar concentration is shown in Figure 4.4, where thermal emission is dominant in for AM1.5 illumination, while optical generation becomes dominant under full solar concentration. For a thermal emission rate of $e_{\text{th}} = 3 \times 10^7 \text{ sec}^{-1}$ measured in this work, optical emission in the GaSb/GaAs QDs ($E_A = 0.33\text{eV}$) is predicted to dominant at solar concentration of approximately 1000X and higher. The thermal emission rate may be further reduced in these structures by incorporating barrier layers in proximity of the GaSb/GaAs QDs, where a decrease in cross section is expected for approaches such as the “DFENCE” structure (decrease from $2.6 \times 10^{12} \text{ sec}^{-1}$ to $3 \times 10^9 \text{ sec}^{-1}$ through incorporation of AlGaAs barriers in the InAs/GaAs system) [112], where optical emission rates will become dominant at lower solar concentration.

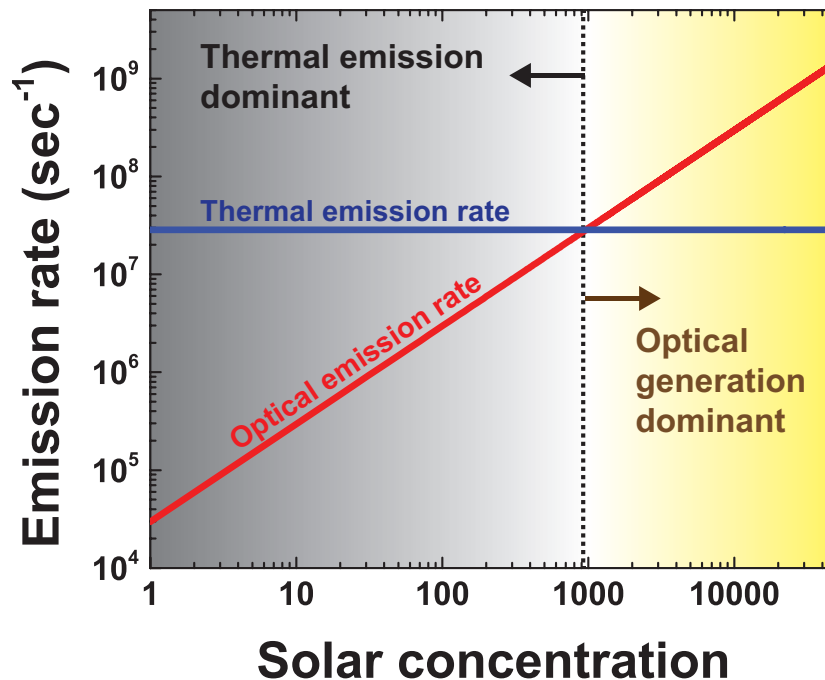


Figure 4.4 Optical (red) and thermal (blue) emission rates of holes in GaSb/GaAs QDs under different solar concentration

4.5. Conclusions

In conclusion, the activation energy and thermal capture cross section of GaSb/GaAs QDs were measured by admittance spectroscopy. The activation energy is in the range of 0.0657 eV – 0.323 eV and exhibits a bias dependence that is consistent with Coulomb charging effects. Activation energy of 0.231 eV – 0.337 eV is obtained that is attributed to the energy separation from the GaSb QD ground state to the GaAs valence band maximum. The thermal capture cross section exhibits a bias-dependence in the range of $\sigma_{th} = 2.0 \times 10^{-16} \text{ cm}^2 - 1.2 \times 10^{-13} \text{ cm}^2$. The measured thermal emission rate is significantly lower than prior reports for InAs/GaAs type-I QDs, and is estimated to be lower than the optical generation rates in an IBSC under solar concentration. The reduced thermal emission rates in the GaSb/GaAs QDs also motivates the study of other material systems with a similar type-II band lineup for future IBSCs.

CHAPTER 5

GaSb/GaAs quantum dot intermediate band solar cells

5.1. Introduction

Intermediate band solar cells (IBSCs) have been developed to surmount the Shockley-Queisser limit of a single junction solar cell by accommodating sub-bandgap photon absorption via absorption bands within the band gap of the host material while preserving the open circuit voltage (V_{oc}). The theoretical estimation of the maximum efficiency of the IBSC is 63.1% under fully concentrated solar irradiation [16], which is comparable to the upper limit of the efficiency of triple-junction solar cells. The IBSCs present one possible way to build a photovoltaic device with multiple energy levels in a single junction while achieving substantial enhancement in the efficiency of the solar energy conversion. Therefore, this strategy can mitigate challenges presented by the multi-junction solar cells that require complicated device structures and fabrication processes.

The intermediate band (IB) can be introduced by confined states in quantum dots (QDs), and InAs/GaSb QD-IBSCs have demonstrated sub-bandgap response and enhancement in photocurrents [22]. However, the excessive thermal emission rates of carriers in the type-I QDs prevent quasi-Fermi level splitting between the conduction band (CB) and the IB, causing the V_{oc} degradation of the IBSC [17], and a substantial

mismatch in the optical transition rates associated with the IB (fast transition rate from the IB to conduction band, $\sim 10^9 \text{ sec}^{-1}$, and slow transition rate from the valence band (VB) to the IB, $\sim 10^3 \text{ sec}^{-1}$ [89]), which is not favorable for enhancing the sub-bandgap response).

To overcome these problems in the type-I QDs, GaSb/GaAs QDs with a type-II band alignment are proposed because (1) the thermal emission rates of carriers in the QD are substantially lower (on the order of 10^7 sec^{-1}) [84, 97, 113] than the rate of the type-I QDs (on the order of 10^{12} sec^{-1}) [106-108] due to a large confinement potential, and (2) the optical interband transition rates in the QDs (from the QD levels to the GaAs CB) can be controlled because of the spatial separation of the electron and hole wavefunctions in the type-II band alignment, allowing better matched optical transition rates.

Previously, GaAs *p-i-n* solar cells containing layers of GaSb self-assembled QD/quantum rings (QRs) in an unintentionally doped intrinsic region have been reported [23, 55]. Laghumavarapu and co-authors [55] have presented GaAs *p-i-n* solar cells with ten layers of the GaSb QDs formed by the interfacial misfit array (strain-free) growth mode, and enhanced spectral response with the inclusion of the QDs in the intrinsic layer has been demonstrated. However, the open circuit voltage (V_{oc}) apparently decreased, and the overall device performance was not improved. Carrington and co-authors [23] also have reported a GaAs *p-i-n* solar cell with five layers of GaSb QDs/QRs in an intrinsic region showing improvement in the short circuit current (J_{sc}) and the sub-bandgap response. However, the V_{oc} was reduced compared to a GaAs control cell, and the efficiency of the solar cell with the GaSb QD/QR layers did not exceed the efficiency of the control cell without QD/QR layers.

5.2. GaSb/GaAs quantum dot growth

In this study, GaSb QDs grown on an Sb-terminated (2×8) surface reconstruction are incorporated in a GaAs p^+n junction in order to introduce an intermediate band in the bandgap of GaAs. All samples used in this work have been grown by Andrew J. Martin and Joanna Millunchick (Material Science and Engineering in the University of Michigan, Ann Arbor) using the molecular beam epitaxy [99]. In order to reconstruct the Sb-terminated (2×8) surface on the GaAs layer, the GaAs surface is exposed to an Sb flux of 0.6 monolayer (ML) sec^{-1} at $T = 580\text{ }^\circ\text{C}$. Once the surface is exposed under Sb overpressure, the temperature of the sample needs to be lowered to the QD growth temperature, $T = 460\text{ }^\circ\text{C}$, at a rate of $30\text{ }^\circ\text{Cmin}^{-1}$. During the cooling process, the Sb-terminated (2×8) surface is constructed, forming a 1.0 ML GaSb wetting layer on the GaAs surface because the Sb replaces the As on the surface through the anion exchange process. Due to the additional wetting layer, a total wetting layer of 2.0 ML is formed after completing the GaSb QD growth. The GaSb QD layers are grown via the Stranski-Krastanov growth mode at $T = 460\text{ }^\circ\text{C}$ and at a GaSb deposition rate of 0.3 MLsec^{-1} with a V/III ratio of 2, resulting in a GaSb layer of 2.3 ML nominal thickness. According to the atomic force microscopy analysis, shown in Figure 5.1, the average QD diameter and height are 34 nm and 2.3 nm, respectively, and the areal density of the QDs is $5.3\times 10^{10}\text{ cm}^{-2}$. The photoluminescence (PL) spectra measured at 10K, shown in Figure 5.2, have a split QD peak at 1.13 eV and 1.18 eV and a WL peak at 1.35 eV. The split QD peak can result from the disintegration of the GaSb QDs upon GaAs capping. [67]

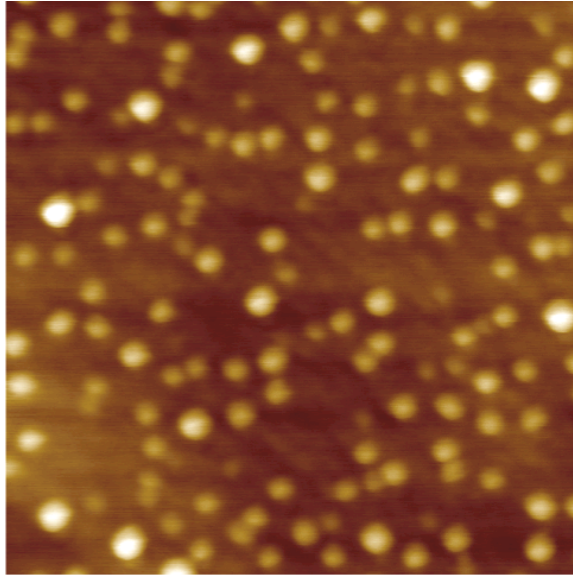


Figure 5.1 AFM images of the uncapped 11th layer of QDs grown on the (2×8) surface with a height scale of 8 nm (adopted from ref [99])

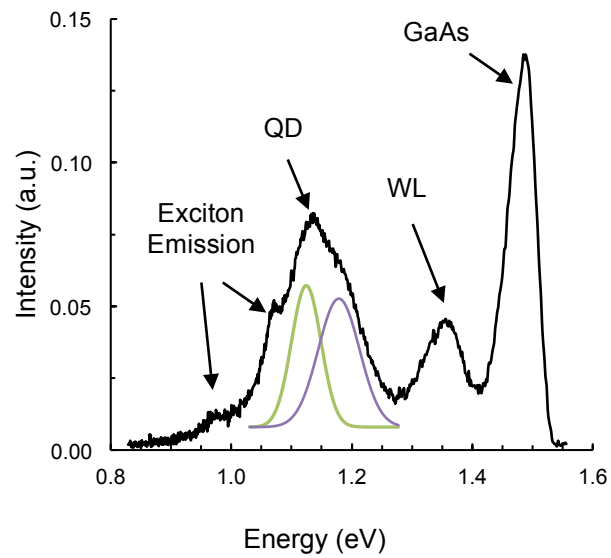
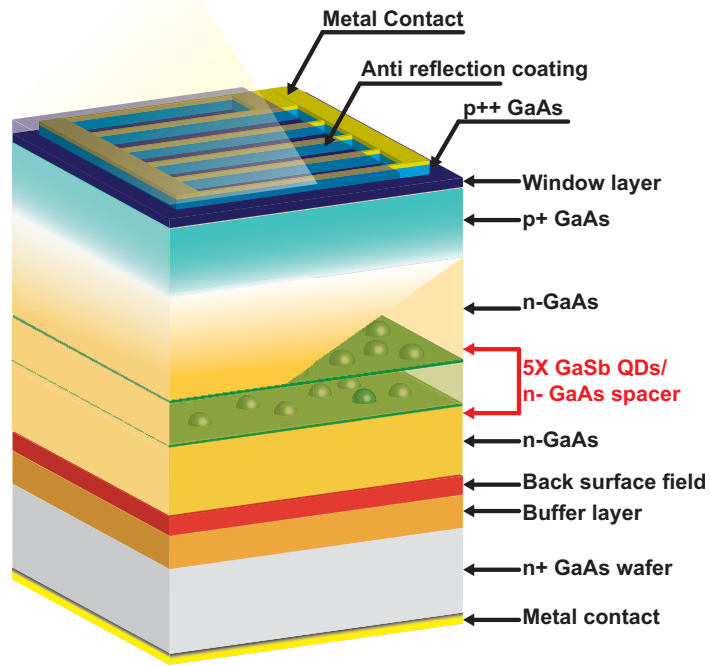


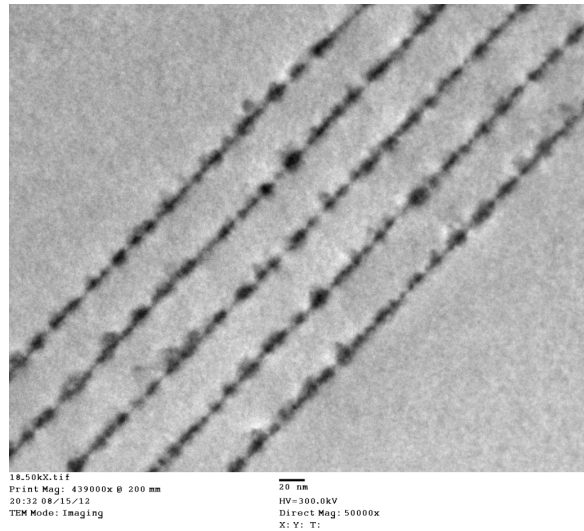
Figure 5.2 Photoluminescence spectra measured at 10K for a sample with ten layers of GaSb QD grown on the (2×8) surface (adopted from ref [99])

5.3. Experimental procedure

GaAs p⁺n junctions with five layers of the GaSb QDs are grown by MBE on heavily n-doped GaAs (001) substrates. The growth of the epitaxial layers starts with a 200 nm thick Si doped n-type GaAs buffer layer grown at T = 590 °C and at a growth rate of 1.0 MLsec⁻¹, followed by the growth of a 150 nm thick n-type Al_{0.3}Ga_{0.7}As back surface field (BSF) layer with doping density of 1×10¹⁸ cm⁻³. Subsequently, a total 3μm thick lightly doped n-type GaAs layer with five layers of the GaSb QDs is grown. The QD growth method is described in section 5.2. All QD layers are immediately capped by a 30 nm GaAs layer, the first 15 nm of which is grown at T = 460 °C at a growth rate of 0.3ML sec⁻¹, and the last 15 nm of which is grown at T = 590 °C at a growth rate of 0.3 ML sec⁻¹ in order to grow a defect-free GaAs layer. The transmission electron microscopy image in Figure 5.3 shows the QD layers embedded in the GaAs solar cell. Finally, a 500 nm thick Be doped p-type GaAs layer with doping density of 4×10¹⁸ cm⁻³ is grown, followed by the growth of a 30 nm thick p-type Al_{0.8}Ga_{0.2}As window layer with doping density of 4×10¹⁸ cm⁻³. On the window layer, a 200 nm heavily doped p-type GaAs layer is grown in order to reduce resistivity at the interface between the top metal grid and the semiconductor, so this layer is etched away during the following fabrication process except the area underneath the top metal grid contact. For comparison, a GaAs p⁺n control sample is also fabricated, which has the same device structure described above but uses five layers of the GaSb QDs.



(a)



(b)

Figure 5.3 (a) A complete structure of GaAs p^+n solar cell with five layers of GaSb QD and (b) scanning transmission electron microscope image of the QD layers in the solar cell (from Sung Joo Kim and Xiao Pan, Material Science Engineering, University of Michigan)

Unlike in previous reports [23, 55] studying the *p-i-n* GaAs solar cells with the GaSb QD layers in the intrinsic GaAs layer, we place the GaSb QD layers in the lightly doped n-GaAs layer in order to balance the optical transitions of carriers from the VB to the QD levels and from the QD levels to the CB. According to the results from the admittance measurement and the deep level transient spectroscopy measurement, the thermal emission/capture rates of the carriers in the GaSb QDs at room temperature are much faster than the optical transition rates from the VB to the QD states under unconcentrated solar irradiation. Under this condition, therefore, electrons need to be intentionally injected into the QD confined states by n-type doping in order to enhance the sub-bandgap response of the IBSC.

The MBE grown GaAs p^+n junctions are fabricated into the square solar cells of area $0.25\text{cm}\times 0.25\text{ cm}$, and all devices are mesa isolated. Pd/Zn/Pd/Au and Ni/Ge/Au/Ti/Au Ohmic contacts are deposited on the top p^+ -GaAs and backside n^+ -GaAs, respectively, followed by rapid thermal annealing at $400\text{ }^\circ\text{C}$. On the top surface of the solar cells, ZnS and MgF_2 layers are deposited successively as an Anti-reflection coating [114].

The current density-voltage (J - V) characteristics of the solar cells are measured under simulated Atmospheric Mass 1.5 Global (AM 1.5G) illumination at 1 sun ($100\text{mW}/\text{cm}^2$) intensity, and a National Renewable Energy Laboratory certified Si reference photovoltaic cell is used to calibrate the optical power intensity. The external quantum efficiencies (EQE) of the solar cells are measured in wavelengths ranging from 400 nm to 1100nm by a setup composed of a tungsten lamp, monochromator, light chopper, and lock-in amplifier. To validate the measurement EQE data, the integration of

the EQE spectrum with the AM1.5G spectrum is compared to the short circuit current obtained from the J - V characteristics while recognizing the discrepancy arising from the lack of EQE data in the range of wavelengths shorter than 400 nm.

5.4. Results and discussion

In order to examine the effect of the electric field crossing the QD layers, a GaAs p⁺n solar cell with five layers of the GaSb QDs placed in the flat band region of the n-GaAs (QD-IBSC) is fabricated along with a control sample without the GaSb QD layers, where the internal electric field does not exist at the equilibrium. The details of the solar cell structure and the band diagram are described in Figure 5.4. The measured J - V under the 1 sun (AM 1.5G simulated solar irradiation) of the QD-IBSC and the control sample are shown in Figure 5.6 (a), and the device characteristics obtained from the curves are listed in Table 5.1. In addition, the diode parameters of the curves in Figure 5.5 (a) are obtained by fitting the data numerically based on a simple diode model defined by

$$J = J_{ph} - J_0 \left[\exp\left(\frac{V + JR_s}{n_d k_B T}\right) - 1 \right] - \frac{V + JR_s}{R_{sh}} \quad (5.1)$$

where J_{ph} , J_0 , n_d , R_s , and R_{sh} represent the photogenerated current, the reverse saturation current, the diode ideality factor, the series resistance, and the shunt resistance, respectively. In this work, the implicit function (5.1) is converted to an explicit function using the Lambert W-function

$$J = -\frac{n_d k_B T}{R_s} \text{LambertW} \left(\frac{R_s J_0 R_{sh} \exp\left(\frac{R_{sh} (R_s J_{ph} + R_s J_0 + V)}{n_d k_B T (R_s + R_{sh})}\right)}{n_d k_B T (R_s + R_{sh})} \right) + \frac{R_{sh} (J_0 + J_{ph}) - V}{R_s + R_{sh}} \quad (5.2)$$

in order to avoid unnecessary numeric approximations and reduced calculation power. Fitting results are also plotted in Figure 5.5 and the diode parameters of the curves are listed in Table 5.1.

The V_{oc} and the efficiency of the QD-IBSC are 0.89 eV and 13.01%, increases of 0.27 eV and 1.61% relative to the previous results [23], respectively. However, although the diode parameters of the QD-IBSC are comparable to those of the control cell, the presence of the GaSb QD leads to significant J_{sc} degradation, which is not consistent with the previous results. In addition, the EQE spectrum at the equilibrium (0V) shown in Figure 5.6 (a) shows a significant drop in the EQE in the range of the wavelengths from about 650 nm to about 900 nm (labeled ‘zone 2’), and the sub-bandgap response does not appear in the range of wavelengths longer than the cutoff wavelength of the GaAs bandgap (labeled ‘zone 3’). In order to analyze the origins of the drop in EQE, the contributions to the EQE from different cell regions (emitter, space charge region, and base) are fitted based on the excessive minority carrier diffusion equation in a p-n junction

$$\frac{d^2 \Delta n(x)}{dx^2} - \frac{\Delta n(x)}{L^2(x)} = -\frac{g(x)}{D} \quad (5.3)$$

where $\Delta n(x)$ is the excessive minority carrier, and L and D represent the minority carrier diffusion length and diffusion coefficient. The generation profile, $g(x)$, is expressed by

$$g(x) = \alpha F(1 - R)\exp(-\alpha x) \quad (5.4)$$

with α the absorption coefficient, F the photon flux from the sun, and R the reflectivity of the front surface of the cell. In this study, the reflectivity R of the stack of the anti-reflection coating and the window layer (105nm MgF_2 / 45 nm ZnS / 30 nm $Al_{0.8}Ga_{0.2}As$) is calculated based on the transfer-matrix method. With the solution of the equation (5.3)

and the photon flux from the sun, the contribution of the emitter and the base to the EQE can be expressed by

$$EQE_E(\lambda) = (1 - R(\lambda)) \times \frac{\alpha L_E}{(\alpha L_E)^2 - 1} \times \left[\frac{\frac{S_E L_E}{D_E} + \alpha L_E - \left(\left(\frac{S_E L_E}{D_E} \right) \cosh\left(\frac{w_E}{L_E}\right) + \sinh\left(\frac{w_E}{L_E}\right) \right) \exp(-\alpha w_E)}{\left(\frac{S_E L_E}{D_E} \right) \sinh\left(\frac{w_E}{L_E}\right) + \cosh\left(\frac{w_E}{L_E}\right)} - \alpha L_E \exp(-\alpha w_E) \right] \quad (5.5)$$

$$EQE_B(\lambda) = (1 - R(\lambda)) \times \frac{\alpha L_B}{(\alpha L_B)^2 - 1} \exp[-\alpha(w_E + w_{SCR})] \times \left[\alpha L_B - \frac{\left(\frac{S_B L_B}{D_B} \right) \cosh\left(\frac{w_B}{L_B}\right) + \sinh\left(\frac{w_B}{L_B}\right) + \left(\alpha L_B - \frac{S_B L_B}{D_B} \right) \exp(-\alpha w_B)}{\left(\frac{S_B L_B}{D_B} \right) \sinh\left(\frac{w_B}{L_B}\right) + \cosh\left(\frac{w_B}{L_B}\right)} \right] \quad (5.6)$$

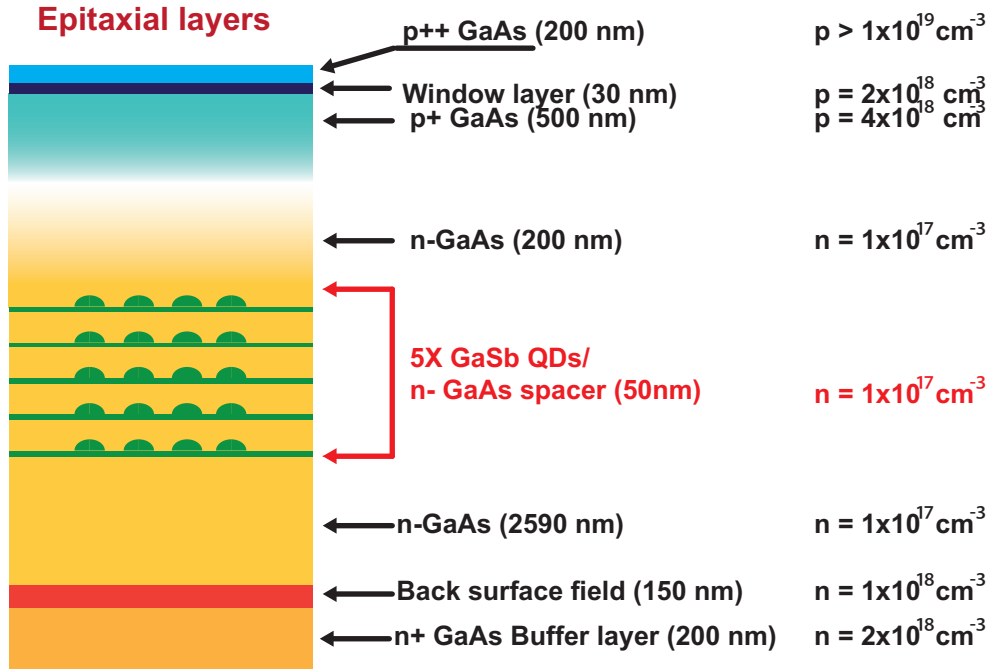
where S_E and S_B represent the surface recombination velocity of the front and the back surfaces, respectively, and w_E , w_{SCR} , and w_B stand for the thickness of the emitter, the space charge region and the base. The contribution of the space charge region can be described by assuming that recombination in the region can be ignored:

$$EQE_{SCR}(\lambda) = (1 - R(\lambda)) \times \exp(-\alpha w_E) (1 - \exp(-\alpha w_{SCR})) \quad (5.7)$$

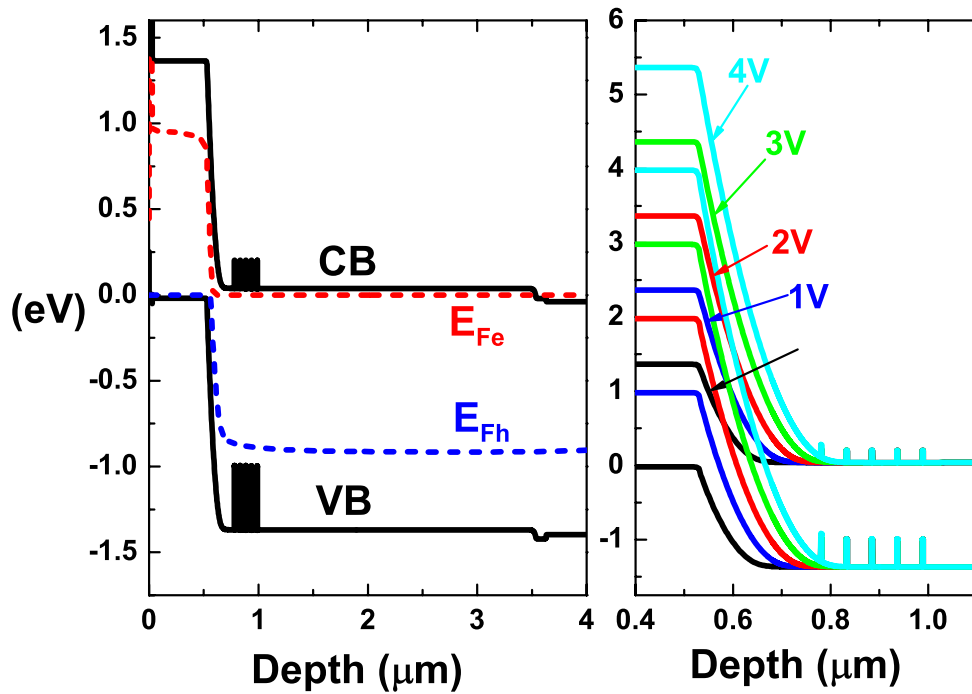
Finally, the total EQE can be obtained by adding all the contributions

$$EQE(\lambda) = EQE_E(\lambda) + EQE_B(\lambda) + EQE_{SCR}(\lambda) \quad (5.8)$$

The EQE fitting results of the control cell and the QD-IBSC are shown in Figure 5.6 (b) and Figure 5.6 (c), respectively, along with the measured data. According to the fitting results shown Figure 5.6 (c), the contribution from the base where the GaSb QD layers are placed has almost disappeared in the EQE of the QD-IBSC.

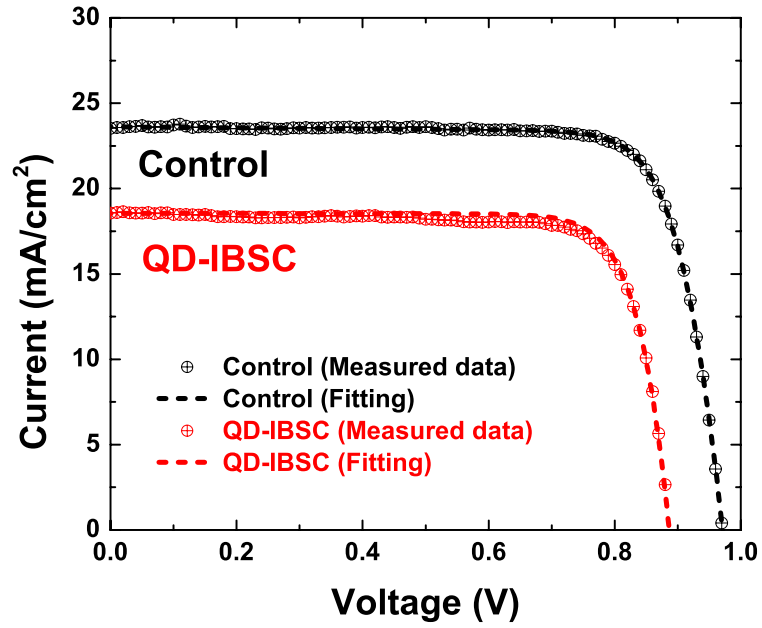


(a)

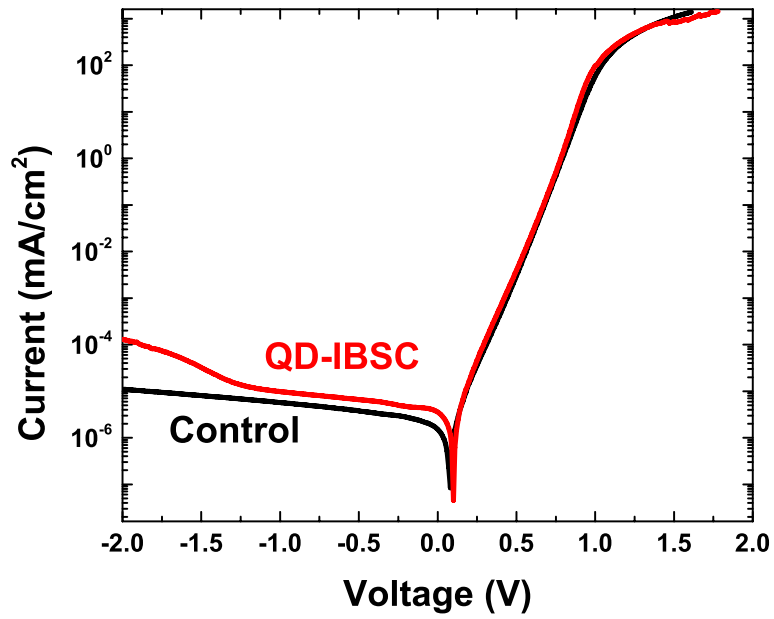


(b)

Figure 5.4 (a) Details of the GaAs p+n solar cell structure and (b) the band diagram of the device at the equilibrium and under the reverse biases of 1V, 2V, 3V, and 4V.

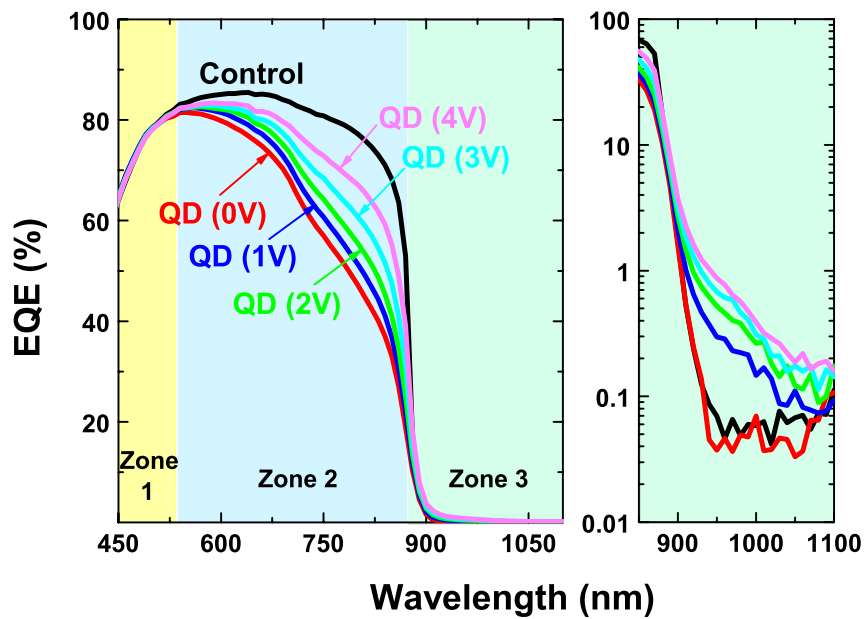


(a)

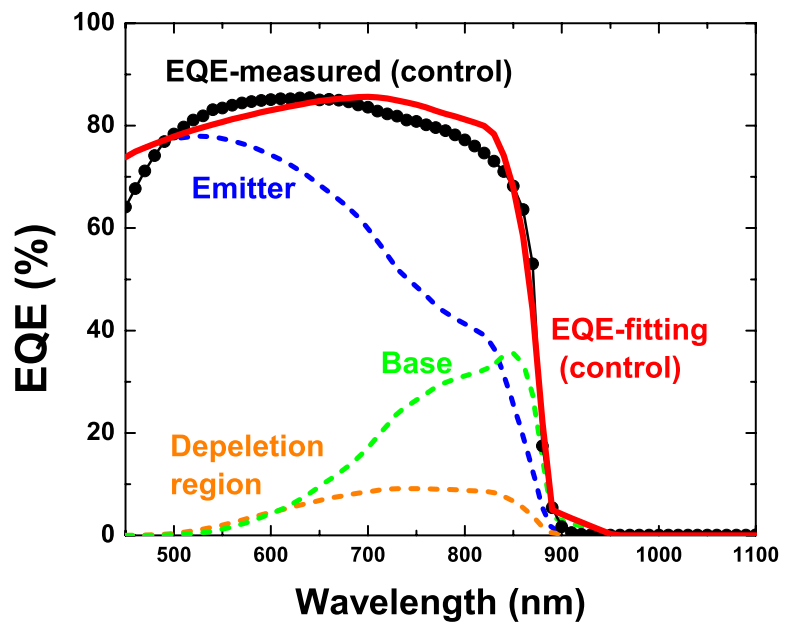


(b)

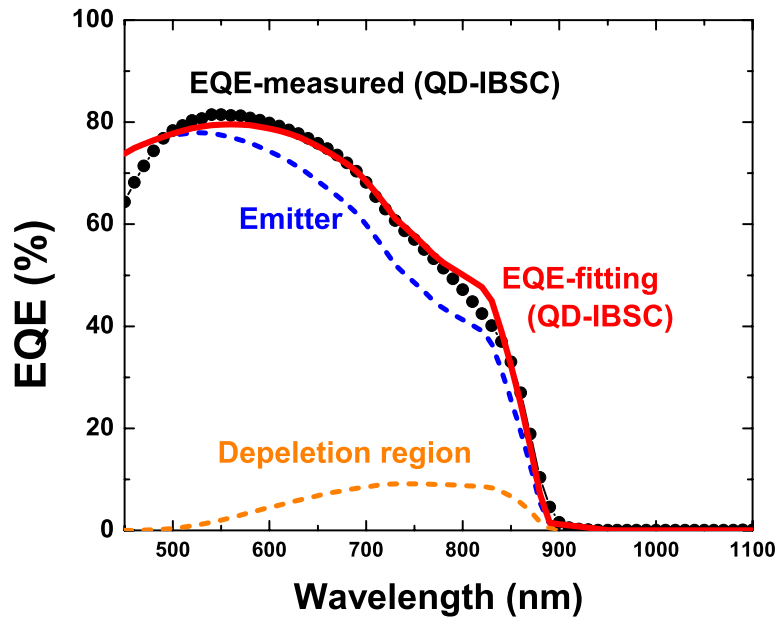
Figure 5.5 Current density vs voltage (J - V) characteristics measured (a) under the 1 sun, AM 1.5G simulated solar irradiation and (b) the dark condition



(a)



(b)

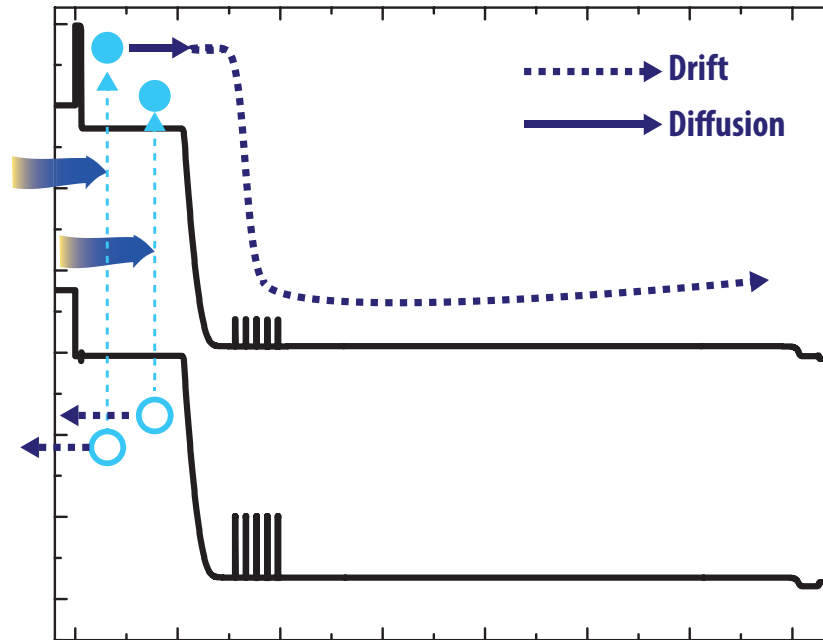


(c)

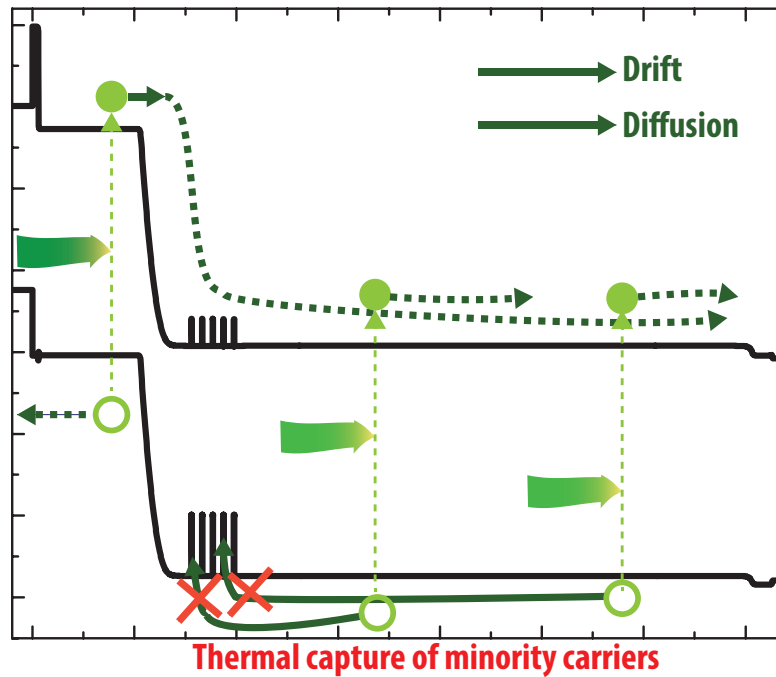
Figure 5.6 (a) EQE spectra at the equilibrium and under the reverse biases of 1V, 2V, 3V, and 4V of the GaAs p^+n solar cell with the five layers of GaSb QDs and the control cell without the QD layers. (b) Contributions of the emitter, space charge region, and the base to EQEs of the control and (c) the QD-IBSC

The possible reasons for the loss of the base contribution to the EQE and the sub-bandgap response can be explained with Figure 5.7. Unlike the minority carriers generated by the short wavelength photons absorbed almost completely near the surface of the device described in Figure 5.7 (a), the minority carriers generated by the long wavelength absorbed in the base need to be diffused across the QD layers to be collected by the topmost p-contact described in Figure 5.7 (b). In this case, many of the carriers can be captured into the QDs' confined states, resulting in a reduction of the contribution of the base to the EQE. In addition, although the sub-bandgap photon absorption occurred via the QD states, the sub-bandgap response can be quenched if the electron-hole pairs

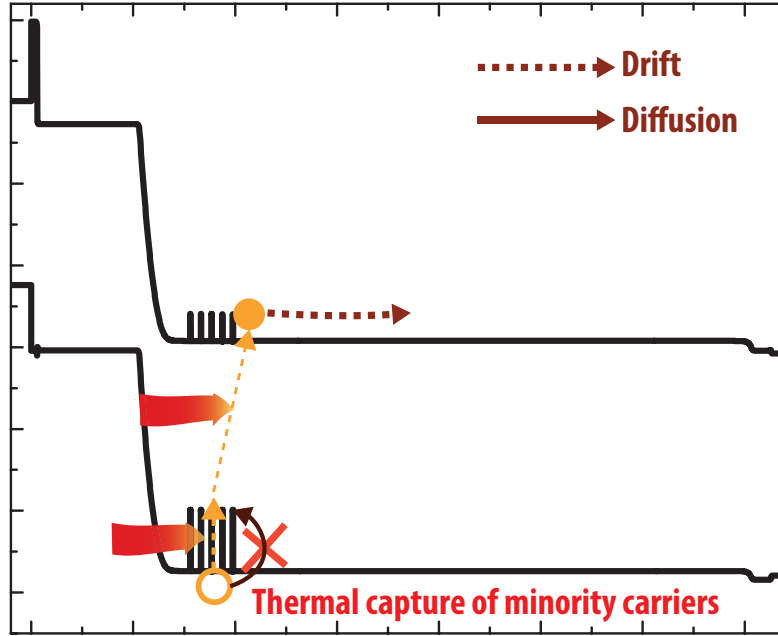
generated within the QDs are captured back to the QD states before they escape to the GaAs junction, as shown in Figure 5.7 (c).



(a)



(b)



(c)

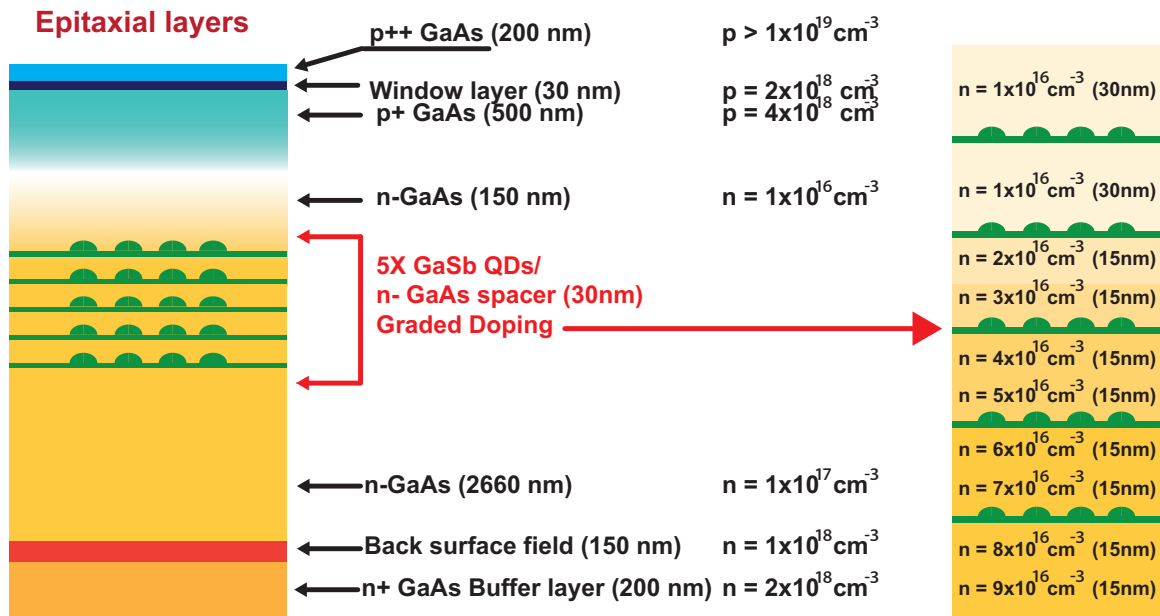
Figure 5.7 Schematic illustration of the carrier transport in the GaAs p^+n junction with the GaSb QD layers under the irradiation of (a) short-wavelength photons, (b) long-wavelength photons, and (c) photons with energy less than the GaAs bandgap

A reverse bias is applied to the QD-IBSC to extend the space charge region of the device into the region where the QD layers are placed in order to introduce an electric field across the QD layers. The EQE spectra under the various reverse biases are given in Figure 5.6 (a), showing that the EQE spectra in zone 2 recover close to the EQE spectrum of the control cell, and the sub-bandgap response starts to appear to be increasing the reverse bias. The results imply that the electric field across the QD layers can improve carrier transport across the QD layers and alleviate the thermal capture of the carriers into the QD confined states. However, according to the dark $J-V$ results of the QD-IBSC shown in Figure 5.5 (b), the V_{oc} may decrease as the QD layers are placed close to the

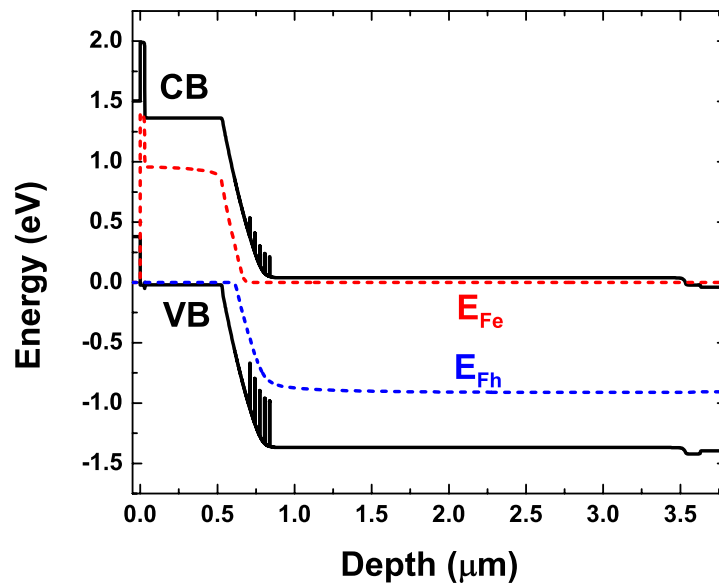
space charge region because the reverse saturation current of the QD-IBSC increases abruptly as the reverse bias increases.

Based on the above results, another GaAs p^+n solar cell with five layers of the GaSb QDs placed in the graded doping region is fabricated in order to build the internal electric field across the QD layers while keeping them away from the space charge region. Shown in Figure 5.8, the n-GaAs base layer is composed of three regions: (1) a flat band region with constant doping of $1 \times 10^{17} \text{ cm}^{-3}$ (bottom), (2) a region with doping concentration gradually decreasing from $1 \times 10^{17} \text{ cm}^{-3}$ to $1 \times 10^{16} \text{ cm}^{-3}$ where five layers of the GaSb QDs are placed with a spacing of 30 nm (middle), and (3) a completely depleted region with constant doping of $1 \times 10^{16} \text{ cm}^{-3}$ (top). The thickness of the layer (3) is chosen to locate the QD layers at the edge of the space charge region in order to retain the higher V_{oc} of the previous QD-IBSC than the V_{oc} of the $p-i-n$ QD-IBSCs.

Figure 5.9 shows that the J_{sc} and the EQE of the QD-IBSC with the graded junction are improved compared to the device described in Figure 5.4, and the sub-bandgap response appears in the EQE spectrum. In particular, the J_{sc} of the QD-IBSC with the graded junction exceeds that of the control cell. However, the V_{oc} decreases to 0.73V. (The device characteristics and diode parameters of the device are listed in Table 5.1.) Therefore, the location of the QD layers in the n-GaAs base needs to be optimized to minimize the V_{oc} degradation while maintaining the J_{sc} enhancement in order to improve the conversion efficiency of the solar cell. In addition, the details of the mechanisms of the V_{oc} drop, which generally appears in the QD-IBSCs, need to be examined in order to improve the overall solar cell performance of the QD-IBSCs.

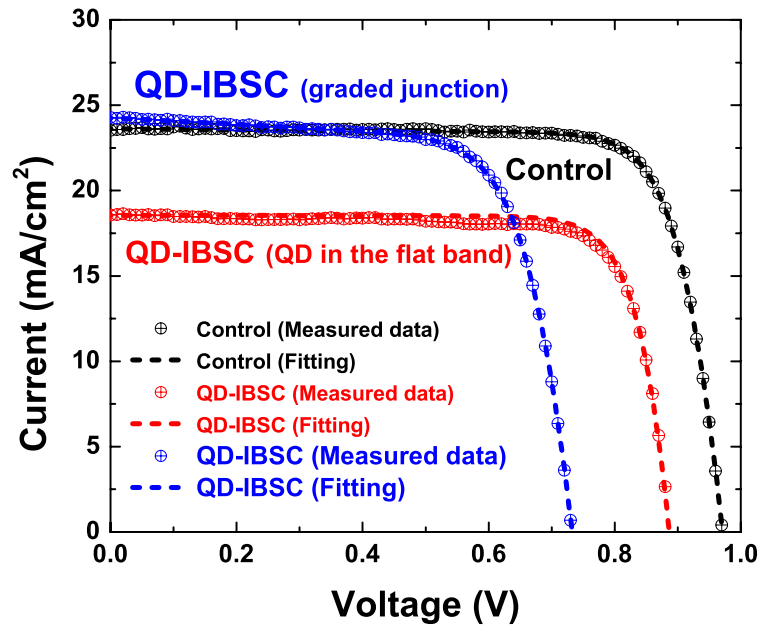


(a)

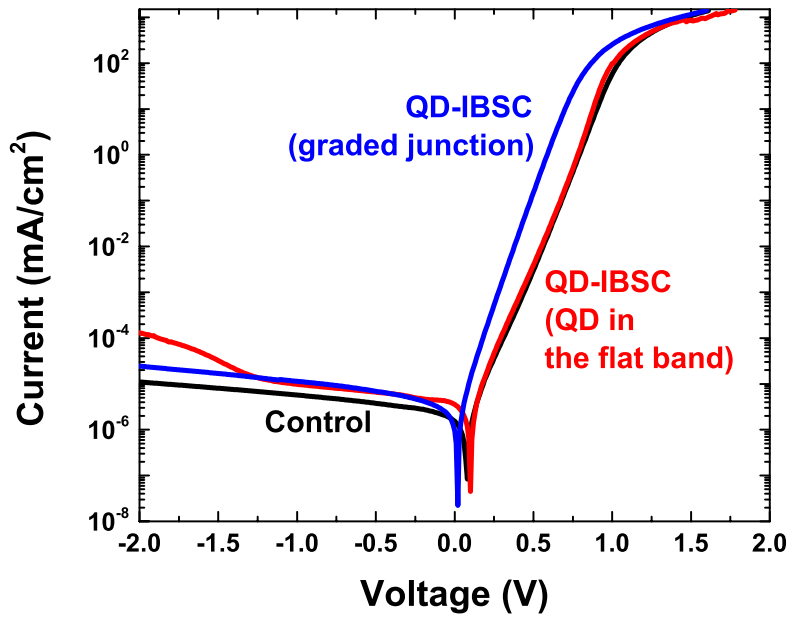


(b)

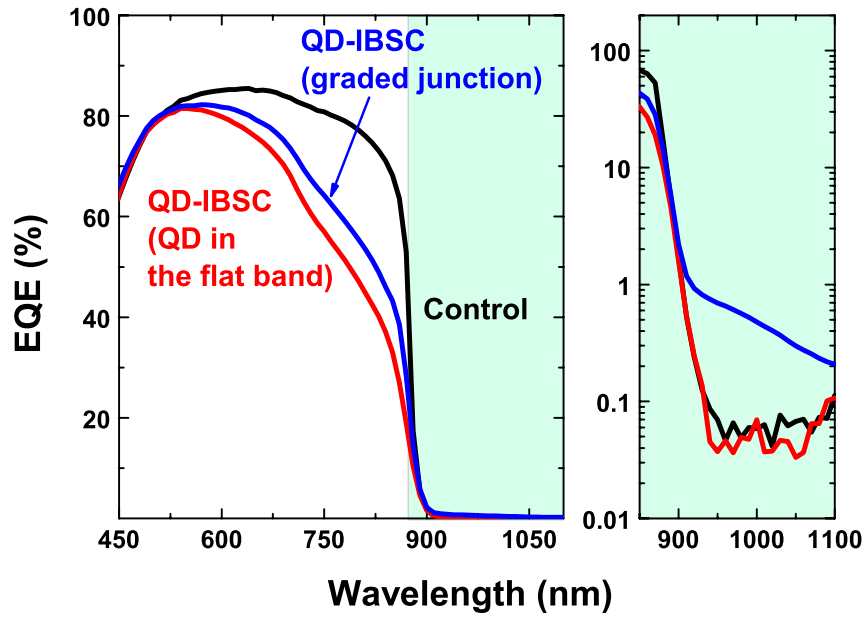
Figure 5.8 (a) Device structure and (b) the band diagram of the GaAs p⁺n solar cell with the five layers of GaSb QDs placed in the graded junction



(a)



(b)



(c)

Figure 5.9 Current density vs voltage (J - V) characteristics measured under (a) the 1 sun, AM 1.5G simulated solar irradiation and (b) the dark environment, and (c) EQE spectra of the GaAs p^+n solar cell with the five layers of GaSb QDs placed in the graded junction (results from Figure 5.5 and Figure 5.6 are also plotted for comparison)

Table 5.1 Solar cell characteristics measured under the AM 1.5G spectrum

	Control	QD-IBSC (QD in the flat band)	QD-IBSC (graded junction)
J_{sc} (mA/cm ²)	23.67	18.56	24.28
V_{oc} (V)	0.97	0.89	0.73
Fill Factor	0.84	0.79	0.71
Efficiency (%)	19.22	13.01	12.61
n_d	1.55	1.54	1.83
J_0 (mA/cm ²)	6.64×10^{-10}	4.05×10^{-9}	4.23×10^{-6}
R_s (Ω)	1.91×10^{-2}	9.08×10^{-3}	1.62×10^{-2}
R_{sh} (Ω)	5.34×10^1	3.44×10^2	7.74

5.5. Conclusions

In conclusion, the GaSb/GaAs QD IBSCs with various structures are fabricated to demonstrate that the sub-bandgap response occurred through sub-bandgap photon absorption via the QD confined states. In order to enhance the sub-bandgap response where the thermal capture/emission of carriers to the GaSb QD confined states is dominant over the optical transition at room temperature, the QD layers are incorporated in the lightly n-doped base of the p⁺n GaAs junction to compensate for the carrier loss through the thermal process by intentionally injecting electrons with n doping. According to the J - V and EQE characteristics of the devices fabricated in this work, the location of the GaSb QD layers can affect the V_{oc} , J_{sc} , and the overall conversion efficiency. If the GaSb QD layers are placed far away from the edge of the space charge region of the

junction, the degradation of the V_{oc} can be minimized while the sub-bandgap response disappears and the QD layer can disturb carrier transport. On the other hand, if the QD layers are completely inside of the space charge region of the junction, the sub-bandgap response is enhanced while V_{oc} is degraded. Therefore, the trade-off between V_{oc} and the sub-bandgap response can be optimized by adjusting the location of the QD layers in the space charge region in order to improve the overall conversion efficiency of the solar cells. In addition, by introducing the internal electric field across the QD layers with guardedly doped junction, the sub-bandgap response can be improved while minimizing the V_{oc} degradation.

CHAPTER 6

Conclusion

6.1. Summary of present work

6.1.1. Strain-balanced GaAsBi/GaAsN superlattice on GaAs

GaAs alloys with dilute content of Bi and N provide a large reduction in bandgap energy with increasing alloy composition. GaAsBi/GaAsN heterojunctions have a type-II band alignment, where superlattices based on these materials offer a wide range of possibilities for designing effective bandgap energy by varying superlattice periods and alloy compositions. The miniband structure and effective bandgap for strain-balanced GaAsBi/GaAsN superlattices with effective lattice matches to GaAs are calculated for alloy compositions up to 5% Bi and N using the **k.p** method. The effective bandgap for these superlattices is found to vary between 0.89eV to 1.32eV for period thicknesses ranging from 10Å-100Å. The joint density of states and optical absorption of a 40Å/40Å GaAs_{0.96}Bi_{0.04}/GaAs_{0.98}N_{0.02} superlattice are reported, demonstrating a ground state transition at 1.005eV and first excited transition at 1.074eV. The joint density of states is similar in magnitude to GaAs, while the optical absorption is approximately one order of magnitude lower due to the spatially indirect optical transition in the type-II structure. The GaAsBi/GaAsN system may provide a new material system with a lattice matched to

GaAs in a spectral range of high importance for photovoltaic devices, especially for the multi-junction solar cells that use the materials near 1 eV bandgap.

6.1.2. Type-II GaSb/GaAs self-assembled quantum dots

The strain distribution and electronic structure for type-II GaSb/GaAs self-assembled quantum dots are calculated using the valence force field model and the **k.p** method. The strain distributions in the QD obtained by the VFF mode are applied to derive the position of the electron, HH, and LH potential profile, showing the larger bandgap of the QD than that of bulk GaSb and the significance of the HH and LH band split on the VB of GaSb. According to the 8-band **k.p** calculations, the single-particle confined states in the QDs are closely spaced compared to the electron states of the InAs QDs because the effective mass of holes is greater than that of electrons. The energy of the QD peak in the PL spectra is in accordance with the transition energy from the CB edge of GaAs to the ground state of the QD. The fully occupied QD states are also calculated with the single-particle wavefunctions by considering the repulsive Coulomb energy between the confined holes in the QD as a perturbation, and the number of states in the fully occupied QD agrees well with the number of holes within the fully occupied QD derived from the capacitance-voltage measurement.

The thermal carriers' capture and escape mechanisms and the activation energy of the process are studied for GaSb/GaAs quantum dots with a type-II band alignment using admittance spectroscopy. Clear signatures are observed corresponding to confined quantum dot states with extracted activation energy of 0.337 eV and the thermal capture cross section in the range from $2.10 \times 10^{-16} \text{ cm}^2$ to $1.19 \times 10^{-13} \text{ cm}^2$. The thermal emission rates in the GaSb/GaAs quantum dots are significantly lower than prior reports for type-I

systems, where optical emission is predicted to be the dominant process in an intermediate band solar cell under solar concentration.

Finally, the GaSb/GaAs QD IBSCs are fabricated, and the sub-bandgap response via the GaSb/GaAs QD is demonstrated. In this work, GaAs p+n junctions are employed, and the multiple layers of GaSb QDs are incorporated in the lightly doped n-layer in order to compensate for carrier loss in the QDs through the thermal emission/capture process by intentionally injecting electrons with n doping at room temperature. The J - V and EQE characteristics from the devices show that the location of the QD layers and the electric field crossing the QD layers can affect the V_{oc} , J_{sc} , and the overall conversion efficiency. The results from the QD-IBSC with the QD layers placed in the flat band region of the n-GaAs layer where the electric field crosses the QD layer are negligible, showing the least degradation of the V_{oc} while the sub-bandgap response disappears and the QD layers disturb the carrier transport. On the other hand, the results from the QD-IBSC with the QD layers placed inside of the depletion region of the junction where the internal electric field of the junction crosses the QD layers show the substantial enhancement of the sub-bandgap response while V_{oc} is degraded. Based on the results, the GaAs spacer with the graded doping profile [need a verb here but I'm not sure what; perhaps “was used”? Or “is preferable”? in order to introduce the internal electric field across the QD layers while keeping the QD layers outside of the junction. The results from the device show the enhanced sub-bandgap response and the less degraded V_{oc} .

6.2. Future works

6.2.1. Strain compensation layers

According to the VFF calculation in section 3.2.2, the biaxial strain (tensile strain) penetrates deep into the GaAs capping layer. If the capping layer is not thick enough to release the strain before growing the next GaSb QD layer, the strain energy accumulates in the stack as more QD layers grow. At some point, the accumulation of strain energy starts to introduce dislocations in the epitaxial layers in order to release the strain energy, shown in Figure 6.1. Once the dislocations are formed in the solar cell, the device performance degrades because the defects increase the non-radiative recombination in the device.

On the other hand, if the GaAs capping layer is too thick, some of the QD layers will be placed out of the electric field region, and those layers can interfere with the carrier transport and the energy conversion process of the sub-bandgap photons via the QD confined states.

In order to avoid the strain accumulation in the multiple QD layer structure while keeping the GaAs spacer thickness thin, we suggest incorporating a strain compensation layer in the middle of the GaAs spacer. By insulating adding the thin layer with a larger lattice constant than that of GaAs within the spacer layer, a compressive strain can be introduced, resulting in strain compensation with the tensile strain originating from the GaSb QD. This strategy has been introduced in the InAs/GaAs QD IBSCs and demonstrated improvement in the device performance [22]. Bailey and co-authors introduced very thin Ga(As)P strain compensating layer in the middle of the GaAs spacer

of the InAs/GaAs QD-IBSCs, and the device has demonstrated near 1eV V_{oc} and enhanced J_{sc} compared to the control sample without the InAs QD layers.

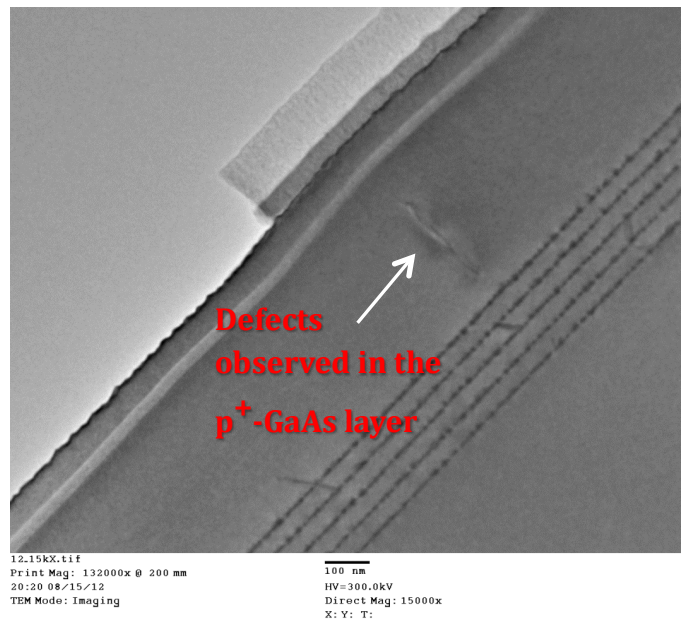
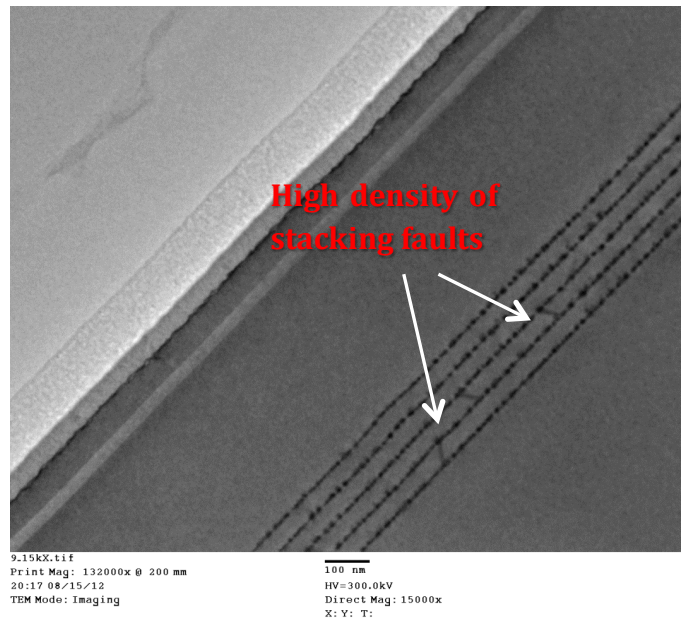


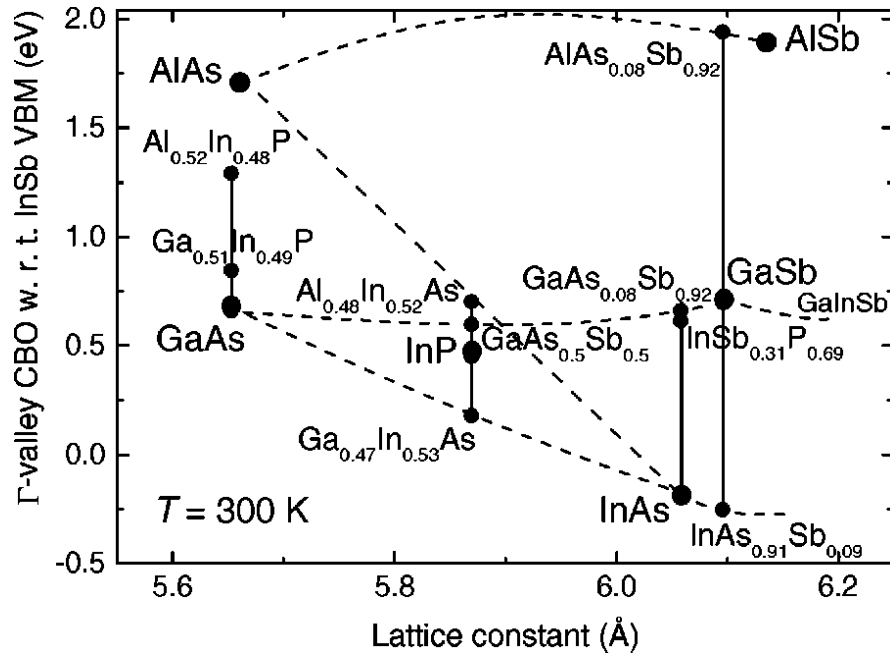
Figure 6.1 Scanning transmission electron microscope images of the QD layers in the solar cell that have dislocations due to the strain accumulation from the QD layers (from Sung Joo Kim and Xiao Pan, Material Science Engineering, University of Michigan)

6.2.2. Quantum-dot-in-a-fence (DEFENCE) heterostructure

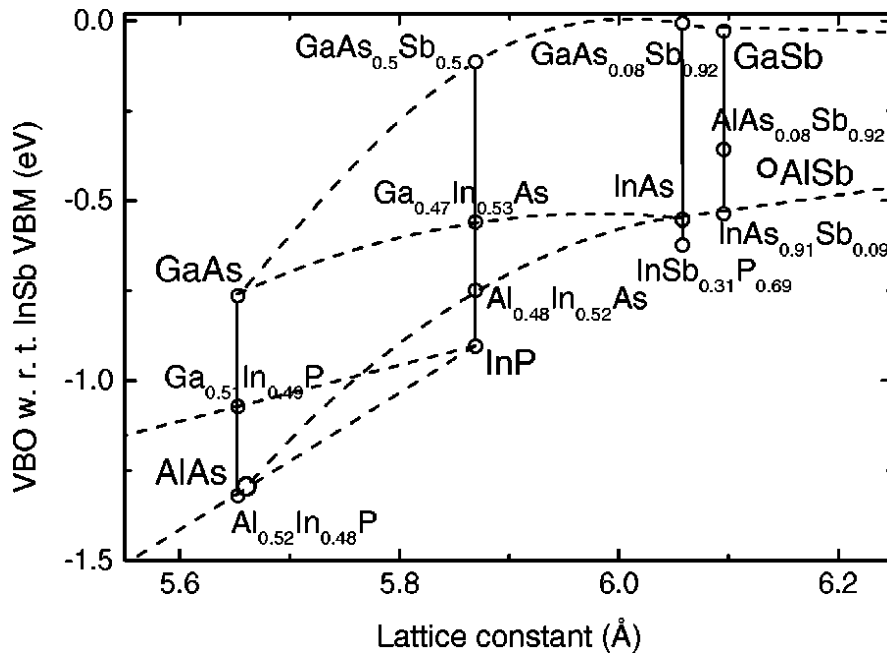
In order to reduce the thermal emission/capture rate in the QD, we suggest incorporating the Quantum-dot-in-a-fence (DEFENCE) heterostructure [112]. Although the thermal emission rates of the GaSb QD are lower than the rate of type-I InAs/GaAs QDs, the rates exceed the optical transition rates from the VB of GaAs to the GaSb QD confined states at room temperature. In this condition, the thermal emission/capture process in the GaSb QDs results in a substantial thermal connection between the QD confined states and the VB of GaAs, preventing the quasi-Fermi level splitting between these levels, which is required to preserve the V_{oc} of the IBSC. Therefore, the thermal emission/capture rates at room temperature need to be reduced further below the intrasubband optical transition rates in the QDs. One of the possible methods is introducing a quantum-dot-in-a-fence (DEFENCE) heterostructure in the IBSCs. Wei and Forrest [112] have theoretically shown that including the thin fence barriers ($Al_xGa_{1-x}As$) surrounding InAs QDs can reduce thermal emission rates of the carriers in the QDs and enhance photocarrier generation without affecting V_{oc} .

For the type-II GaSb/GaAs QD IBSC, a thin layer of $Ga_{0.51}In_{0.49}P$ can be a promising candidate for the DEFENCE heterostructure. According to Figure 6.2, the lattice constant of $Ga_{0.51}In_{0.49}P$ is matched to that of GaAs, and the band gap of $Ga_{0.51}In_{0.49}P$ is 0.49 eV higher than that of GaAs [75]. In addition, the band alignment of $Ga_{0.51}In_{0.49}P/GaAs$ is more suitable to the type-II GaSb/GaAs QD system than that of $AlGaAs/GaAs$ because the valence band offset (VBO) between $Ga_{0.51}In_{0.49}P/GaAs$ (0.31 eV) is greater than the conduction band offset (CBO) of the heterostructure (0.18 eV), introducing a barrier to the holes in the QD confined states on the valence band while

decreasing the effect of an undesirable barrier on the conduction band that can interfere electron transport. A schematic structure of the $\text{Ga}_{0.51}\text{In}_{0.49}\text{P}$ DEFENCE is illustrated in Figure 6.3 (a), and the expected band diagram is plotted in Figure 6.3 (b) based on the material parameters provided in ref [75].

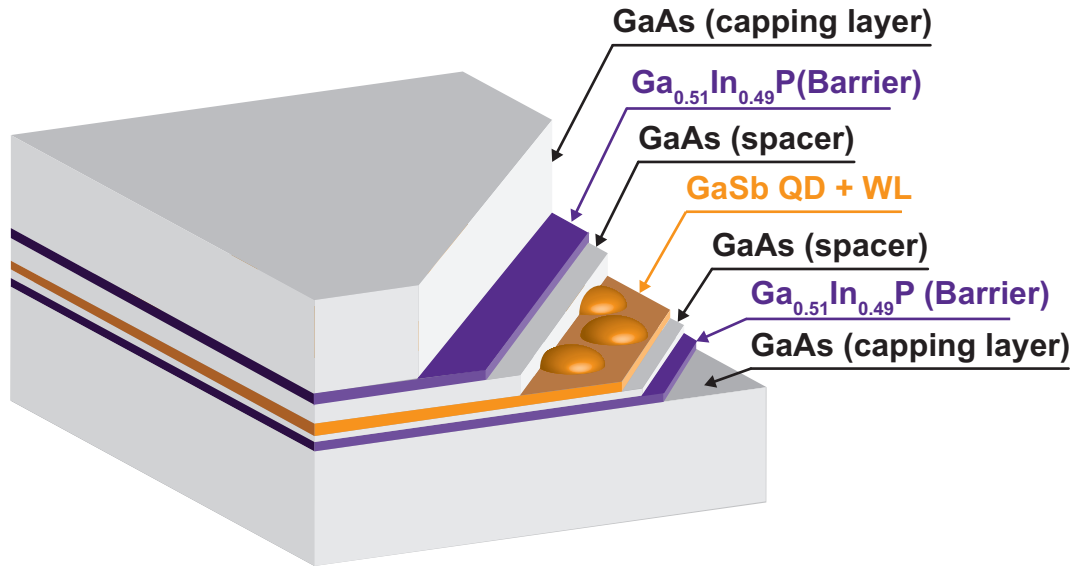


(a)

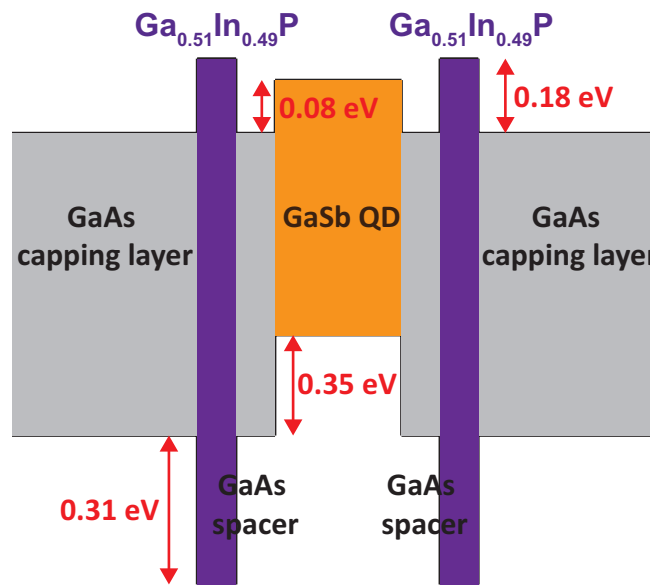


(b)

Figure 6.2 (a) Conduction band offsets and (b) valence band offsets of the III-V semiconductors as a function of lattice constant (adopted from ref [75])



(a)



(b)

Figure 6.3 (a) Structure of the quantum-dot-in-a-fence barrier with $\text{Ga}_{0.51}\text{In}_{0.49}\text{P}$ and (b) the expected band diagram of the heterostructure

APPENDICES

APPENDIX A

Eight-band $\mathbf{k}\cdot\mathbf{p}$ model within the envelope function approximation

The eight-band $\mathbf{k}\cdot\mathbf{p}$ model within the envelope function approximation is widely used to calculate the electronic structure of semiconductor heterostructures when the coupling between the conduction, heavy-hole, light-hole, and spin-orbit bands needs to be considered carefully in the electronic structure of the system.

In the formula, the wavefunction can be expanded in terms of the basis $|i\rangle$,

$$\Psi(\vec{r}) = \sum_{i=1}^8 \Phi_i(\vec{r})|i\rangle \quad (\text{A.1})$$

where $|i\rangle$ is the Γ point Bloch functions of the conduction, heavy-hole, light-hole, and spin-orbit bands corresponding to Γ_6 , Γ_7 , and Γ_8 of the zinc-blend crystal

$$\begin{aligned} |1\rangle &= |S\rangle \uparrow \\ |2\rangle &= |S\rangle \downarrow \\ |3\rangle &= \left| \frac{3}{2}, \frac{3}{2} \right\rangle = -\frac{1}{\sqrt{2}} (|p_x\rangle + i|p_y\rangle) \uparrow \\ |4\rangle &= \left| \frac{3}{2}, \frac{1}{2} \right\rangle = -\frac{1}{\sqrt{6}} [(|p_x\rangle + i|p_y\rangle) \downarrow - 2|p_z\rangle \uparrow] \\ |5\rangle &= \left| \frac{3}{2}, -\frac{1}{2} \right\rangle = \frac{1}{\sqrt{6}} [(|p_x\rangle - i|p_y\rangle) \uparrow + 2|p_z\rangle \downarrow] \\ |6\rangle &= \left| \frac{3}{2}, -\frac{3}{2} \right\rangle = \frac{1}{\sqrt{2}} (|p_x\rangle - i|p_y\rangle) \downarrow \\ |7\rangle &= \left| \frac{1}{2}, \frac{1}{2} \right\rangle = -\frac{1}{\sqrt{3}} [(|p_x\rangle + i|p_y\rangle) \downarrow + |p_z\rangle \uparrow] \\ |8\rangle &= \left| \frac{1}{2}, -\frac{1}{2} \right\rangle = -\frac{1}{\sqrt{3}} [(|p_x\rangle - i|p_y\rangle) \uparrow - |p_z\rangle \downarrow] \end{aligned} \quad (\text{A.2})$$

and $\Phi_i(\vec{r})$ is the envelope function of the i -th basis. The wavefunction satisfies the time-independent Schrödinger equation

$$H(\vec{r})\Psi(\vec{r}) = E\Psi(\vec{r}) \quad (\text{A.3})$$

with the Hamiltonian

$$H(\vec{r}) = H_0(\vec{r}) + H_s(\vec{r}) \quad (\text{A.4})$$

where H_0 and H_s are the 8×8 matrices corresponding to the second order eight-band Kane Hamiltonian with modified Luttinger-like parameters and the strain Hamiltonian, respectively. H_0 has the form

$$(\text{A.5})$$

$$H_0 = \begin{bmatrix} E_g + \frac{\hbar^2 k^2}{2m_0} & 0 & pk_+ & -\sqrt{\frac{2}{3}}pk_z & -\sqrt{\frac{1}{3}}pk_- & 0 & \sqrt{\frac{1}{3}}pk_z & -\sqrt{\frac{2}{3}}pk_- \\ 0 & E_g + \frac{\hbar^2 k^2}{2m_0} & 0 & -\sqrt{\frac{1}{3}}pk_+ & -\sqrt{\frac{2}{3}}pk_z & pk_- & \sqrt{\frac{2}{3}}pk_+ & \sqrt{\frac{1}{3}}pk_z \\ pk_- & 0 & F & H^* & -I & 0 & -\sqrt{\frac{1}{2}}H^* & -\sqrt{2}I \\ -\sqrt{\frac{2}{3}}pk_z & \sqrt{\frac{1}{3}}pk_- & H & G & 0 & I & \sqrt{\frac{1}{2}}(F-G) & -\sqrt{\frac{3}{2}}H^* \\ -\sqrt{\frac{1}{3}}pk_+ & -\sqrt{\frac{2}{3}}pk_z & -I^* & 0 & G & H^* & \sqrt{\frac{3}{2}}H & \sqrt{\frac{1}{2}}(F-G) \\ 0 & pk_+ & 0 & I^* & H & F & \sqrt{2}I^* & -\sqrt{\frac{1}{2}}H \\ \sqrt{\frac{1}{3}}pk_z & \sqrt{\frac{2}{3}}pk_- & -\sqrt{\frac{1}{2}}H & \sqrt{\frac{1}{2}}(F-G) & \sqrt{\frac{3}{2}}H^* & \sqrt{2}I & \frac{F+G}{2} - \Delta & 0 \\ -\sqrt{\frac{2}{3}}pk_+ & \sqrt{\frac{1}{3}}pk_z & -\sqrt{2}I & -\sqrt{\frac{3}{2}}H & \sqrt{\frac{1}{2}}(F-G) & -\sqrt{\frac{1}{2}}H^* & 0 & \frac{F+G}{2} - \Delta \end{bmatrix}$$

where

$$\begin{aligned}
k_{\pm} &= \sqrt{\frac{1}{2}}(k_x \pm ik_y) \\
F &= \gamma_1 k^2 + \frac{\gamma_2}{2}(k^2 - 3k_z^2) \\
G &= \gamma_1 k^2 - \frac{\gamma_2}{2}(k^2 - 3k_z^2) \\
H &= -\gamma_3 k_z (k_x + ik_y) \\
I &= \frac{\sqrt{3}}{2} \gamma_2 (k_x^2 - k_y^2) - i\gamma_3 k_x k_y
\end{aligned} \tag{A.6}$$

with the modified Luttinger-like parameters are given by

$$\begin{aligned}
\gamma_1 &= \gamma_1^L + \frac{E_p}{3E_g} \\
\gamma_2 &= 2 \left(\gamma_2^L + \frac{E_p}{6E_g} \right) \\
\gamma_3 &= 2\sqrt{3} \left(\gamma_3^L + \frac{E_p}{6E_g} \right)
\end{aligned} \tag{A.7}$$

where γ_1 , γ_2 , and γ_3 are the Kohn-Luttinger valence band parameters, and E_g is the bandgap. E_p can be obtained from the matrix element for the momentum operator based on the relation

$$E_p = \frac{2}{m_0} |\langle p_x | p_x | s \rangle| \tag{A.8}$$

where m_0 is the free-electron effective mass.

H_s can be written as

(A.9)

$$H_s = \begin{bmatrix} E_s & 0 & 0 & 0 & 0 & 0 & 0 & 0 & 0 \\ 0 & E_s & 0 & 0 & 0 & 0 & 0 & 0 & 0 \\ 0 & 0 & F_s & H_s^* & -I & 0 & -\sqrt{\frac{1}{2}}H_s^* & -\sqrt{2}I_s \\ 0 & 0 & H_s & G_s & 0 & I & \sqrt{\frac{1}{2}}(F_s - G_s) & -\sqrt{\frac{3}{2}}H_s^* \\ 0 & 0 & -I_s^* & 0 & G_s & H^* & \sqrt{\frac{3}{2}}H_s & \sqrt{\frac{1}{2}}(F_s - G_s) \\ 0 & 0 & 0 & I_s^* & H & F_s & \sqrt{2}I_s^* & -\sqrt{\frac{1}{2}}H_s \\ 0 & 0 & -\sqrt{\frac{1}{2}}H_s & \sqrt{\frac{1}{2}}(F_s - G_s) & \sqrt{\frac{3}{2}}H_s^* & \sqrt{2}I_s & \frac{F_s + G_s}{2} & 0 \\ 0 & 0 & -\sqrt{2}I_s & -\sqrt{\frac{3}{2}}H_s & \sqrt{\frac{1}{2}}(F_s - G_s) & -\sqrt{\frac{1}{2}}H_s^* & 0 & \frac{F_s + G_s}{2} \end{bmatrix}$$

with

$$\begin{aligned} E_s &= a_c(\varepsilon_{xx} + \varepsilon_{yy} + \varepsilon_{zz}) \\ F_s &= a_v(\varepsilon_{xx} + \varepsilon_{yy} + \varepsilon_{zz}) + \frac{b}{2}(\varepsilon_{xx} + \varepsilon_{yy} - 2\varepsilon_{zz}) \\ G_s &= a_v(\varepsilon_{xx} + \varepsilon_{yy} + \varepsilon_{zz}) - \frac{b}{2}(\varepsilon_{xx} + \varepsilon_{yy} - 2\varepsilon_{zz}) \\ H_s &= -d(\varepsilon_{zx} + i\varepsilon_{yz}) \\ I_s &= \frac{\sqrt{3}}{2}b(\varepsilon_{xx} - \varepsilon_{yy}) - id\varepsilon_{xy} \end{aligned} \tag{A.10}$$

where ε_{ij} is the strain tensor, and a_c , a_v , b , and d are the deformation potentials for the conduction band and the valence band.

APPENDIX B

GaAs solar cell fabrication procedures

1. Top grid metal deposition
 - 1.1. Immerse the sample in heated Acetone for 5 min
 - 1.2. Immerse the sample in isopropyl alcohol (IPA) for 5 min
 - 1.3. Dry the sample under a stream of nitrogen
 - 1.4. Lithography
 - 1.4.1. Bake the sample at 130 °C for 2 min to remove the solvent residue
 - 1.4.2. Spin coat the photoresist (PR) (SPR 220-3.0 positive photoresist) at 4000 rpm for 30 sec
 - 1.4.3. Bake the sample at 115 °C for 90 sec (soft bake)
 - 1.4.4. Expose the sample under UV light intensity of 20 mW/cm² in hard contact mode for 5 sec
 - 1.4.5. Bake the sample 115 °C for 90 sec (hard bake)
 - 1.4.6. Immerse and stir the sample in MF-319 developer for 1 min – pattern will appear
 - 1.5. Etch away PR residues on the exposed GaAs surface under oxygen plasma
 - 1.6. Immerse the sample in HCl solution (HCl:H₂O = 1:1) for 1 min to remove native oxide on the exposed GaAs surface

- 1.7. Deposit metal layers using E-beam evaporator
- 1.8. Lift-off
 - 1.8.1. Immerse the sample in Acetone until the grid metal pattern appears completely
 - 1.8.2. Rinse the sample in IPA
 - 1.8.3. Dry the sample under a stream of nitrogen
2. Mesa isolation
 - 2.1. Lithography – back to 1.4
 - 2.2. Phosphoric acid etch ($\text{H}_3\text{PO}_4:\text{H}_2\text{O}_2:\text{H}_2\text{O} = 3:1:25$)
 - 2.2.1. Fill the beaker with DI water
 - 2.2.2. Pour hydrogen peroxide (H_2O_2) in to the beaker
 - 2.2.3. Add phosphoric acid (H_3PO_4) into the beaker
 - 2.2.4. Immerse the sample in the solution (etch rate is approximately 0.3 $\mu\text{m}/\text{min}$)
 - 2.2.5. Rinse sample in DI water
 - 2.2.6. Dry the sample under a stream of nitrogen
3. Bottom ohmic contact deposition
 - 3.1. Deposit metal layers using E-beam evaporator
 - 3.2. Remove the PR layer on top using Acetone
 - 3.3. Rinse the sample in IPA
 - 3.4. Dry the sample under a stream of nitrogen
4. Top contacting GaAs layer removal

- 4.1. Etch away the top GaAs layer by reactive ion etching (RIE) with BCl_3 and Ar-based plasma
- 4.2. Citric acid etch (Citric Acid: H_2O_2 : H_2O = 3:1:150) – GaAs residue removal
 - 4.2.1. Fill the beaker with DI water
 - 4.2.2. Pour hydrogen peroxide (H_2O_2) in to the beaker
 - 4.2.3. Add citric acid into the beaker
 - 4.2.4. Immerse the sample in the solution
 - 4.2.5. Rinse sample in DI water
 - 4.2.6. Dry the sample under a stream of nitrogen
5. Annealing
 - 5.1. Anneal the sample at 400 °C for 60 second by rapid thermal processing (RTP)
6. Anti-reflection coating
 - 6.1. Deposit ZnS/ MgF_2 bilayer using E-beam evaporator

BIBLIOGRAPHY

- [1] M. A. Green, "Third generation photovoltaics: Ultra-high conversion efficiency at low cost," *Prog. Photovolt: Res. Appl.*, vol. 9, pp. 123-135, 2001.
- [2] A. Nozik, "Next Generation Photovoltaics Based on Multiple Exciton Generation in Quantum Dot Solar Cells," in *Next Generation of Photovoltaics*, A. B. Cristóbal López, A. Martí Vega and A. Luque López, Eds. Berlin: Springer Berlin Heidelberg, 2012, pp. 191-207.
- [3] G. Conibeer, "Third-generation photovoltaics," *Materials Today*, vol. 10, pp. 42-50, 2007.
- [4] W. Shockley and H. J. Queisser, "Detailed Balance Limit of Efficiency of p-n Junction Solar Cells," *J. Appl. Phys.*, vol. 32, pp. 510-519, 1961.
- [5] L. C. Hirst and N. J. Ekins-Daukes, "Fundamental losses in solar cells," *Prog. Photovolt: Res. Appl.*, vol. 19, pp. 286-293, 2011.
- [6] M. A. Green, K. Emery, Y. Hishikawa, W. Warta and E. D. Dunlop, "Solar cell efficiency tables (version 40)," *Prog. Photovolt: Res. Appl.*, vol. 20, pp. 606-614, 2012.
- [7] M. A. Green, G. Conibeer, D. König, S. Shrestha, S. Huang, P. Aliberti, L. Treiber, R. Patterson, B. P. Veetil, A. Hsieh, Y. Feng, A. Luque, A. Marti, P. G. Linares, E. Cánovas, E. Antolín, D. F. Marrón, C. Tablero, E. Hernández, J.-F. Guillemoles, L. Huang, A. Le Bris, T. Schmidt, R. Clady and M. Tayebjee, "Hot carrier solar cells: Challenges and recent progress," in *35th IEEE Photovoltaic Specialists Conference*, Honolulu, HI, 2010, pp. 57-60.
- [8] O. E. Semonin, J. M. Luther, S. Choi, H.-Y. Chen, J. Gao, A. J. Nozik and M. C. Beard, "Peak External Photocurrent Quantum Efficiency Exceeding 100% via MEG in a Quantum Dot Solar Cell," *Science*, vol. 334, pp. 1530-1533, 2011.
- [9] W. G. J. H. M. van Sark, A. Meijerink and R. E. I. Schropp, "Solar Spectrum Conversion for Photovoltaics Using Nanoparticles," in *Third Generation Photovoltaics*, V. Fthenakis, Ed. Rijeka, Croatia: InTech, 2012, pp. 1-29.
- [10] A. S. Brown and M. A. Green, "Detailed balance limit for the series constrained two terminal tandem solar cell," *Physica E: Low-dimensional Systems and Nanostructures*, vol. 14, pp. 96-100, 2002.
- [11] R. R. King, D. Bhusari, D. Larrabee, X. Q. Liu, E. Rehder, K. Edmondson, H. Cotal, R. K. Jones, J. H. Ermer, C. M. Fetzer, D. C. Law and N. H. Karam, "Solar cell generations over 40% efficiency," *Prog. Photovolt: Res. Appl.*, vol. 20, pp. 801-815, 2012.
- [12] E. F. Schubert, *Physical Foundations of Solid-State Devices*. Troy, NY: Rensselaer Polytechnic Institute, 2009.

- [13] R. R. King, A. Boca, W. Hong, X.-Q. Liu, D. Bhusari, D. Larrabee, K. M. Edmondson, D. C. Law, C. M. Fetzer, S. Mesropian and N. H. Karam, "Band-Gap-Engineered Architectures For High-Efficiency Multijunction Concentrator Solar Cells," presented at the 24th European Photovoltaic Solar Energy Conference and Exhibition, Hamburg, Germany, 2009.
- [14] T. Takamoto, T. Agui, A. Yoshida, K. Nakaido, H. Juso, K. Sasaki, K. Nakamora, H. Yamaguchi, T. Kodama, H. Washio, M. Imaizumi and M. Takahashi, "World's highest efficiency triple-junction solar cells fabricated by inverted layers transfer process," in *35th IEEE Photovoltaic Specialists Conference*, Honolulu, HI, 2010, pp. 412-417.
- [15] D. J. Friedman, J. F. Geisz, S. R. Kurtz and J. M. Olson, "1-eV GaInNAs Solar Cells for Ultrahigh- Efficiency Multijunction Devices," presented at the 2nd World Conference and Exhibition on Photovoltaic Solar Energy Conversion, Vienna, Austria, 1998.
- [16] A. Luque and A. Martí, "Increasing the Efficiency of Ideal Solar Cells by Photon Induced Transitions at Intermediate Levels," *Phys. Rev. Lett.*, vol. 78, pp. 5014-5017, 1997.
- [17] A. Luque and A. Marti, "Photovoltaics: Towards the intermediate band," *Nat Photon*, vol. 5, pp. 137-138, 2011.
- [18] G. F. Brown and J. Wu, "Third generation photovoltaics," *Laser & Photon. Rev.*, vol. 3, pp. 394-405, 2009.
- [19] K. M. Yu, W. Walukiewicz, J. Wu, W. Shan, J. W. Beeman, M. A. Scarpulla, O. D. Dubon and P. Becla, "Diluted II-VI Oxide Semiconductors with Multiple Band Gaps," *Phys. Rev. Lett.*, vol. 91, p. 246403, 2003.
- [20] N. López, L. A. Reichertz, K. M. Yu, K. Campman and W. Walukiewicz, "Engineering the Electronic Band Structure for Multiband Solar Cells," *Phys. Rev. Lett.*, vol. 106, p. 028701, 2011.
- [21] W. Wang, A. S. Lin and J. D. Phillips, "Intermediate-band photovoltaic solar cell based on ZnTe:O," *Appl. Phys. Lett.*, vol. 95, pp. 11103-11105, 2009.
- [22] C. G. Bailey, D. V. Forbes, R. P. Raffaele and S. M. Hubbard, "Near 1 V open circuit voltage InAs/GaAs quantum dot solar cells," *Appl. Phys. Lett.*, vol. 98, pp. 163105-163103, 2011.
- [23] P. J. Carrington, A. S. Mahajumi, M. C. Wagener, J. R. Botha, Q. Zhuang and A. Krier, "Type II GaSb/GaAs quantum dot/ring stacks with extended photoresponse for efficient solar cells," *Physica B: Condensed Matter*, vol. 407, pp. 1493-1496, 2012.
- [24] W. G. Bi and C. W. Tu, "Bowling parameter of the band-gap energy of GaN_xAs_{1-x}," *Applied Physics Letters*, vol. 70, pp. 1608-1610, 1997.

- [25] S. Fahy, A. Lindsay, H. Ouerdane and E. P. O'Reilly, "Alloy scattering of n -type carriers in $\text{GaN}_x\text{As}_{1-x}$," *Physical Review B*, vol. 74, p. 035203, 2006.
- [26] T. Tiedje, E. C. Young and A. Mascarenhas, "Growth and properties of the dilute bismide semiconductor $\text{GaAs}_{1-x}\text{Bi}_x$ a complementary alloy to the dilute nitrides," *International Journal of Nanotechnology*, vol. 5, pp. 963-983, 2008.
- [27] A. Sibille, "Miniband Transport," in *Semiconductor Superlattices: Growth and Electronic Properties*, H. T. Grahn, Ed. River Edge: World Scientific Publishing Co. Pte. Ltd., 1995, .
- [28] K. Uesugi, N. Morooka and I. Suemune, "Reexamination of N composition dependence of coherently grown GaNAs band gap energy with high-resolution x-ray diffraction mapping measurements," *Applied Physics Letters*, vol. 74, pp. 1254-1256, 1999.
- [29] K. Alberi, J. Wu, W. Walukiewicz, K. M. Yu, O. D. Dubon, S. P. Watkins, C. X. Wang, X. Liu, Y. J. Cho and J. Furdyna, "Valence-band anticrossing in mismatched III-V semiconductor alloys," *Physical Review B*, vol. 75, p. 045203, 2007.
- [30] Y. Takehara, M. Yoshimoto, W. Huang, J. Saraie, K. Oe, A. Chayahara and Y. Horino, "Lattice Distortion of GaAsBi Alloy Grown on GaAs by Molecular Beam Epitaxy," *Japanese Journal of Applied Physics*, vol. 45, p. 67, .
- [31] C. H. Fischer, "Molecular beam epitaxy and characterization of GaAsN and its application to quantum dot cascade light sources," Ph.D. thesis, University of Michigan, 2004.
- [32] I. Vurgaftman, J. R. Meyer and L. R. Ram-Mohan, "Band parameters for III-V compound semiconductors and their alloys," *Journal of Applied Physics*, vol. 89, pp. 5815-5875, 2001.
- [33] M. Ferhat and A. Zaoui, "Structural and electronic properties of III-V bismuth compounds," *Physical Review B*, vol. 73, p. 115107, 2006.
- [34] S. Ikuo and et al., "Growth and structural characterization of III–N–V semiconductor alloys," *Semiconductor Science and Technology*, vol. 17, p. 755, 2002.
- [35] I. J. W. Ager and W. Walukiewicz, "Current status of research and development of III–N–V semiconductor alloys," *Semiconductor Science and Technology*, vol. 17, p. 741, 2002.
- [36] X. Lu, D. A. Beaton, R. B. Lewis, T. Tiedje and M. B. Whitwick, "Effect of molecular beam epitaxy growth conditions on the Bi content of $\text{GaAs}_{1-x}\text{Bi}_{1-x}$," *Applied Physics Letters*, vol. 92, pp. 192110-192113, 2008.

- [37] W. Shan, W. Walukiewicz, K. M. Yu, J. W. Ager III, E. E. Haller, J. F. Geisz, D. J. Friedman, J. M. Olson, S. R. Kurtz, H. P. Xin and C. W. Tu, "Band Anticrossing in III–N–V Alloys," *physica status solidi (b)*, vol. 223, pp. 75-85, 2001.
- [38] A. Lindsay and E. P. O'Reilly, "Unification of the Band Anticrossing and Cluster-State Models of Dilute Nitride Semiconductor Alloys," *Physical Review Letters*, vol. 93, p. 196402, 2004.
- [39] G. Pettinari, F. Masia, A. Polimeni, M. Felici, A. Frova, M. Capizzi, A. Lindsay, E. P. O'Reilly, P. J. Klar, W. Stolz, G. Bais, M. Piccin, S. Rubini, F. Martelli and A. Franciosi, "Influence of nitrogen-cluster states on the gyromagnetic factor of electrons in GaAs_{1-x}N_x," *Physical Review B*, vol. 74, p. 245202, 2006.
- [40] T. Dannecker, Y. Jin, H. Cheng, C. F. Gorman, J. Buckeridge, C. Uher, S. Fahy, C. Kurdak and R. S. Goldman, "Nitrogen composition dependence of electron effective mass in GaAs_{1-x}N_x," *Physical Review B*, vol. 82, p. 125203, 2010.
- [41] J. W. Matthews and A. E. Blakeslee, "Defects in epitaxial multilayers: I. Misfit dislocations," *Journal of Crystal Growth*, vol. 27, pp. 118-125, 1974.
- [42] N. J. Ekins-Daukes, K. Kawaguchi and J. Zhang, "Strain-Balanced Criteria for Multiple Quantum Well Structures and Its Signature in X-ray Rocking Curves," *Crystal Growth & Design*, vol. 2, pp. 287-292, 2002.
- [43] D. L. Smith and C. Mailhot, "Theory of semiconductor superlattice electronic structure," *Reviews of Modern Physics*, vol. 62, p. 173, 1990.
- [44] M. E. Flatt, P. M. Young, L.-H. Peng and H. Ehrenreich, "Generalized superlattice K.p theory and intersubband optical transitions," *Physical Review B*, vol. 53, p. 1963, 1996.
- [45] R. J. Potter, D. Alexandropoulos, A. Erol, S. Mazzucato, N. Balkan, M. J. Adams, X. Marie, H. Carrère, E. Bedel, G. Lacoste, A. Arnoult and C. Fontaine, "Comparison of theoretical models for interband transitions in dilute nitrides and experimental measurement," *Physica E: Low-dimensional Systems and Nanostructures*, vol. 17, pp. 240-241, 2003.
- [46] A. A. Khandekar, B. E. Hawkins, T. F. Kuech, J. Y. Yeh, L. J. Mawst, J. R. Meyer, I. Vurgaftman and N. Tansu, "Characteristics of GaAsN/GaAsSb type-II quantum wells grown by metalorganic vapor phase epitaxy on GaAs substrates," *Journal of Applied Physics*, vol. 98, pp. 123525-123525, 2005.
- [47] S. A. Choulis, T. J. C. Hosea, S. Tomić, M. Kamal-Saadi, B. A. Weinstein, E. P. O'Reilly, A. R. Adams and P. J. Klar, "Pressure and k · p studies of band parameters in dilute-N GaInNAs/GaAs multiple quantum wells," *physica status solidi (b)*, vol. 235, pp. 384-389, 2003.

- [48] L. R. Ram-Mohan, K. H. Yoo and R. L. Aggarwal, "Transfer-matrix algorithm for the calculation of the band structure of semiconductor superlattices," *Physical Review B*, vol. 38, p. 6151, 1988.
- [49] I.-H. Tan, G. L. Snider, L. D. Chang and E. L. Hu, "A self-consistent solution of Schrodinger--Poisson equations using a nonuniform mesh," *Journal of Applied Physics*, vol. 68, pp. 4071-4076, 1990.
- [50] E. Anemogiannis, E. N. Glytsis and T. K. Gaylord, "Bound and quasibound state calculations for biased/unbiased semiconductor quantum heterostructures," *Quantum Electronics, IEEE Journal of*, vol. 29, pp. 2731-2740, 1993.
- [51] R. N. Kini, L. Bhusal, A. J. Ptak, R. France and A. Mascarenhas, "Electron Hall mobility in GaAsBi," *Journal of Applied Physics*, vol. 106, pp. 043705-043703, 2009.
- [52] H. Suzuki, T. Hashiguchi, N. Kojima, Y. Ohshita and M. Yamaguchi, "Hole mobility of GaAs_{1-x}N_x grown by chemical beam epitaxy," in *Photovoltaic Specialists Conference (PVSC), 2009 34th IEEE*, 2009, pp. 000848-000851.
- [53] N. F. Johnson, H. Ehrenreich, P. M. Hui and P. M. Young, "Electronic and optical properties of III-V and II-VI semiconductor superlattices," *Physical Review B*, vol. 41, p. 3655, 1990.
- [54] B. Jogai and D. N. Talwar, "Interband optical absorption in strained InAs/In_xGa_{1-x}Sb type-II superlattices," *Physical Review B*, vol. 54, p. 14524, 1996.
- [55] R. B. Laghumavarapu, A. Moscho, A. Khoshakhlagh, M. El-Emawy, L. F. Lester and D. L. Huffaker, "GaSb/GaAs type II quantum dot solar cells for enhanced infrared spectral response," *Appl. Phys. Lett.*, vol. 90, pp. 173125-173123, 2007.
- [56] T. Chi-Che, L. Shih-Yen, L. Wei-Hsun, M. Shu-Cheng, W. Shung-Yi, C. Shu-Han and C. Jen-Inn, "Room-temperature operation type-II GaSb/GaAs quantum-dot infrared light-emitting diode," in *Indium Phosphide & Related Materials (IPRM), 2010 International Conference on*, 2010, pp. 1-3.
- [57] K. S. Hsu, T. T. Chiu, W.-H. Lin, K. L. Chen, M. H. Shih, S.-Y. Lin and Y.-C. Chang, "Compact microdisk cavity laser with type-II GaSb/GaAs quantum dots," *Appl. Phys. Lett.*, vol. 98, pp. 051105-051103, 2011.
- [58] J. Tatebayashi, A. Khoshakhlagh, S. H. Huang, G. Balakrishnan, L. R. Dawson, D. L. Huffaker, D. A. Bussian, H. Htoon and V. Klimov, "Lasing characteristics of GaSb/GaAs self-assembled quantum dots embedded in an InGaAs quantum well," *Appl. Phys. Lett.*, vol. 90, pp. 261115-261113, 2007.
- [59] A. Marent, M. Geller and D. Bimberg, "A novel nonvolatile memory based on self-organized quantum dots," *Microelectronics Journal*, vol. 40, pp. 492-495, 2009.

- [60] M. Geller, C. Kapteyn, L. Müller-Kirsch, R. Heitz and D. Bimberg, "Hole storage in GaSb/GaAs quantum dots for memory devices," *Phys. Stat. Sol. (b)*, vol. 238, pp. 258-261, 2003.
- [61] C. K. Sun, G. Wang, J. E. Bowers, B. Brar, H. R. Blank, H. Kroemer and M. H. Pilkuhn, "Optical investigations of the dynamic behavior of GaSb/GaAs quantum dots," *Appl. Phys. Lett.*, vol. 68, pp. 1543-1545, 1996.
- [62] K. Gradkowski, N. Pavarelli, T. J. Ochalski, D. P. Williams, J. Tatebayashi, G. Huyet, E. P. O'Reilly and D. L. Huffaker, "Complex emission dynamics of type-II GaSb/GaAs quantum dots," *Appl. Phys. Lett.*, vol. 95, pp. 061102-061103, 2009.
- [63] G. G. Zegrya and A. D. Andreev, "Mechanism of suppression of Auger recombination processes in type-II heterostructures," *Appl. Phys. Lett.*, vol. 67, pp. 2681-2683, 1995.
- [64] L. Muller-Kirsch, R. Heitz, A. Schliwa, O. Stier, D. Bimberg, H. Kirmse and W. Neumann, "Many-particle effects in type II quantum dots," *Appl. Phys. Lett.*, vol. 78, pp. 1418-1420, 2001.
- [65] R. Timm, H. Eisele, A. Lenz, S. K. Becker, J. Grabowski, T. Y. Kim, L. Muller-Kirsch, K. Potschke, U. W. Pohl, D. Bimberg and M. Dahne, "Structure and intermixing of GaSb/GaAs quantum dots," *Appl. Phys. Lett.*, vol. 85, pp. 5890-5892, 2004.
- [66] R. Timm, H. Eisele, A. Lenz, L. Ivanova, G. Balakrishnan, D. L. Huffaker and M. Dähne, "Self-Organized Formation of GaSb/GaAs Quantum Rings," *Phys. Rev. Lett.*, vol. 101, p. 256101, 2008.
- [67] A. J. Martin, J. Hwang, E. A. Marquis, E. Smakman, A. Hunter, T. W. Saucer, G. Rodriguez, V. Sih, P. M. Koenraad, J. D. Phillips and J. M. Millunchick, "The disintegration of GaSb/GaAs nanostructures upon capping," *Appl. Phys. Lett.*, submitted for publication.
- [68] P. N. Keating, "Effect of Invariance Requirements on the Elastic Strain Energy of Crystals with Application to the Diamond Structure," *Phys. Rev.*, vol. 145, pp. 637-645, 1966.
- [69] R. M. Martin, "Elastic Properties of ZnS Structure Semiconductors," *Phys. Rev. B*, vol. 1, pp. 4005-4011, 1970.
- [70] H. Jiang and J. Singh, "Strain distribution and electronic spectra of InAs/GaAs self-assembled dots: An eight-band study," *Phys. Rev. B*, vol. 56, pp. 4696-4701, 1997.
- [71] B. Kochman, "Electronic phenomena in self-organized quantum dots: Theory and applications," Ph.D. thesis, University of Michigan, Ann Arbor, MI, 2002.
- [72] M. Willatzen and L. C. Lew Yan Voon, *The $k p$ Method Electronic Properties of Semiconductors*. Berlin, Heidelberg: Springer-Verlag Berlin Heidelberg, 2009.

- [73] B. Fredrik and T. Jukka, "Theory of the electronic structure and carrier dynamics of strain-induced (Ga, In)As quantum dots," *Rep. Prog. Phys.*, vol. 70, p. 1425, 2007.
- [74] K. Boujdaria, S. Ridene and G. Fishman, "Luttinger-like parameter calculations," *Phys. Rev. B*, vol. 63, p. 235302, 2001.
- [75] I. Vurgaftman, J. R. Meyer and L. R. Ram-Mohan, "Band parameters for III-V compound semiconductors and their alloys," *J. Appl. Phys.*, vol. 89, pp. 5815-5875, 2001.
- [76] C. G. Van de Walle, "Band lineups and deformation potentials in the model-solid theory," *Phys. Rev. B*, vol. 39, pp. 1871-1883, 1989.
- [77] S. M. North, P. R. Briddon, M. A. Cusack and M. Jaros, "Electronic structure of GaSb/GaAs quantum domes," *Phys. Rev. B*, vol. 58, pp. 12601-12604, 1998.
- [78] M. E. Rubin, H. R. Blank, M. A. Chin, H. Kroemer and V. Narayanamurti, "Local conduction band offset of GaSb self-assembled quantum dots on GaAs," *Appl. Phys. Lett.*, vol. 70, pp. 1590-1592, 1997.
- [79] R. J. Warburton, B. T. Miller, C. S. Dürr, C. Bödefeld, K. Karrai, J. P. Kotthaus, G. Medeiros-Ribeiro, P. M. Petroff and S. Huant, "Coulomb interactions in small charge-tunable quantum dots: A simple model," *Phys. Rev. B*, vol. 58, pp. 16221-16231, 1998.
- [80] S. M. Reimann and M. Manninen, "Electronic structure of quantum dots," *Rev. Mod. Phys.*, vol. 74, pp. 1283-1342, 2002.
- [81] K. Gradkowski, T. J. Ochalski, D. P. Williams, S. B. Healy, J. Tatebayashi, G. Balakrishnan, E. P. O'Reilly, G. Huyet and D. L. Huffaker, "Coulomb effects in type-II Ga(As)Sb quantum dots," *Phys. Stat. Sol. (b)*, vol. 246, pp. 752-755, 2009.
- [82] P. Moontragoon, N. Vukmirovic, Z. Ikonc and P. Harrison, "Electronic structure and optical properties of Sn and SnGe quantum dots," *J. Appl. Phys.*, vol. 103, pp. 103712-103718, 2008.
- [83] Y.-Y. Lin and J. Singh, "Theory of polarization dependent intersubband transitions in p-type SiGe/Si self-assembled quantum dots," *J. Appl. Phys.*, vol. 96, pp. 1059-1063, 2004.
- [84] M. Geller, C. Kapteyn, L. Muller-Kirsch, R. Heitz and D. Bimberg, "450 meV hole localization in GaSb/GaAs quantum dots," *Appl. Phys. Lett.*, vol. 82, pp. 2706-2708, 2003.
- [85] A. Luque and A. Marti, "Increasing the Efficiency of Ideal Solar Cells by Photon Induced Transitions at Intermediate Levels," *Phys. Rev. Lett.*, vol. 78, p. 5014, 1997.
- [86] A. Marti, E. Antolin, C. R. Stanley, C. D. Farmer, N. Lopez, P. Diaz, E. Canovas, P. G. Linares and A. Luque, "Production of Photocurrent due to Intermediate-to-

Conduction-Band Transitions: A Demonstration of a Key Operating Principle of the Intermediate-Band Solar Cell," *Phys. Rev. Lett.*, vol. 97, p. 247701, 2006.

[87] V. Popescu, G. Bester, M. C. Hanna, A. G. Norman and A. Zunger, "Theoretical and experimental examination of the intermediate-band concept for strain-balanced (In,Ga)As/Ga(As,P) quantum dot solar cells," *Phys. Rev. B*, vol. 78, p. 205321, 2008.

[88] S. M. Hubbard, C. D. Cress, C. G. Bailey, R. P. Raffaele, S. G. Bailey and D. M. Wilt, "Effect of strain compensation on quantum dot enhanced GaAs solar cells," *Appl. Phys. Lett.*, vol. 92, p. 123512, 2008.

[89] G. Wei, K.-T. Shiu, N. C. Giebink and S. R. Forrest, "Thermodynamic limits of quantum photovoltaic cell efficiency," *Appl. Phys. Lett.*, vol. 91, p. 223507, 2007.

[90] Y. D. Jang, T. J. Badcock, D. J. Mowbray, M. S. Skolnick, J. Park, D. Lee, H. Y. Liu, M. J. Steer and M. Hopkinson, "Carrier lifetimes in type-II InAs quantum dots capped with a GaAsSb strain reducing layer," *Appl. Phys. Lett.*, vol. 92, p. 251905, 2008.

[91] F. Hatami, N. N. Ledentsov, M. Grundmann, J. Böhrer, F. Heinrichsdorff, M. Beer, D. Bimberg, S. Ruvimov, P. Werner, U. Gösele, J. Heydenreich, U. Richter, S. V. Ivanov, B. Y. Meltser, P. Kop'ev and Z. I. Alferov, "Radiative recombination in type-II GaSb/GaAs quantum dots," *Appl. Phys. Lett.*, vol. 67, p. 656, 1995.

[92] C.-K. Sun, G. Wang, J. E. Bowers, B. Brar, H.-R. Blank, H. Kroemer and M. H. Pilkuhn, "Optical investigations of the dynamic behavior of GaSb/GaAs quantum dots," *Appl. Phys. Lett.*, vol. 68, pp. 1543-1545, 1996.

[93] R. B. Laghumavarapu, A. Moscho, A. Khoshakhlagh, M. El-Emawy, L. F. Lester and D. L. Huffaker, "GaSb/GaAs II quantum dot solar cells for enhanced infrared spectral response," *Appl. Phys. Lett.*, vol. 90, p. 173125, 2007.

[94] P. J. Carrington, A. S. Mahajumi, M. C. Wagener, J. R. Botha, Q. Zhuang and A. Krier, "Type II GaSb/GaAs quantum dot/ring stacks with extended photoresponse for efficient solar cells," *Physica B*, vol., 2011.

[95] A. Marti, E. Antolín, E. Cánovas, N. López, P. G. Linares, A. Luque, C. R. Stanley and C. D. Farmer, "Elements of the design and analysis of quantum-dot intermediate band solar cells," *Thin Solid Films*, vol. 516, pp. 6716-6722, 2008.

[96] E. Antolín, A. Martí, C. D. Farmer, P. G. Linares, E. Hernández, A. M. Sánchez, T. Ben, S. I. Molina, C. R. Stanley and A. Luque, "Reducing carrier escape in the InAs/GaAs quantum dot intermediate band solar cell," *J. Appl. Phys.*, vol. 108, p. 064513, 2010.

[97] R. Magno, B. R. Bennett and E. R. Glaser, "Deep level transient capacitance measurements of GaSb self-assembled quantum dots," *J. Appl. Phys.*, vol. 88, p. 5843, 2000.

- [98] M. Geller, C. Kapteyn, L. Müller-Kirsch, R. Heitz and D. Bimberg, "450 meV hole localization in GaSb/GaAs quantum dots," *Appl. Phys. Lett.*, vol. 82, p. 2706, 2003.
- [99] A. J. Martin, T. W. Saucer, K. Sun, S. J. Kim, G. Ran, G. V. Rodriguez, X. Pan, V. Sih and J. Millunchick, "Analysis of defect-free GaSb/GaAs(001) quantum dots grown on the Sb-terminated (2 x 8) surface," *J. Vac. Sci. Technol. B*, vol. 30, pp. 02B112-115, 2012.
- [100] A. J. Chiquito, Y. A. Pusep, S. Mergulhao, J. C. Galzerani and N. T. Moshegov, "Capacitance-voltage profile in a structure with negative differential capacitance caused by the presence of InAs/GaAs self-assembled quantum dots," *Phys. Rev. B*, vol. 61, p. 5499, 2000.
- [101] J. B. Wang, F. Lu, S. K. Zhang, B. Zhang, D. W. Gong, H. H. Sun and X. Wang, "Analysis of capacitance-voltage characteristics of Si_{1-x}Gex/Si quantum-well structures," *Phys. Rev. B*, vol. 54, p. 7979, 1996.
- [102] D. K. Schroder, *Semiconductor material and device characterization*. Hoboken: John Wiley & Sons, Inc., 2006.
- [103] S. K. Zhang, H. J. Zhu, F. Lu, Z. M. Jiang and X. Wang, "Coulomb Charging Effect in Self-Assembled Ge Quantum Dots Studied by Admittance Spectroscopy," *Phys. Rev. Lett.*, vol. 80, p. 3340, 1998.
- [104] A. I. Yakimov, A. V. Dvurechenskii, A. I. Nikiforov, A. A. Bloshkin, A. V. Nenashev and V. A. Volodin, "Electronic states in Ge/Si quantum dots with type-II band alignment initiated by space-charge spectroscopy," *Phys. Rev. B*, vol. 73, p. 115333, 2006.
- [105] W.-H. Chang, W. Y. Chen, M. C. Cheng, C. Y. Lai, T. M. Hsu, N.-T. Yeh and J.-I. Chyi, "Charging of embedded InAs self-assembled quantum dots by space-charge techniques," *Phys. Rev. B*, vol. 64, p. 125315, 2001.
- [106] C. M. A. Kapteyn, M. Lion, R. Heitz, D. Bimberg, P. N. Brunkov, B. V. Volovik, S. G. Konnikov, A. R. Kovsh and V. M. Ustinov, "Hole and electron emission from InAs quantum dots," *Appl. Phys. Lett.*, vol. 76, p. 1573, 2000.
- [107] T. Müller, F. F. Schrey, G. Strasser and K. Unterrainer, "Ultrafast intraband spectroscopy of electron capture and relaxation in InAs/GaAs quantum dots," *Appl. Phys. Lett.*, vol. 83, p. 3572, 2003.
- [108] O. Engström, M. Kaniewska, Y. Fu, J. Piscator and M. Malmkvist, "Electron capture cross sections of InAs/GaAs quantum dots," *Appl. Phys. Lett.*, vol. 85, p. 2908, 2004.
- [109] V. Aroutiounian, S. Petrosyan and A. Khachatryan, "Studies of the photocurrent in quantum dot solar cells by the application of a new theoretical model," *Sol. Energ. Mat. Sol. Cells*, vol. 89, pp. 165-173, 2005.

- [110] P. Boucaud, V. Le Thanh, S. Sauvage, D. Débarre and D. Bouchier, "Intraband absorption in Ge/Si self-assembled quantum dots," *Appl. Phys. Lett.*, vol. 74, p. 401, 1999.
- [111] J. Nelson, *The physics of solar cells*. London: Imperial College Press, 2003.
- [112] G. Wei and S. R. Forrest, "Intermediate-Band Solar Cells Employing Quantum Dots Embedded in an Energy Fence Barrier," *Nano Lett.*, vol. 7, pp. 218-222, 2007.
- [113] J. Hwang, A. J. Martin, J. M. Millunchick and J. D. Phillips, "Thermal emission in type-II GaSb/GaAs quantum dots and prospects for intermediate band solar energy conversion," *J. Appl. Phys.*, vol. 111, pp. 074514-074515, 2012.
- [114] K. Lee, J. D. Zimmerman, X. Xiao, K. Sun and S. R. Forrest, "Reuse of GaAs substrates for epitaxial lift-off by employing protection layers," *J. Appl. Phys.*, vol. 111, pp. 033527-033526, 2012.